# In-Volume Laser Direct Writing of Silicon-Challenges and Opportunities

Maxime Chambonneau, David Grojo, Onur Tokel, Fatih Ömer Ilday, Stelios Tzortzakis, Stefan Nolte

LASER & PHOTONICS REVIEWS
www.lpr-journal.org

# In-Volume Laser Direct Writing of Silicon—Challenges and Opportunities

*Maxime Chambonneau,* David Grojo, Onur Tokel, Fatih Ömer Ilday, Stelios Tzortzakis, and Stefan Nolte*

**Laser direct writing is a widely employed technique for 3D, contactless, and fast functionalization of dielectrics. Its success mainly originates from the utilization of ultrashort laser pulses, offering an incomparable degree of control on the produced material modifications. However, challenges remain for devising an equivalent technique in crystalline silicon which is the backbone material of the semiconductor industry. The physical mechanisms inhibiting sufficient energy deposition inside silicon with femtosecond laser pulses are reviewed in this article as well as the strategies established so far for bypassing these limitations. These solutions consisting of employing longer pulses (in the picosecond and nanosecond regime), femtosecond-pulse trains, and surface-seeded bulk modifications have allowed addressing numerous applications.**

## 1. Introduction

Silicon is the basis semiconductor material for countless applications including photovoltaics, sensors, and, more generally, microelectronics. In this latter field, the performance of silicon-based devices is historically governed from the 1970s by the empirical Moore's law, predicting that the size of transistors should be comparable to the one of the atoms in the 2020s. The latest improvements made in quantum computing hold promises for reaching this milestone.[1] These advances are related to the extraordinary developments of the "silicon on insulator" (SOI) lithography technique allowing the fabrication of functional micro- and nano-devices for guiding, modulating, emitting, and detecting light in silicon.[2–4] However, the SOI technique involves several constraints such as (i) the 2D character of the layer-by-layer deposition for fabricating 3D architectures, (ii) the necessity to operate in an extremely clean environment, and (iii) the time required for the fabrication.

An attractive alternative for the SOI technique is ultrafast laser direct writing in the bulk of silicon, as it exists in transparent materials since 1996.[5–7] During the 20 years that followed, the femtosecond laser functionalization of dielectrics (e.g., glasses, polymers) has considerably improved so that, nowadays, high-performance optical devices can be inscribed in these wide band-gap materials. The transposition of this technique to narrow band-gap semiconductor materials such as silicon would thus bring a revolution consisting of a 3D, contactless, and

M. Chambonneau, S. Nolte
Institute of Applied Physics, Abbe Center of Photonics
Friedrich Schiller University Jena
Albert-Einstein-Straße 15, Jena 07745, Germany
E-mail: maxime.chambonneau@uni-jena.de

D. Grojo
Aix-Marseille University
CNRS
LP3, Marseille F-13288, France

O. Tokel, F. Ö. Ilday
UNAM – National Nanotechnology Research Center and Institute of Materials Science and Nanotechnology
Bilkent University
Ankara 06800, Turkey

O. Tokel, F. Ö. Ilday
Department of Physics
Bilkent University
Ankara 06800, Turkey

F. Ö. Ilday
Department of Electrical and Electronics Engineering
Bilkent University
Ankara 06800, Turkey

S. Tzortzakis
Science Program
Texas A&M University at Qatar
Doha 23874, Qatar

S. Tzortzakis
Institute of Electronic Structure and Laser (IESL)
Foundation for Research and Technology—Hellas (FORTH)
Heraklion 1527 GR-71110, Greece

S. Tzortzakis
Materials Science and Technology Department
University of Crete
Heraklion 71003, Greece

S. Nolte
Fraunhofer Institute for Applied Optics and Precision Engineering (IOF)
Center of Excellence in Photonics
Albert-Einstein-Straße 7, Jena 07745, Germany

The ORCID identification number(s) for the author(s) of this article can be found under https://doi.org/10.1002/lpor.202100140



**DOI: 10.1002/lpor.202100140**

**Table 1.** Comparison between the main material properties of crystalline silicon (c-Si) and amorphous silica (a-$SiO_2$) at room temperature. The optical properties are given for 1.3-μm for c-Si and 800-nm wavelength for a-$SiO_2$ since most of the studies have been realized at these wavelengths.

| Material property | c-Si | Ref. | a-$SiO_2$ | Ref. |
|---|---|---|---|---|
| Medium type | Semiconductor | | Dielectric | |
| Band gap Δ (eV) | 1.1 | [39–41] | 9.0 | [42, 43] |
| Spectral domain of transparency between mid-ultraviolet and mid-infrared (μm) | 1.1–7 | | 0.2–3.5 | |
| Linear refractive index $n$ | 3.50 | [34, 44] | 1.45 | [34, 45] |
| Fresnel reflection coefficient for air–material interface | 30.9% | | 3.4% | |
| Group velocity dispersion ($fs^2$ $mm^{-1}$) | 1462.7 | [36] | 36.2 | [45] |
| Nonlinear refractive index $n_2$ ($cm^2$ $W^{-1}$) | $\approx 3.1 \times 10^{-14}$ | [46–48] | $3.5 \times 10^{-16}$ | [49] |
| Critical power for self-focusing $P_{cr}$ (kW) | 24 | | 1903 | |
| Critical plasma density $n_c$ ($cm^{-3}$) | $\approx 10^{20}$ | | $\approx 10^{21}$ | |
| Multi-photon ionization order $N$ | 2 | | 6 | |
| Thermal diffusivity $D$ ($m^2$ $s^{-1}$) | $8.8 \times 10^{-5}$ | [50] | $7.9 \times 10^{-7}$ | [51] |
| Phase transition temperature (K) | 1687 (melting point) | [52, 53] | 3000 (boiling point) | [54] |

fast production of photonic-electronic integrated circuits.[8–10]. Nevertheless, within the same timeframe, the attempts to modify the bulk of monolithic silicon with ultrashort laser pulses were fruitless. The only modifications that were written in the subsurface of silicon have been achieved at a limited depth through an interface with another material.[11,12]

Recent theoretical and experimental works have shed light on the fundamental physical processes that govern in-volume laser–silicon interaction and limit the energy deposition inside the material.[13–15] This novel understanding has subsequently offered multiple possibilities for circumventing these limitations,[16–20] and for producing a wide variety of material changes inside silicon.[21–23] This new avenue to 3D laser-writing in the bulk of silicon has consequently led to the inscription of numerous functions including waveguides,[19,20,24–26] data storage,[19] holograms,[19] microfluidic channels,[19] gratings,[27] as well as surface texturing.[28] These first fruits mark the beginning of a new era for the laser functionalization of silicon as a next generation of $\mu$J-class mid-infrared lasers is emerging,[29,30] offering additional possibilities for investigating this topic.[31]

This review is organized as follows. Section 2 gives an overview about the key properties of silicon influencing the laser-matter interaction. The comparison to amorphous silica allows one to understand the radically different response of silicon to laser irradiation. In Section 3, we present experimental (Section 3.1) and theoretical (Section 3.2) works that have established the limitations inherent to the femtosecond regime for laser-silicon interaction. The restrictive established circumventions (Section 3.3) to these, as well as the applications in the non-modification regime (Section 3.4) are also presented in this section. The existing solutions for achieving laser direct inscription in silicon are presented in Section 4. These solutions include the exploitation of nanosecond (Section 4.1) and picosecond (Section 4.2) pulses, pulse trains (Section 4.3), as well as surface-seeded bulk modifications (Section 4.4). These strategies have enabled addressing a broad range of applications including optical functionalization, wafer dicing, additive manufacturing, microfluidics, and data storage which are presented in this section. Ultimately, the whole set of results is recapitulated in Section 5.

## 2. Properties of Silicon

In this section, we introduce a selection of key parameters that are relevant for understanding the silicon response to energy delivery by ultrashort laser pulses. Systematic comparisons are made with fused silica, a material for which functionalization by femtosecond laser direct writing is way more advanced. A first set of basic properties of crystalline silicon (c-Si) at room temperature is displayed in **Table 1**. The data in silicon are displayed at 1.3-μm wavelength, while the ones of amorphous silica (a-$SiO_2$) are displayed at 800-nm wavelength. While one could estimate that this invalidates such comparison, we make this choice given that these are standard wavelengths for which most of the studies have been realized.

The first major difference between c-Si and a-$SiO_2$ is the material family: silicon is a semiconductor while fused silica is an insulator (i.e., a dielectric). This implies that the intrinsic free-carrier density in fused silica is extremely low compared to the one in silicon. The latter also strongly varies with the doping concentration. For instance, high-resistivity silicon may exhibit electron densities on the order of $n_e \leq 10^{13}$ $cm^{-3}$, while highly doped silicon may show electron densities $n_e \geq 10^{19}$ $cm^{-3}$.

The narrow band gap of silicon ($\Delta = 1.1$ eV) compared to the one of fused silica ($\Delta = 9$ eV) also has important consequences on the optical properties of the materials. There is a large difference in the spectral domain for transparency. Since a photon energy of 1.1 eV corresponds to a wavelength of $\approx 1.1$ μm, silicon linearly absorbs wavelengths below this value. In stark contrast, the transparency domain of fused silica starts from the near-ultraviolet ($\approx 200$ nm). The upper bound of this spectral domain (7- and 3.5-μm wavelength for c-Si and a-$SiO_2$, respectively) for each material (assumed to be defect-free) is determined by its band structure.

Another striking feature in Table 1 in terms of optical properties is the much larger refractive index of silicon ($n = 3.5$) compared to the one of fused silica ($n = 1.45$). This has many consequences.

1. The Fresnel reflection coefficient (assuming an air–silicon interface at normal incidence) is about 30%, while it is < 4% for an air–silica interface. In other words, for an identical input pulse energy, the actual energy reaching the focus is much lower in silicon than in fused silica, considering a linear propagation only.
2. In silicon, the refracted angle is $\theta < 16.6°$ for a maximum near-unity numerical aperture. This relatively low angle value can be taken as a benefit for calculations because the paraxial approximation $\sin(\theta) \approx \theta$ holds independently of the input numerical aperture used for focusing.
3. Because of the high refractive index of the semiconductor, any movement of the silicon sample along the optical axis or the focusing lens is amplified by a factor of 3.5. For this reason, in order to improve the accuracy on the positioning, laser direct writing in silicon generally involve high-precision stages and a vibration-free environment.
4. Another drawback associated to the high refractive index of silicon is spherical aberrations[32] which need to be compensated to generate diffraction-limited spots.
5. As it will be discussed in Section 3, the low angle of the cone of light in silicon implies strong plasma effects (shielding, absorption, reflection, defocusing) in the prefocal region. This is even more pronounced when one considers the long wavelengths inevitably employed for internal processing of silicon. In comparison to dielectrics which can be processed with visible or near-infrared laser pulses, using wavelengths ≥ 1.2 μm for processing silicon implies stronger ponderomotive force.

One should also mention at this stage a noticeable difference in the refractive index of the allotropic phases of the two materials. The amorphous phase of $SiO_2$ ($n = 1.45$) shows a lower refractive index than its crystalline phase for both the ordinary and the extraordinary axis ($n = 1.54$[33,34]). Conversely, the amorphous phase of Si exhibits a higher refractive index ($n \approx 4$ depending on the preparation method[35]) than its crystalline phase ($n = 3.5$). As it will be shown in Section 4, this implies that optical functional devices can be inscribed in silicon with a partial amorphization and/or the formation of polycrystalline phases.

Another remarkable difference in the optical properties of silicon compared to fused silica is the important group velocity dispersion value. Silicon is a highly dispersive medium with a group velocity dispersion on the order of 1500 $fs^2$ $mm^{-1}$. To be precise, the value of 1462.7 $fs^2$ $mm^{-1}$ in Table 1 is extracted from ref. [36] and given at 1.357-μm wavelength, not at 1.3-μm wavelength. However, since this wavelength is close to 1.3 μm, and because we do not expect a drastic change in the group velocity dispersion value, we safely assume that the value at 1.3-μm wavelength is on the same order of magnitude. The high group velocity dispersion of silicon implies that, after only one millimeter of propagation in the material, pulses with a duration ≤100 fs will be drastically stretched. For instance, a pulse of 60-fs duration is stretched to 100 fs after one millimeter of propagation in silicon.[34] The much lower group velocity dispersion of fused silica makes that pulse stretching by dispersion can be neglected unless much shorter pulses (near few-optical-cycles) are considered in this material. An important conclusion from these simple considerations is that increasing the intensity at the focus by using pulses below 100-fs duration will not be a viable approach without implementation of precompensation strategies.

Other important features of silicon to consider are the nonlinearities. As shown in Table 1, silicon exhibits a high nonlinear refractive index ($n_2 \approx 3.1 \times 10^{-14}$ $cm^2$ $W^{-1}$)—and, thus, a low critical power for self-focusing—compared to glasses. Rigorously, the nonlinear response of silicon is anisotropic. For instance, as shown in ref. [37], the nonlinear refractive index of the material (as well as the multi-photon absorption coefficient) decreases by ≈ 12% along the [0 1 0] direction compared with the [0 1 $\bar{1}$] direction in the 1.2–2.4-μm wavelength range. Given that we are mostly interested in comparing the order of magnitude of the nonlinear refractive index of crystalline silicon and amorphous silica, this anisotropy is neglected in this review. As can be seen in Table 1, there is a difference of orders of magnitude in the critical power for self-focusing between the two analog cases in silicon ($P_{cr} = 24$ kW) and silica ($P_{cr} = 1.9$ MW). This implies that the propagation is nonlinear even at modest pulse energies. If one considers a 100-fs duration pulse, self-focusing occurs in silicon at pulse energies at the nanojoule level, while a few hundreds of nanojoules are required for self-focusing to play a role in fused silica. As it will be discussed in Section 3, pulse energies of a few nanojoules are insufficient for provoking any permanent modification in silicon, even with the tightest focusing conditions (i.e., NA ≫ 1[18]). Therefore, one cannot neglect the role of the optical Kerr effect in the beam propagation of femtosecond and picosecond pulses inside silicon. Similarly, we note a strong difference in the multi-photon ionization orders. This results in an increased absorption and depletion of pulse energy provoking plasma effects already in the prefocal region which are detrimental for efficient energy delivery to the focus region.

Finally, one should note in Table 1 the differences in the thermal properties of silicon compared to fused silica. Let us consider that the production of permanent modifications is correlated with a phase transition of the material. Despite the fact that the phase transition temperature of c-Si (1687 K) is way below that of a-$SiO_2$ (3000 K), the thermal diffusivity of silicon is two orders of magnitude higher than the one of fused silica. In other words, any laser-produced heat in silicon will rapidly diffuse away from the heat source (i.e., the focus). This represents a technical complication for elaborating heat-accumulation-based laser techniques in silicon. In fused silica, repetition rates on the order of 100 kHz are typically sufficient for provoking cumulative effects.[38] As it will be shown in Sections 4.3 and 4.4, the high thermal diffusivity of silicon implies that repetition rates higher than 10 MHz (i.e., 100 ns between two consecutive pulses) are required for provoking heat accumulation.

A conclusion of this comparison is that the narrow band gap of semiconductors associated to the long wavelengths required to carry out in-volume multi-photon interactions leads to linear and nonlinear effects profoundly modifying the energy flux in comparison to experiments in dielectrics. This can be attractive for novel nonlinear propagation and filament-induced manipulations. However, it also complicates the situation for controlled and highly concentrated energy deposition in the

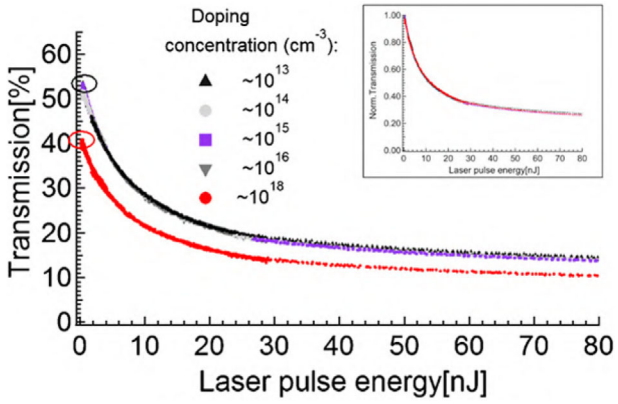


**Figure 1.** Evolution of the transmission of silicon samples with various initial doping concentrations as a function of the input pulse energy. The inset is a normalization of the same data. Laser wavelength: 1.3 μm; Pulse duration: 100 fs. Reproduced with permission.[57] Copyright 2013, Elsevier.

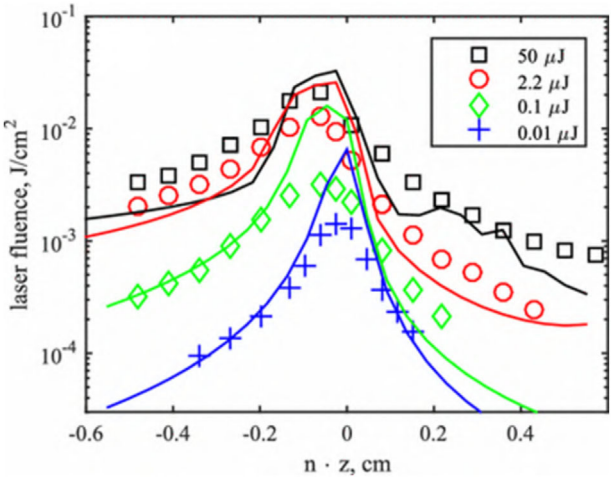


**Figure 2.** Evolution of the maximum laser fluence in silicon as a function of the optical path $n \cdot z$ along the optical axis $z$, where $n$ is the refractive index of silicon, for different input pulse energies. The symbols are the experimental data and the lines are simulations of the nonlinear propagation (see Section 3.2). Laser wavelength: 1.2 μm; pulse duration: 250 fs. Reproduced with permission.[58] Copyright 2016, Springer Nature.

bulk of the material. Even under very tight focusing conditions, nonlinear Kerr-induced phase distortions and strong plasma effects must occur in regimes where semiconductor material modifications can be expected. These are aspects that will be discussed hereafter with the presentation of the limitations on space–time localization of the energy deposition in silicon, and the solutions demonstrated to overcome them.

## 3. Self-Limited Excitation with Ultrashort Pulses

### 3.1. Experimental Evaluation of the Energy Deposition

#### *3.1.1. Time-Integrated Measurements of the Nonlinear Ionization*

In order to improve the comprehension of the physics of laser–silicon interaction, the first important step consists of identifying the involved ionization mechanisms—and thus, the way the energy is deposited inside the material. Three ionization processes are susceptible to occur which are multi-photon, tunnel and impact ionization—this latter provoking avalanche ionization when combined to Joule heating of electrons in the conduction band by inverse bremsstrahlung absorption. To determine which of the two first photo-ionization mechanisms is dominant, one usually refers to the Keldysh adiabaticity parameter $\gamma$.[55] For typical intensities involved in femtosecond laser processing (on the order of $10^{12}$ W cm$^{-2}$) and wavelengths for which silicon is transparent, $\gamma > 1$, and it is thus reasonable to assume that the contribution of multi-photon ionization is more important than that of tunnel ionization as shown in ref. [56]. In order to reveal the relevance of avalanche ionization, Leyder et al. measured the transmission of silicon samples with various initial doping concentrations for an irradiation with 100-fs duration pulses at 1.3-μm wavelength.[57] The results are shown in **Figure 1** as a function of the input pulse energy (measured before the entrance surface of the sample). For doping concentrations $\leq 10^{16}$ cm$^{-3}$, the nonlinear transmission response with respect to the input pulse intensity is very similar. The transmission values for near-zero pulse energies are about 50% corresponding to losses due to Fresnel reflections at both air–silicon interfaces. In contrast, the results for a doping concentration of $10^{18}$ cm$^{-3}$ are shifted to lower transmission values. We simply note an offset due to the contribution of linear absorption by free carriers in high conductivity samples, without any significant change on the nonlinearity of the response (energy dependence). As shown by the inset in Figure 1, the normalized transmission curves are identical for all the tested doping concentrations. Because avalanche ionization strongly depends on the initial electron density, one would expect these behaviors to be radically different once the density is sufficient for triggering avalanche. An important conclusion of this study was that, for 100-fs duration pulses, the contribution of avalanche ionization is very limited, independently of the initial doping concentration. Therefore, this indicates that simplified simulations accounting only for multi-photon ionization can be valid for some interaction cases with ultrashort pulses.

In order to evaluate the location of the deposited energy as well as the maximum fluence reached inside silicon, Kononenko et al. employed nonlinear propagation imaging.[58] The measurements displayed in **Figure 2** rely on an inverted microscope for imaging the exit surface of a silicon sample. The beam is focused inside the sample and moved at different locations. One can distinguish two main results in Figure 2. The first one is that the position of the maximum fluence (i.e., the focus) along the optical axis strongly depends on the input pulse energy. Starting from the lowest pulse energy, the focus is unambiguously shifted upstream the laser for increased pulse energies. This nonlinear focal shift mainly related to the optical Kerr effect is typical from the filament formation,[59] in good agreement with the peak power exceeding the critical power for self-focusing for pulse energies $\geq 10$ nJ and a pulse duration of 250 fs. This behavior was confirmed by nonlinear propagation simulations described in Section 3.2. The second main result, also typical from filament formation,[49] is the evidence of the intensity clamping phenomenon in bulk silicon. In comparison to an expected proportionality between the input pulse energy and the measured

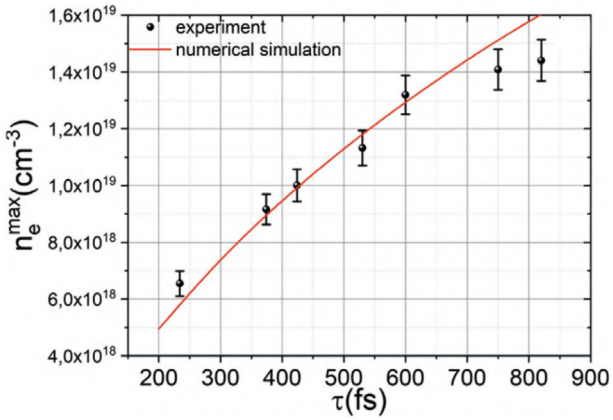


**Figure 3.** Evolution of the maximum electron density in silicon as a function of the pulse duration, for an input pulse energy of 250 nJ and a numerical aperture NA = 0.5. The symbols are the experimental data, and the lines are simulations of the nonlinear propagation (see Section 3.2). Laser wavelength: 1.24 µm. Reproduced with permission.[60] Copyright 2020, IOP Publishing.

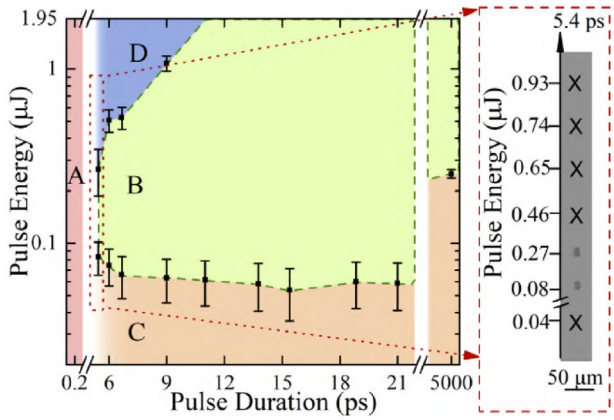


**Figure 4.** Identified conditions allowing laser-induced micro-modification inside silicon with a numerical aperture NA = 0.85. The green region "B" shows the identified set of parameters for which local modifications are observed. The regions "A" and "D" indicate the domains for which the pulse duration are respectively too short or the energy too high to avoid the light delocalization which prevents the initiation of modifications. The region "C" indicates conditions below the energy threshold for modifications. Laser wavelength: 1.55 µm. Reproduced with permission.[62] Copyright 2020, The Optical Society.

delivered fluence for linear propagation, strong deviations were observed in Figure 2. For instance, for 0.01 and 50-µJ input pulse energy (corresponding to a ratio of 5000), the delivered fluence ratio was only 20 in the reported experiments. This evidences strong nonlinear propagation effects in the investigated situation.

By employing a similar approach, Mareev et al. recently investigated the pulse duration dependence of the energy deposition in silicon.[60] The nonlinear propagation imaging relies on a silicon-based camera.[61] While this type of camera is usually less costly than infrared cameras, the dynamic range is reduced for laser pulses of wavelength ≥ 1.1 µm due to the fact that the two-photon response of the device has to be taken into account. In addition, for accessing the maximum electron density produced, the authors carried out nonlinear transmission measurements. The experimental electron density values were deduced from the absorption values thanks to the Drude–Lorentz model, where the distribution of the imaginary part of the experimental and the theoretical wave vectors are compared. The results obtained at 1.24-µm wavelength for different pulse durations are displayed in **Figure 3** for a pulse energy of 250 nJ. The electron density increases with the pulse duration, as confirmed by nonlinear propagation calculations (see Section 3.2). This result is consistent with the fact that increasing the pulse duration for a constant input pulse energy decreases the intensity—and, thus, the detrimental nonlinear propagation effects preventing the localization of the energy deposition inside silicon.

This observation from Mareev et al.[60] was confirmed in another recent experimental study by Das et al. where an even larger pulse duration range (0.2–21 ps) has been investigated.[62] In this work, the authors rely on a high temporal-contrast femtosecond optical parametric amplifier operated at 1.55-µm wavelength. An optional two-grating stretcher arrangement can be inserted in the optical path for adjustment of the pulse duration from 4 to 21 ps. This study was complemented with nanosecond pulses delivered by a compact fiber source. For pulse durations up to ≈ 1 ps, the measured electron densities in ref. [60] were increasing with pulse duration but remain in the range $n_e = 0.65–1.45 \times 10^{19}$ cm$^{-3}$, which is below the critical density ($n_c = 7.3 \times 10^{19}$ cm$^{-3}$ at 1.24-µm wavelength). One should emphasize that the criterion $n_e = n_c$ for material modification is not the most accurate, and criteria based on the total delivered energy inside the material generally give more realistic results.[63] The delivered energy can be derived by evaluating the work done by the electromagnetic field force acting on the electrons.[64] Mareev et al. showed that the delivered energy inside silicon increases with the pulse duration. Nevertheless, for pulse durations < 900 fs, the corresponding delivered energy values are below the latent heat of fusion of silicon (3.4 kJ cm$^{-3}$), suggesting the impossibility to modify the material at these durations. By measuring the delivered energy density inside silicon for a similar numerical aperture (NA = 0.45) and performing damage test experiments, it is shown in ref. [62] that the same conclusion must hold for 21-ps pulses. This indicates the persistence of detrimental nonlinear propagation effects even if these are progressively decreased with pulse stretching. However, one has to keep in mind that not only the absorbed energy density but also the material breakdown threshold also increases with the pulse duration.[65–67] This must lead to an optimum pulse duration for addressing 3D silicon processing applications with a minimum of energy. Interestingly, repeating the damage study with a focusing optics of NA = 0.85, the authors found that a minimum duration of 5.4 ps was required for initiating permanent modifications.[62] As shown in **Figure 4**, they observed the existence of an energy which should not be exceeded for the shortest pulses (typically 5.4–10 ps) in order to avoid delocalization of the energy deposition (see region "D"). In accordance with the decrease of nonlinear effects that prevent energy delivery, the repeatability of the achieved modifications was also improved by increasing the pulse duration. However, no significant change in the energy threshold was reported in the picosecond range (see Figure 4). The modification threshold is lower in the picosecond than in

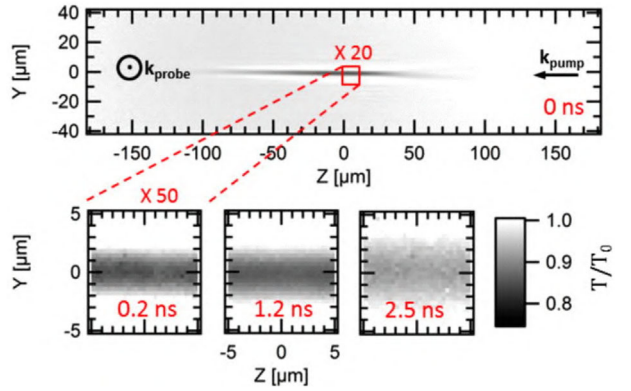


**Figure 5.** Ultrafast infrared microscopy observation of a femtosecond laser-induced microplasma (20-nJ input pulse energy, NA = 0.3). The high-resolution images acquired for different delays reveal directly the expansion of the microplasma by free-carrier diffusion. Laser wavelength: 1.3 µm; Pulse duration: 60 fs. Reproduced with permission.[78] Copyright 2016, American Institute of Physics.

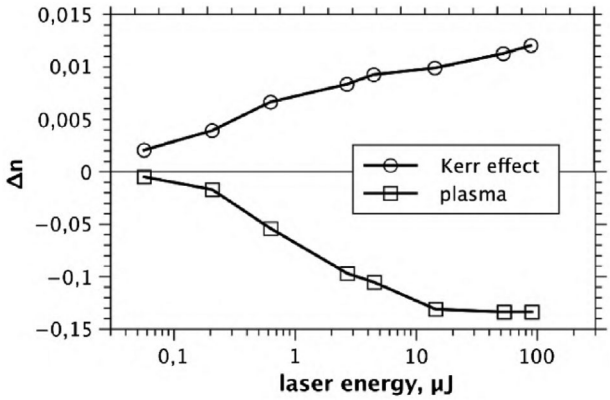


**Figure 6.** Laser-induced transient refractive index change versus energy of laser pulses near the focus inside silicon. The $+\Delta n$ and $-\Delta n$ scales are different. Laser wavelength: 1.2 µm; Pulse duration: 250 fs. Reproduced with permission.[77] Copyright 2012, The Optical Society.

the nanosecond regime. Nevertheless, the difference is not as high as one could expect assuming a square-root dependence for the damage threshold as for thermally-driven surface interaction with long pulses.[65,66] Overall, a minimum bulk modification threshold was observed by tuning the pulse duration. When this latter is excessively short or long, this threshold increases due to nonlinear propagation effects and heat transport, respectively.

### *3.1.2. Time-Resolved Ultrafast Imaging Experiments*

A more direct way to observe femtosecond laser-induced carrier excitation in transparent materials is to rely on ultrafast imaging using pump-probe optical arrangements.[68–70] Given that dielectrics are transparent to visible light which can be sensed with standard silicon-based detectors, various pump-probe methods have been applied during the last decades to experimentally access all dynamical aspects from ionization, trapping of generated free-carriers to material responses.[51,68–76] This metrology is progressively translated in the infrared to allow similar measurements inside silicon and other narrow-gap semiconductors.[13,77,78] While the resolution limit obviously decreases with long wavelengths, by using InGaAs array sensors and microscopy arrangements optimized at telecommunication wavelengths (e.g., 1.3 or 1.55 µm), one can reach enough precision to extract the free-carrier density and the spatial distribution of the laser-induced microplasmas produced by tightly focused femtosecond pulses. **Figure 5** shows an example of amplitude imaging of such microplasmas generated 1 mm below the surface of a silicon sample by two-photon ionization with 60-fs duration pulses at 1.3-µm wavelength.[78] In practice, a beam splitter separates the beam in probe and pump pulses. The probe beam is directed to an optical delay stage and illuminates the silicon sample perpendicular to the excitation by the pump pulse. By moving the delay stage, the optical path of the probe beam can be adjusted, so the time difference between the pump and the probe pulses is changed. The resulting images shown in Figure 5 represent the spatial transmittance of the probe pulse, corrected for background intensity measured without laser excitation. Interestingly, the high-mobility and long-lived characteristics of free-carriers in silicon combined to resolution-limited infrared imaging performances allowed to observe directly the plasma expansion due to the diffusion of carriers (which is not achievable in dielectrics due to the low carrier mobility).[78] Under these experimental conditions, the lifetime of the laser-produced microplasmas inside silicon was measured to be ≈ 2.5 ns.

To extract free-carrier densities from the plasma linear transmission images, one can apply a Drude model accounting for inverse bremsstrahlung absorption of the probe.[79] Both experimental works of Kononenko et al. using high-energy focused pulses (> 90 µJ),[77] and Mouskeftaras et al. for relatively tight focusing conditions (NA = 0.3)[13] conclude on sub-critical plasma densities in all tested femtosecond interactions in silicon. They observed a clamping of the plasma density as evidenced by the pump-energy dependence of the refractive index change and the transmission loss associated with plasma formation. **Figure 6** shows a typical measurement of transient refractive index change, and **Figure 7** shows the measured plasma absorption corresponding to a maximum level of excitation near or below $10^{20}$ cm$^{-3}$. This is significantly below the critical plasma density (≈ $6 \times 10^{20}$ cm$^{-3}$ at 1.3-µm wavelength) and represents a major difference with femtosecond-laser–dielectric interactions for which much higher densities are reported.[80,81]

By using pump-probe interferometry, Kononenko et al. have investigated the dynamics of plasma formation in silicon.[82] The evolution of the brightness of an interference pattern (directly linked to the refractive index change) at the focus of a 250-fs duration pump beam at 1.2-µm wavelength is shown in **Figure 8** for different probe delays. The refractive index change is positive during the pump pulse, and turns negative afterward. This behavior analogous to the one observed using similar pump-probe interferometry techniques in wide band-gap materials[71,83–85] highlights the competition between the optical Kerr effect and the plasma formation together with defocusing. Indeed, the positive refractive index change $\Delta n$ during the pump pulse can be attributed to the optical Kerr effect as $\Delta n = n_2 I$, where $n_2$ and $I$ are the nonlinear refractive index and the pump intensity, respectively. The negative refractive index change corresponds to

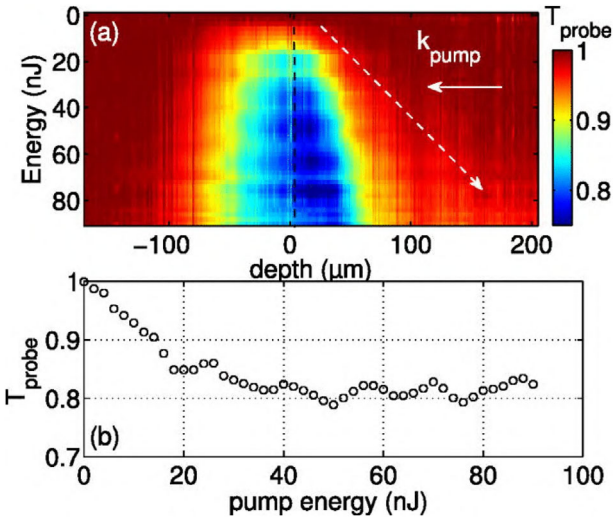


**Figure 7.** a) Probe transmission as a function of the pump pulse energy and the depth inside silicon. Pump-probe delay is fixed at 10 ps. The dashed arrow indicates the shift of the absorption distribution. b) Evolution of the measured transmission of the microplasma as a function of the pump pulse energy [dotted line in a)]. Laser wavelength: 1.3 μm; Pulse duration: 60 fs. Reproduced with permission.[13] Copyright 2014, American Institute of Physics.

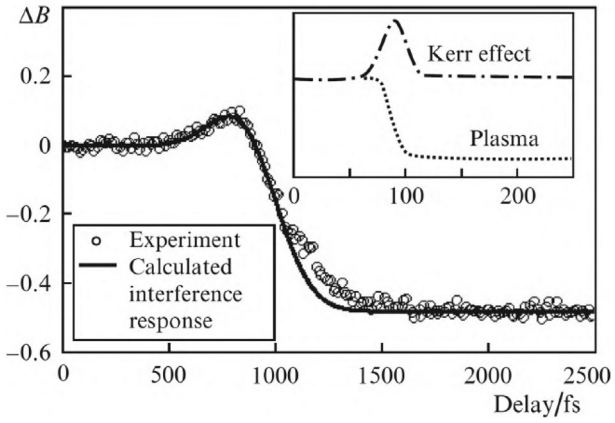


**Figure 8.** Evolution of the relative brightness $\Delta B$ of an interferogram at the focus of the pump beam (with a pulse energy of 4.5-μJ) as a function of the probe delay. The circles stand for the experimental data, and the solid line corresponds to calculations with a model which takes into account Kerr effect and plasma formation. These two effects are shown separately in the inset. Laser wavelength: 1.2 μm; pulse duration: 250 fs. Reproduced with permission.[82] Copyright 2012, IOP Publishing.

the contribution of free carriers according to the Drude model[79] $\Delta n = -2\pi e^2 n_e/(n_0 \omega^2 m^*)$, where $e$ is the elementary charge, $n_0$ is the refractive index of silicon, $\omega$ is the laser angular frequency, $m^*$ is the effective mass of the carriers, and $n_e$ is the electron density which can be evaluated by considering two-photon absorption as the dominant ionization mechanism (see Section 3.1.1). The calculated interference response in Figure 8 relies on the sum of these two contributions, and is in agreement with the experimental data. Despite the simplicity of this model for describing all the involved processes (see Section 3.2), the good agreement between theory and experiments demonstrates that the major mechanisms occurring during laser–silicon interaction are well-described.

A major limitation of the pump-probe technique remains the sensitivity since the dynamic range of infrared cameras limits the minimum measurable absorption at typical levels of few percent (performance similar to standard silicon-based technologies at best). Technically, this means that only densities exceeding $10^{17}$ cm$^{-3}$ can reasonably be detected for micrometer-size plasmas by absorption. Thus, as it will be shown below, the progressive excitation in the prefocal volume as the pulse approaches the focus is hardly revealed by these imaging experiments. Beyond these state-of-the-art pump-probe experiments, new infrared imaging developments will be required to access more details of femtosecond interactions in semiconductors. In particular, we anticipate that the advanced holographic imaging methodologies developed in the visible domain to study nonlinear interactions in dielectrics[73,86,87] can be transposed to the infrared. It should allow retrieval not only of the imaginary part of the refractive index with increased sensitivity but also of the changes in its real part. These improvements are essential to follow both in time and 3D-space the ionization dynamics and other effects such as the strong Kerr-induced nonlinearities inherent to narrow band-gap materials described in the previous section.

### *3.1.3. Interactions with Non-Gaussian Beams*

To achieve higher space–time localization of energy deposition, potential optimizations of the energy deposition have been investigated. In particular, femtosecond Bessel beams have been endeavored because this class of beams is known to strongly resist to detrimental nonlinear distortions. In Bessel beams, the energy is directed everywhere at a given angle with respect to the optical axis (conical energy flux) providing two advantages for energy deposition over long distances. First, it makes the interactions free from spherical aberrations in comparison with focused Gaussian beams that contain a wide range of angles of incidence. Second, an even more important feature is that the intensities remain modest until the central core region on the optical axis is reached. For high Bessel angles, it is only here that significant nonlinear effects (including nonlinear beam distortions and nonlinear absorption) occur.[88] These beams therefore intrinsically allow controlled interactions at higher intensities compared to Gaussian beams which has already been exploited for the fabrication of high aspect-ratio nano-channels in glasses using single femtosecond pulses at 800-nm wavelength.[89,90] He et al. have presented evidence of the fabrication of high-quality through-silicon vias which constitute an essential building block for vertical electrical connections in 3D integrated electronics circuits using femtosecond Bessel-like beams at 1.5-μm wavelength.[91] The corresponding realizations displayed in **Figure 9** were obtained on ultra-thin wafers by employing a drilling technique with sequences of 1200 high-energy (104 μJ) 65-fs duration pulses. The morphology—and, thus, the quality—of the vias strongly depends on the spatial beam shape. As shown in Figure 9a, Gaussian-shaped beams lead to conical through-silicon vias due to the short Rayleigh length inherent to tight focusing conditions (NA = 0.3). To solve this issue, one could think about employing a conventional Bessel beam shape showing an extended depth of focus. While this

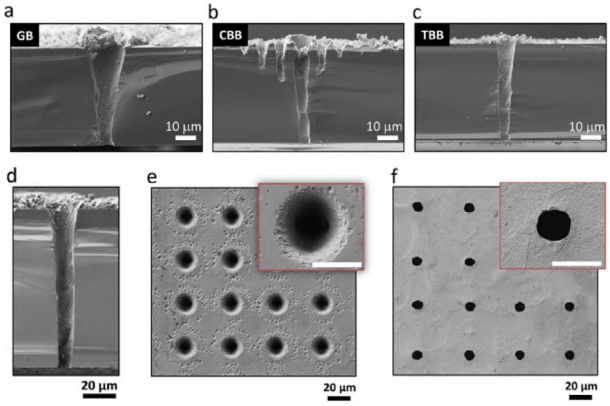


**Figure 9.** a–c) Cross Section images of through-silicon vias fabricated using a) a Gaussian beam (GB), b) a conventional Bessel beam (CBB), and c) a tailored Bessel beam (TBB) in a 50-µm silicon sample. d–f) Images of d) the cross section, e) the entrance surface, and d) the exit surface of vias fabricated in a 100-µm thick silicon sample with a tailored Bessel beam. The scale bars in the insets of e) and f) are 5 µm. Laser wavelength: 1.5 µm; pulse duration: 65 fs. Reproduced with permission.[91] Copyright 2017, Springer Nature.

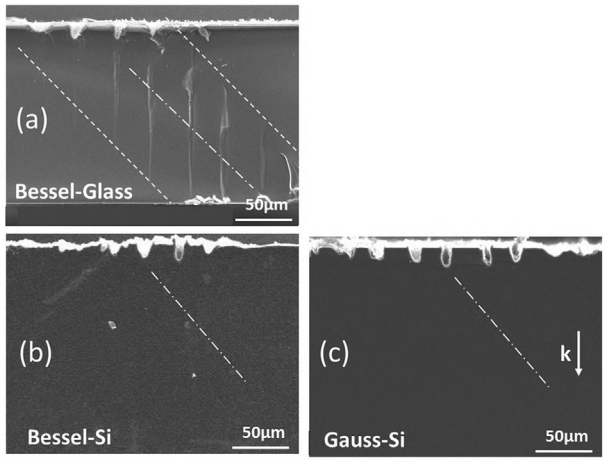


**Figure 10.** Comparison between modifications induced in glass and silicon for a pulse energy of 12 µJ. For all substrates, lines are written at different depths and cross-sections are observed by scanning electron microscopy (SEM). The dashed dotted line shows the evolution of focus position to guide the eye. Laser wavelength: 1.3 µm; pulse duration: 100 fs. Reproduced with permission.[92] Copyright 2015, American Institute of Physics.

solution works well at the center of the Bessel beam (see Figure 9b), the non-negligible energy contained in the side lobes provokes damage on the entrance surface. The authors solved this problem by using a customized binary phase plate for tailoring the shape of the Bessel beam. The resulting through-silicon vias in 50-µm (Figure 9c) as well as 100-µm (Figure 9d,e) thick silicon samples exhibit a high aspect-ratio with no unwanted damage on the surface, and are almost cylindrical.

To investigate the natural bulk silicon response to a Bessel energy flux, other groups have produced high-angle femtosecond Bessel beams (> 20°) at 1.3-µm wavelength with axicon-based methods.[92] In addition, high energy versions of the beams leading to ultrahigh intensities (> $10^{15}$ W cm$^{-2}$) over millimeter-long distances have been endeavored.[90] A direct comparison of the modifications induced in samples of borosilicate glass and silicon with Bessel and focused Gaussian beams is shown in **Figure 10**. Concerning glass, it is found that the Bessel beams produce complete through hole modifications with efficiencies very similar to those commonly reported at 800-nm wavelength.[89,93–95] However the response in silicon is drastically different. We note that the surface damage threshold is largely exceeded. The stronger surface damage sites in comparison to glass are associated to the high two-photon absorption coefficient of silicon. However, for both Bessel and focused Gaussian beams there is no noticeable material modification in the bulk.

An interesting complementary diagnostic in these femtosecond Bessel beam experiments is the measurement of the intensity delivered in the bulk which exhibits a clamping at $\approx 4 \times 10^{11}$ W cm$^{-2}$.[92] The corresponding fluence (0.05 J cm$^{-2}$) is well below the known thresholds for surface modification of silicon ($F_{th}$ > 0.1 J cm$^{-2}$)[96,97] but the intensity exceeds the reported thresholds for measurable two-photon absorption ($\approx 10^{10}$ W cm$^{-2}$.[56]) A simple estimate of the produced free-carrier density can be made with the relation $N_{max} = (\tau\beta I_{max}^2)/(2\hbar\omega)$ where $\tau$ = 110 fs, $\beta$ and $\hbar\omega$ = 0.95 eV are respectively, the pulse duration, the two-photon absorption coefficient, and the photon energy associated to these experiments. This relation neglects collision-assisted ionization and avalanche ionization mechanisms.[57] Using a two-photon absorption coefficient in the range of 0.5–1.5 cm GW$^{-1}$,[46–48,98] one finds a maximum free-carrier density $N_{max} = 2.9–8.1 \times 10^{19}$ cm$^{-3}$ remarkably matching the values found with the measurements based on ultrafast imaging of the plasma created by Gaussian beams (see Section 3.1.2). These considerations show that the benefit of Bessel beams on ultrafast silicon excitation (if any) remains very modest in the situations investigated. One possible reason for this limitation is that spatial improvement requires a large-angle cone of light (i.e., breaking the paraxiality), which is particularly challenging to achieve in high refractive index materials (see Section 2). Even if the Bessel beams that have been produced rely on large angles, they do not exceed the highest angle components in tightly focused Gaussian beam experiments. To improve this aspect, one option would be to consider more exotic beams as ring-Airy beams that exhibit a parabolic energy flux and nonlinear collapsing features that have shown their potential for high intensity delivery in dielectrics.[99,100] However, the potential of this direction has not been carefully evaluated in semiconductors so far. It would also require new experimental developments to address this topic at non-conventional wavelengths.

### 3.2. Theoretical Identification of the Limiting Processes

Early studies on the modeling of ultrashort-laser-silicon interaction were performed using vectorial solver of Maxwell's equations based on a finite-difference time-domain (FDTD) method. In that way, Bogatyrev et al. developed a 3D model relying on a FDTD approach for describing the local energy deposition in semiconductors (silicon and gallium arsenide).[101] The method includes a two-temperature model and takes into account linear absorption, two-photon absorption as well as

avalanche ionization, with no recombination term included. The main difficulty arising from FDTD-based approaches is the excessive computation time, especially in a 3D configuration. In order to elucidate the experimental limitations developed in Section 3.1, Zavedeev et al. developed a scalar model based on the nonlinear Schrödinger equation (NLSE).[14,102] This latter consists of calculations of the space-time-dependent magnitude of the electric field $E$ of a femtosecond laser pulse under the slowly varying envelope approximation. The model takes into account various physical mechanisms and can be written in cylindrical coordinates $(r, z)$ as[14]

$$\frac{\partial E}{\partial z} = \frac{i}{2k_0}\left(\frac{1}{r}\frac{\partial}{\partial r} + \frac{\partial^2}{\partial r^2}\right)E + \frac{ik_0 n_2}{n_0}|E|^2 E - \frac{\beta_2}{2}|E|^2 E - \frac{\sigma}{2}\left(1 + i\omega_0\tau_c\right)\rho_e E \quad (1)$$

On the right-hand side in Equation (1), the first, second, third and fourth terms correspond to the diffraction, the optical Kerr effect, the two-photon absorption, and the plasma absorption and defocusing according to the Drude model,[79] respectively. In Equation (1), $k_0$ is the wavenumber of the laser pulse with a center angular frequency $\omega_0 = 2\pi c/\lambda$, $c$ is the speed of light in vacuum, $\lambda$ is the wavelength of the laser pulse, $n_0$ is the linear refractive index of silicon, $n_2$ is the nonlinear refractive index, $\beta_2$ is the two-photon absorption coefficient, $\sigma = e^2 k_0 \omega_0 \tau_c / [n_0^2 \omega_0^2 \varepsilon_0 m^* (1 + \omega_0^2 \tau_c^2)]$ is the inverse bremsstrahlung absorption cross section, $e$ is the elementary charge, $\tau_c$ is the free-carrier momentum scattering time, $\varepsilon_0$ is the vacuum permittivity, $m^*$ is the effective mass of the electron–hole pairs in silicon, and $\rho_e$ is the electron density of the plasma. While various ionization and recombination mechanisms may be taken into account for the evaluation of $\rho_e$, a simple approach consists in accounting for the two-photon absorption only, yielding

$$\frac{\partial \rho_e}{\partial t} = \frac{\beta_2 |E|^4}{2\hbar\omega_0} \quad (2)$$

where, $\hbar$ is the reduced Planck constant. The assumption that two-photon absorption is the main ionization mechanism that occurs during femtosecond laser irradiation of silicon is strongly supported by the experimental results of ref. [57], where avalanche ionization could not be detected (see Section 3.1.1). Moreover, the absence of any recombination term in the kinetic equation for the plasma concentration [Equation (2)] was justified by experimental observations of the relatively long lifetime of the plasma (1–10 ns) induced by sub-picosecond pulses.[77,78,82]

This approach enabled Zavedeev et al. to calculate the evolution of the electron density produced in bulk silicon (at 700 µm from the entrance surface) by 250-fs duration pulses focused with a numerical aperture NA = 0.3 as a function of the input energy $E_{in}$ (**Figure 11**). There are two striking features in Figure 11. First, the electron density curve rapidly deviates from a linear regime (dashed lines) at extremely modest pulse energies (≈ 5 nJ). This threshold corresponds to the required input energy for reaching the critical power for self-focusing. Once it is reached, a competition between the optical Kerr effect and plasma defocusing occurs. Simultaneously, the significant absorption in the prefocal region leads to delocalization of the energy deposition. As a consequence, the intensity scales logarithmically as a function of $E_{in}$. This phenomenon often referred to as "intensity clamping" directly explains the experimental results presented in Section 3.1. The second major result of these simulations lies in the maximum electron density level reached. Given that the calculations have been made at 2-µm wavelength, the critical plasma density is $2.8 \times 10^{20}$ cm$^{-3}$. As shown in Figure 11, the calculated electron densities are one order of magnitude below this value, even for 10-µJ input pulse energy. This implies that femtosecond-laser induced plasmas in bulk silicon are subcritical, thus preventing enhanced energy deposition in the produced plasma. Taken together, these two results demonstrate that a simple increase in the input pulse energy is not an appropriate solution for achieving bulk modifications in silicon because of the nonlinear energy depletion well before the focus. In fact, such an increase in $E_{in}$ may result in ablation of the entrance surface before bulk modification since the limiting plasma effects are triggered at much higher intensities in air than in silicon. This is evidenced by the dashed curves on the right-hand side of Figure 11 showing a higher electron density level on the surface than in the bulk for $E_{in} = 10$ µJ.

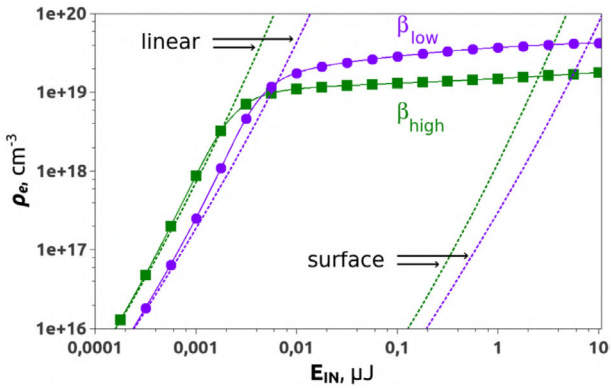


**Figure 11.** Evolution of the maximum electron density $\rho_e$ as a function of the input pulse energy $E_{in}$. The labels $\beta_{low}$ and $\beta_{high}$ designate different values for the two-photon absorption coefficient extracted from ref. [47]. The dashed lines on the left- and the right-hand side indicate the density which would be reached in the bulk in the case of a linear propagation and on the entrance surface, respectively. Laser wavelength: 2 µm; Pulse duration: 250 fs. Reproduced with permission.[102] Copyright 2016, IOP Publishing.

The wavelength dependence of femtosecond-laser–silicon interaction is an overriding issue for the design of experimental arrangements aiming at in-volume laser direct writing of the material. There is actually no intuitive solution for this problem as all the material properties are wavelength-dependent. On the one hand, increasing the wavelength can be beneficial as it leads to a decreased critical plasma density, a decreased multi-photon absorption in the prefocal region, and a more efficient avalanche ionization. On the other hand, it can also be detrimental due to the inevitably increased focal spot size as well as the decreased multi-photon absorption at the focus. In order to address this problem, Zavedeev et al. have carried out nonlinear propagation simulations over a broad wavelength range (i.e., not only limited to the two-photon absorption regime) under identical focusing

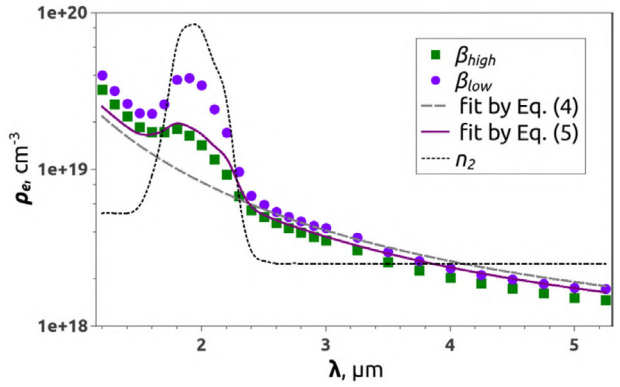


**Figure 12.** Evolution of the maximum electron density $\rho_e$ as a function of the laser wavelength $\lambda$ for 500-nJ pulse energy (NA = 0.3). The labels $\beta_{low}$ and $\beta_{high}$ designate different values for the multi-photon absorption coefficient extracted from ref. [47, 98, 103–105]. The calculated data are fitted in two different ways that account for the nonlinear refractive index $n_2$ or not. The curve corresponding to the nonlinear refractive index $n_2$ is in linear ordinate scale and explains the local maximum at the maximum Kerr-induced nonlinear focusing. Pulse duration: 250 fs. Reproduced with permission.[102] Copyright 2016, IOP Publishing.

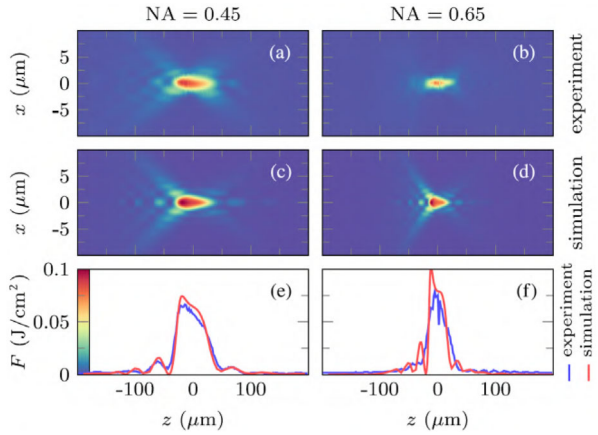


**Figure 13.** Comparison between a,b) experimental measurements and c,d) simulations of the fluence distributions for an ultrashort laser pulse focused in a 1-mm thick silicon sample with (left) NA = 0.45 and (right) NA = 0.65. The input pulse energy is 10 nJ. The corresponding e) experimental and f) simulated fluence distributions along the optical axis are displayed. Laser wavelength: 1.3 μm; Pulse duration: 60 fs. Adapted with permission.[15] Copyright 2016, American Physical Society.

conditions for high input pulse energy ($E_{in}$ = 500 nJ).[102] The term $\beta_2|E|^2E/2$ in Equation (1) was thus replaced by

$$\frac{1}{2}\sum_K \beta_K |E|^{2(K-1)}E \tag{3}$$

where $\beta_K$ is the $K$-photon absorption coefficient at the considered wavelength $\lambda$ according to the literature.[47,98,103–105] The corresponding results are displayed in **Figure 12** where the maximum electron density $\rho_e$ produced in the bulk of silicon decreases with increasing wavelength. This behavior was explained by the higher efficiency of the plasma defocusing when the wavelength is increased, thus responsible for the light delocalization. The overall trend is that the electron density scales as $1/\lambda^2$, so as the critical plasma density. One may note, however, the non-monotonic behavior of the curve around 2-μm wavelength corresponding to the peak in the nonlinear refractive index $n_2$ of silicon, thus increasing the importance of the optical Kerr effect with respect to plasma defocusing. While one could conclude that mid-infrared pulses are unfavorable for producing permanent modifications inside silicon, the authors also calculated the maximum delivered energy at different wavelength. In contrast with the overall decrease in the electron density, the delivered energy reaches a minimum in the 3-photon absorption regime (at ≈ 2.8-μm wavelength), before growing again in the 4- and 5-photon absorption regime. While this potential benefit has not been experimentally confirmed yet, this difference between electron density and delivered energy analyses originates from inverse bremsstrahlung absorption which is more efficient for long wavelengths.

As discussed in Section 2, the high refractive index of silicon implies relatively low angles in the material (i.e., < 17°). However, in some applications using hyper-NA configurations (e.g., micro-explosion experiments for producing new allotropic phases of silicon[106,107]), the paraxial approximation is not valid. In order to address this issue, Fedorov et al. have developed a simulation approach based on transformation optics for modeling laser-silicon interaction in high numerical-aperture configurations (NA ≥ 1)[15] without the need for vectorial treatments. Their scalar model relies on the unidirectional pulse propagation equation (UPPE) which is similar to the above-presented one (Equation 1), in the spectral domain. In order to simulate large angle wave vectors, the authors defined a scaled refractive index as $n_s = sn$, where $s$ is the scaling factor (typically on the order of 1000). In this way, the problem is transformed into an analog virtual situation where the wavefront curvature is drastically reduced. The original geometry can be retrieved by compressing the space along the optical axis by $s$ times. The authors have shown that the linear propagation calculated for NA ≥ 1 with their model was in excellent agreement with simulations using the rigorous vectorial theory. In the nonlinear case, the code was benchmarked with propagation measurements performed with 60-fs laser pulses at 1.3-μm wavelength, as shown in **Figure 13**. For each of the two employed numerical apertures, one may note that the shape of the fluence distribution is fairly well reproduced. Interestingly, the values for the maximum fluence reached in every configuration are particularly well-estimated. Therefore, the model with its transformation optics approach is an extremely powerful tool for estimating the dynamics of the energy deposition inside silicon. Moreover, as it will be shown in Section 3.3, this model is able to predict the experimental behavior of silicon under extremely tight focusing conditions (NA >> 1).

### 3.3. Bypassing the Single Femtosecond Pulse Limitations

Whereas, as presented in Section 3.2, the nonlinear propagation effects in silicon lead to an intensity clamping below the modification threshold, two main ways have been found for circumventing these limitations inherent to prefocal interactions. Nevertheless, both practical methods suffer from important drawbacks for an industrial perspective of laser direct writing applications. In this section, we present the techniques that are operational at

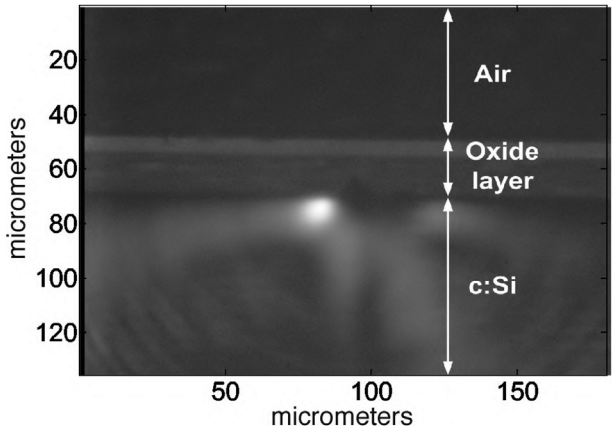


**Figure 14.** Near-field image of the end facet of a subsurface waveguide in silicon in which continuous light at 1.55-μm wavelength is injected. The waveguide has been inscribed by focusing 150-fs duration laser pulses at 2.4-μm wavelength with a Schwarzschild reflective objective of numerical aperture NA = 0.5. Reproduced with permission.[11] Copyright 2005, The Optical Society.

modest repetitions rates, that is, each individual pulse interacts with cold and relaxed material. The proposed solution relying on high repetition rates—and, thus, potential pulse-to-pulse accumulation regimes—will be presented in Section 4.3.

The first method to circumvent the intensity clamping is to minimize the amount of material in which the pulse propagates, and thus aims at modifications at low depth. However, this leads to important difficulties to avoid surface damage. In a pioneer paper, Nejadmalayeri et al.[11] added an amorphous silica (a-$SiO_2$) layer on the entrance surface of silicon and identified conditions to confine modifications near the interface. In an analogous configuration, Crawford et al. employed a carbon (a-C) layer.[12] The corresponding modifications are located close to the interface with the amorphous material (typically on the order of 10 μm below the interface), irrespective of the focusing depth. By moving the sample perpendicularly with respect to the incoming laser beam, Nejadmalayeri et al. have inscribed subsurface waveguides in silicon,[11] as shown in **Figure 14**. The associated refractive index change is $\approx 10^{-3}$, and the losses were estimated to be $\approx 1.2$ dB cm$^{-1}$. Nevertheless, the mechanisms making the permanent modifications possible were unclear. By carrying out numerical simulations of the nonlinear propagation inside silicon, Kononenko et al. showed that plasmas with relatively high electron densities can be produced in the subsurface of silicon during the interaction,[58] thus explaining the laser-induced modifications in this region. From an industrial point of view, besides its 2D limitations analogous to the silicon-on-insulator (SOI) technique, coating the silicon surface may be incompatible with some microelectronic devices, where a layer of insulator is undesirable.

The second method for producing modifications in bulk silicon with femtosecond laser pulses consists of employing hyper-NA configurations (i.e., numerical apertures well above unity) so that the intensity in the prefocal region is minimized. To do so, Sreenivas et al. have employed an oil immersion microscope objective of numerical aperture NA = 1.25 and index matching liquid of refractive index 1.49 for focusing in bulk silicon 800-fs duration laser pulses at 1.55-μm wavelength and a pulse energy of 50 μJ.[108] The authors reported buried structures in the material, which can be attributed to the higher intensity at the focus together with large angles of the cone of light which limit the plasma effects. While this technique is convenient for ensuring the immersion of the objective lens when the sample is moved during 3D inscription, the main drawback is the limited refractive index of liquids which can never perfectly match the one of silicon. Therefore, the general aforementioned refraction-based limitations still apply and make this methodology inapplicable with shorter pulses. In order to solve this issue, Chanal et al. proposed a solid immersion lens (SIL) technique relying on a spherical air–silicon interface.[18] To demonstrate this technique, 60-fs duration laser pulses at 1.3-μm wavelength were focused in the center of a 2-mm diameter silicon sphere with an objective lens of numerical aperture NA = 0.85. In this configuration schematically depicted in **Figure 15**, there is no refraction at the air–silicon interface, and the effective numerical aperture is thus the one of the objective lens multiplied by the refractive index of silicon $NA_{eff} = n_{c\text{-}Si} \times NA_{obj} = 2.97$. Supported by nonlinear propagation simulations with the model developed in ref. [15], these extreme focusing conditions produced the very first modifications induced in a deterministic way in bulk silicon with < 100-fs duration pulses. The remarkably low pulse energy sufficient for producing these modifications (20 nJ) as well as repeated experiments confirmed that the laser-produced modifications do not rely on defects inside the material. The refractive index change associated with these modifications is negative, suggesting that these may be voids or micro-cavities. While the liquid and solid immersion lens techniques applied for intense laser–silicon interaction have demonstrated that the nonlinear propagation limitations can be bypassed for producing material modifications, they suffer from drawbacks limiting their industrial applicability. For instance, the oil immersion technique requires to clean up the entrance surface after laser inscription. Similarly, while the solid immersion lens technique offers high-resolution inspection of silicon integrated circuits,[109,110] transposing it for laser processing in silicon requires a less-than-a-half-sphere positioned on a wafer surface to produce modifications similar to those shown in Figure 15. A writing procedure would then require moving this SIL on the entrance surface—thus, potentially provoking scratches. An additional difficulty is the need for a perfect optical contact between SIL and the substrate for taking advantage of the hyper-NA configuration as any air gap will simply make impossible to couple the high angular components. Finally, this SIL technique does not allow to modify the material at arbitrary depths—thus, restricting the inscription to a 2D geometry unless it is combined with complex adaptive optics solutions.

### 3.4. Underdense Plasmas—Applications

As developed in the whole Section 3, laser direct writing in bulk silicon with femtosecond pulses is extremely challenging due to nonlinear effects that limit the energy deposition inside the material. Nevertheless, the possibility to produce transient microplasmas inside silicon in a non-destructive way with ultrashort pulses offers other applications. The first of these concerns microelectronics. Indeed, because of their compactness, optical approaches

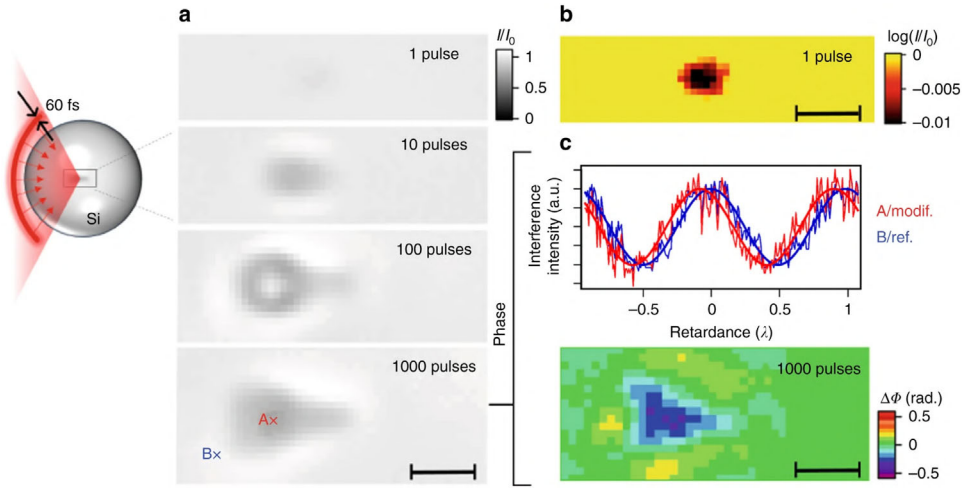


**Figure 15.** Micro-modification produced in bulk silicon with 60-fs duration laser pulses through a spherical interface. a) Bright-field images of the modifications for different number of applied pulses. b) Transmission image of a modification induced by a single pulse in logarithmic scale. c) Phase measurements of a modification induced by 1000 pulses including (top) an interferogram comparing the phase on the two points A and B indicated in a), and (bottom) a 2D phase image. Laser wavelength: 1.3 μm; pulse duration: 60 fs. Reproduced with permission.[18] Copyright 2017, Springer Nature.

are commonly employed since the 1960s to emulate radiation effects in microelectronic devices (e.g., gamma-ray-irradiated circuits in space applications),[111] and to investigate the possibility to handle free carriers in these devices (i.e., physical hacking). However, because of the technology available at that time, these techniques were limited to long-duration irradiations at wavelengths for which silicon linearly absorbs the laser flux (i.e., the photon energy is higher than the band gap of the material).[112–118] The laser energy deposition in this case is thus limited by the opaque metallic components on the frontside of the device. The later technological developments of femtosecond lasers as well as near-infrared lasers enabled to irradiate the device from the silicon substrate (i.e., the backside) by two-photon absorption—and, consequently, to generate free carriers with a remarkable spatial resolution.[119–134] The plasma production close to the logic gates of the irradiated device implies that some of the free carriers are able to migrate through a tunnel oxide so that the logic state of the microelectronic component (e.g., flash memory, photodiode) is modified in a stable manner after irradiation.

A second application of the femtosecond-laser produced underdense plasmas in silicon is spatial beam shaping. Faccio et al. reported a spontaneous reshaping of Gaussian-shaped beams to Bessel beams during the propagation in silicon for pulses at 1.55-μm wavelength with a peak power exceeding the critical power.[135] This reshaping was explained by the competition between Kerr nonlinearity and two-photon absorption together with plasma defocusing. In this configuration, two-photon absorption can be viewed as a semi-opaque stopper located in the center of the Gaussian beam leading to a diffractive transformation which is well-described by a Bessel function. Analogous plasma-shaped beams in silicon were recently reported by Pinhas et al. in a double-pulse configuration.[136] This technique consists of a pump beam at 532-nm wavelength for producing a plasma on the surface for shaping a parallel probe beam at 1.55-μm wavelength. Two probe beam shapes were obtained using this technique. The first one is a donut shape obtained by adjusting the pump beam size so that it is smaller than the probe. Conversely, the second shape is a narrow probe beam obtained for a donut pump beam. Once shaped, the probe beam was used to successfully overcome the resolution limit for microscopy in silicon. This stimulated emission depletion (STED) microscopy technique[137] is particularly meaningful for characterizing integrated circuits in micro- and nano-electronics.

Finally, femtosecond-laser produced underdense plasmas show applications for spectral manipulations in silicon. By the same way the spatial characteristics of the beam are modified by nonlinear propagation effects, one can also expect distortions in the temporal and spectral domain. During ultrashort-laser–matter interaction, several frequency generation processes may occur. By employing femtosecond laser pulses at 1550-nm wavelength, Kadan et al. demonstrated third-harmonic generation in silicon.[138] The steep electron density profile of the plasma is indeed a nonlinear optical medium suitable for frequency conversion.[139] This well-known phenomenon is the basis of high-harmonic generation[140] and attosecond science.[141] The surprising aspect of harmonic generation in silicon relies on the detection of the wavelength involved. Indeed, the third-harmonic generated light in ref. [138] is at 516-nm wavelength, which is strongly absorbed by silicon with a linear absorption coefficient of $8.8 \times 10^3$ cm$^{-1}$.[142] The relatively thin wafers (0.5 mm) used in the experiments made possible the detection of this light. In the same study, Kadan et al. also reported a spectral broadening of femtosecond laser pulses propagating through silicon, which was mainly explained by self-phase modulation. Given that the frequency blue-shift was larger than the red-shift, the authors also suggested that the blue-shifted light generated in silicon originates from plasma emission. Ultimately, by using ultrashort laser pulses at different mid-infrared wavelengths, Marcinkevičiūtė et al. recently demonstrated experimentally octave-spanning supercontinuum generation in silicon.[143] When generated by pulses at 4.7-μm wavelength, the supercontinuum covers the 2.5–5.8-μm wavelength range. No damage is

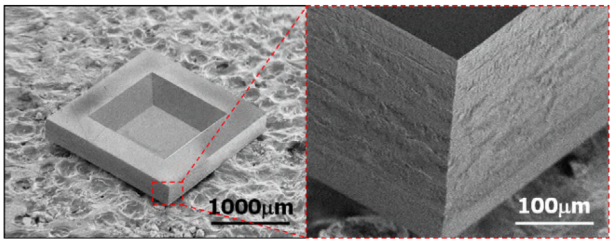


**Figure 16.** Scanning electron microscopy (SEM) images of microelectromechanical systems (MEMS) cut with the stealth dicing method. Courtesy of Hamamatsu Photonics K. K.

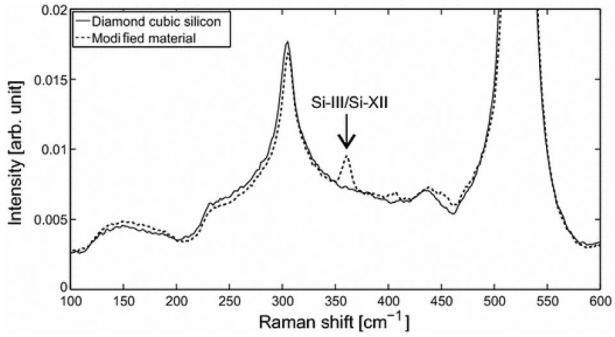


**Figure 17.** Raman spectrum of (solid) unmodified and (dotted) laser-modified silicon on a fracture plane. Laser wavelength: 1.55 μm; pulse duration: 3.5 ns. Reproduced with permission.[21] Copyright 2015, Springer Nature.

formed during this process for input pulse energies and durations on the order of 1 μJ and 100 fs, respectively, suggesting that, due to its high nonlinear coefficients (see Section 2), silicon is a suitable medium for supercontinuum generation.

## 4. Solutions for Laser Direct Writing in Silicon

### 4.1. Nanosecond Inscription

#### *4.1.1. Permanent Modifications Induced by Nanosecond Pulses*

One manner to drastically reduce the limiting nonlinear effects presented in Section 3 which are inherent to the propagation of femtosecond laser pulses in silicon is to employ longer pulses. In that way, nanosecond pulses were shown to be adapted for producing permanent modifications in the bulk of silicon during the 2000s.[144–147] The possibility to modify the material with such pulses has led to the development of a dicing technique called "stealth dicing," which is routinely employed in the industry for cutting large wafers into individual chips.[148] This technique relies on the inscription of modifications in the bulk of a silicon wafer with no surface damage. After this inscription, when pressure is applied onto the wafer, the modifications act as weak points, facilitating the breakage. The wafer is thus diced along the laser-defined directions. In contrast with other methods such as mechanical dicing (e.g., blade dicing) or laser drilling, stealth dicing offers numerous advantages,[144] including high processing speed, the absence of debris or contaminants, and steep edges as illustrated in **Figure 16**.

The stealth dicing technique introduced in refs. [144–147] was demonstrated for thin wafers (50–500 μm) at wavelengths in the 1.03–1.10 μm range. Other groups employed these wavelengths for applications such as backside machining of 380-μm thick silicon wafers.[149] One must note that this wavelength range corresponds to photon energies ≥ 1.13 eV, slightly above the one of the band gap of silicon at room temperature (1.12 eV).[39–41] In other words, the material transparency to these wavelengths is extremely limited, as indicated by the linear absorption coefficient ≥ 3.5 cm$^{-1}$.[142] Such a high linear absorption coefficient is an important hurdle to overcome for the stealth dicing of thicker wafers. The development of near-infrared lasers enabled Verburg et al. to show that permanent modifications could be produced in bulk silicon in the two-photon absorption regime with nanosecond pulses at 1.55-μm wavelength.[16] These modifications could be created at various depths of thin wafers (160-μm thickness). In later works, Verburg et al. also analyzed the crystalline structure of the laser-irradiated zones with Raman spectroscopy.[21,150] These characterizations highlighted that the modifications consist of transformations of the initially crystalline silicon to amorphous and polycrystalline silicon as shown by the peak corresponding to the Si-III/Si-XII phases in **Figure 17**. The localization of the energy deposition in the two-photon absorption regime was then investigated by Yu et al. in silicon samples with different doping concentrations.[151] Their study showed that, for low doping concentration samples with electron densities $n_e \leq 10^{16}$ cm$^{-3}$, similar modifications could be produced inside silicon. However, for highly doped silicon ($n_e = 10^{18}$ cm$^{-3}$), where linear absorption cannot be neglected,[152] the modifications in the focus region are way smaller.

The possibility to produce permanent modifications of the crystalline structure of silicon with nanosecond laser pulses in the two-photon absorption regime has led other groups to systematically investigate the material changes that could be obtained with such pulses. To do so, electron microscopy coupled to electron diffraction analyses offers an extremely remarkable way to characterize these changes at the nanometer scale. A wide variety of material changes induced by nanosecond pulses was discovered, including voids,[22,153] high-pressure phases,[154] dislocations,[27,28,155,156] hydrostatic compressive strain,[27,28,155,156] cracks[22] as well as polycristalline features.[19,154] As illustrated by the transmission electron microscopy (TEM) image with the selective area electron diffraction images in **Figure 18**, several types of material changes may coexist in the same laser-irradiated zone. Considering all the fundamental processes taking place during and after the nanosecond laser pulse (including carrier excitation, thermal and mechanical events[157]) before resolidification, one could expect this coexistence. All the aforementioned material changes are associated with different optical properties showing high potential for a broad range of applications in photonics.

Given the high transparency of silicon at 1.55-μm wavelength, Li et al. showed the possibility to modify the material at depths up to 2 mm below the surface.[158] By means of infrared quantitative-phase microscopy, the authors investigated the refractive index change associated to laser-induced modifications in various conditions (i.e., different number of pulses per location and pulse energy). Consistently with the above discussion, the modified zones show coexisting positive and negative refractive index

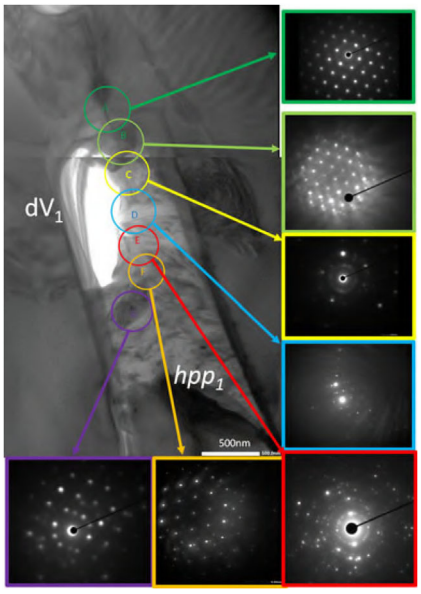


**Figure 18.** Transmission electron microscopy image of a laser-induced modification. The insets correspond to different selective area electron diffraction images taken at various positions of the modification. The notations $dV_1$ and $hpp_1$ correspond to "decorated void" and "high pressure phase," respectively. The zones A, B, D, and F show typical features from mono-crystalline silicon, and the zones E and G exhibit Debye–Scherrer rings associated with polycristalline silicon. Laser wavelength: 1.34 µm; Pulse duration: 90 ns. Reproduced with permission.[154] Copyright 2018, Oxford University Press.

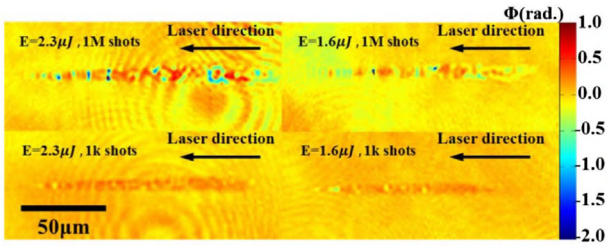


**Figure 19.** Phase images of four microstructures created in the indicated laser conditions in terms of pulse energy and number of applied pulses. A positive and negative phase shift Φ corresponds to a positive and negative refractive index change, respectively. Laser wavelength: 1.55 µm; pulse duration: 5 ns. Reproduced with permission.[158] Copyright 2016, The Optical Society.

changes, as illustrated by the top images in **Figure 19**. This is linked to the creation of micro-cavities/porosity and densified regions. Nevertheless, by using phase microscopy for characterizing the modifications, it was shown in the experiments that nearly uniform positive refractive index changes could be produced under specific laser conditions (see the bottom images in Figure 19).

#### *4.1.2. Structuring through Nonlinear Feedback-Driven Collective Pulse–Material Interactions*

Traditional laser-material processing methods rely on a laser beam modifying different points on or inside a material essentially independently, whether the process is serial, as in laser direct writing, or in parallel, as in lithography. The sequence in which the modification is made does not matter, except for trivial geometric dependencies, such as a previously modified point blocking access. An alternative approach is to exploit intrinsic nonlinear feedback mechanisms that arise in laser–matter interactions in the strongly nonlinear regime, for which silicon is a well-suited platform. In this approach, when a laser pulse modifies the material, the change in the material properties influences how the next pulse interacts with the material, creating an iterative process resulting in a self-organized structure even when the laser beam is stationary. The influence of a given pulse within a sequence of pulses depends on the entire history of modifications by the previous pulses. Thus, a large number of pulses interact collectively with the target material over a finite but spatially extended region. This approach opens up new possibilities in laser-material structuring, especially when point-by-point modification is difficult to achieve. One obvious limitation of this approach is that any overall pattern must comprise these self-organized structures.

The rich history of the creation of well-controlled self-organized patterns dates back to the fluid convection experiments of Bénard in 1900.[159,160] The first use of a laser beam to create permanent self-organized structures was shown within a few years of the laser invention.[161] However, the first unambiguous identification and deliberate exploitation of the intrinsic nonlinear feedback mechanisms to achieve laser-induced self-organization appears to be more recent.[162] Its first application was the creation of surface nanostructures of unprecedented uniformity.[162] Additional demonstrations of such similar feedback-driven collective interactions by the same authors are described in refs. [163–165].

The first application of this approach to the in-volume refractive index structuring of silicon was shown in ref. [19], and included the first selective chemical etching to create 3D structures out of silicon using the wavelength of 1.55 µm. There, Tokel et al. showed that it is possible to modify the material within its bulk, without altering the wafer above or below the modifications, and with strong 3D control.[19] The achieved refractive index contrast of $5 \times 10^{-4}$ is due to a localized disturbance of the crystal, based on stress and strain effects.[19] The authors circumvented the speed limitations of point-by-point writing (this will be shown in **Figure 31**), with the creation of self-organized rod-like structures which are formed along the beam propagation direction (**Figure 20**a). Here, the laser is partially reflected from the exit surface due to Fresnel reflection, creating nonlinearly coupled counter-propagating beams within the semiconductor. The nonlinear interactions described in ref. [19] cause the beams to collapse, triggering the self-organized pulse-to-pulse growth of rod-like structures, which extend hundreds of micrometers while preserving their 1-µm thickness (Figure 20a). With this approach, the fabrication speed increases rapidly compared to point-by-point fabrication, and the structures elongate without physically changing the laser focus as in conventional approaches. For instance, with a single circular motion of the laser, which can be performed in seconds, one can create a high-aspect ratio in-chip cylinder of > 700-µm length with 1-µm resolution (Figure 20b). The authors also developed a hydrofluoric acid (HF) based selective chemical etching approach to remove the laser

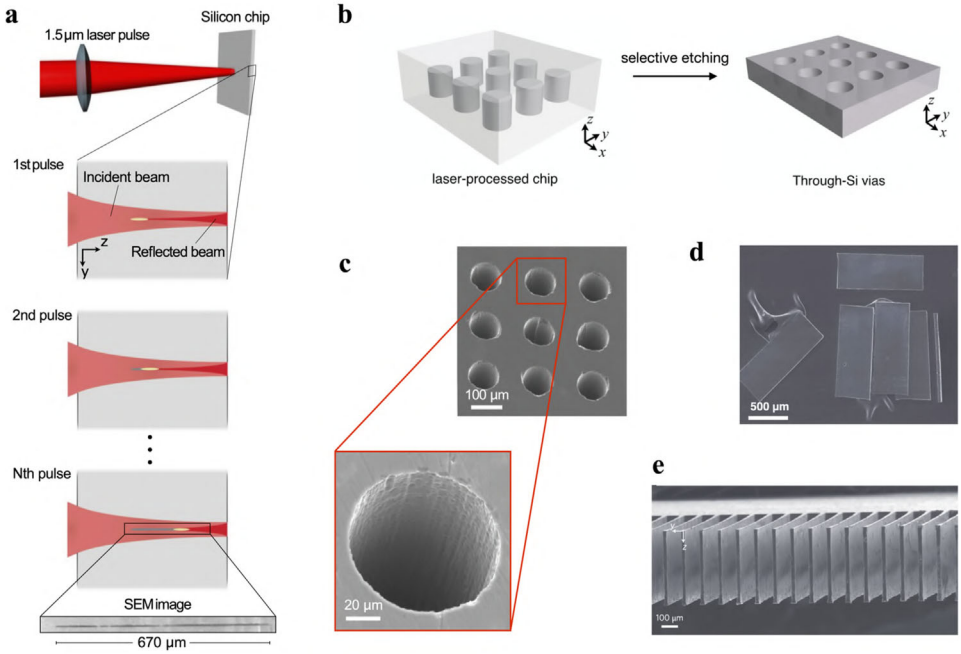


**Figure 20.** a) Schematic showing laser pulses incident on a silicon wafer to create elongated structures. The reflected beam couples to the incident beam, and collapses to modify the wafer. Consecutive pulses focus to shifted positions, elongating the in-chip structure. Inset: scanning electron microscopy (SEM) image of a 670-μm-long elongated structure in silicon, preserving 1-μm thickness. b) The elongated structures created in (a) can be used as a building block for more complex architectures. Exposing the structures to a selective etchant enables creation of 3D shapes. c) SEM image of an array of through-silicon vias cutting through > 700 μm, each created with a single circular motion of the laser. d) SEM image of laser-sliced silicon with 30-μm thick platelets. e) SEM image of micro-plate array; with removed parts corresponding to thin platelets given in d). Laser wavelength: 1.55 μm; pulse duration: 5 ns. Adapted with permission.[19] Copyright 2017, Springer Nature.

written parts, without significantly effecting the non-irradiated crystal (Figure 20b). Thus, by exposing the modified areas to the solution, high aspect-ratio through-silicon vias can be sculpted in a few minutes (Figure 20b,c). These vias elongate hundreds of micrometers, and each one is created with a single circular motion of the laser, notably created without changing the depth of the laser focus (Figure 20c). Such a capability may have significant advantages in the industry, where the fabrication speed is critical. Furthermore, the capability is not limited to circular symmetry. For instance, an in-chip rectilinear pattern can be converted to large-volume covering micro-pillar arrays (**Figure 32**) or micro-plate arrays (Figure 20e). Another application would be in ultra-thin laser-slicing of silicon (Figure 20d),[19] for instance, in the form of pieces removed from the architecture given in Figure 20e.

#### *4.1.3. Nanosecond Laser–Matter Interaction Models*

In the femtosecond regime, the difficulties for modeling laser–matter interaction are generally related to the nonlinear propagation of an intense laser pulse. Nevertheless, due to the timescale of femtosecond laser pulses, below the electron–phonon scattering time of 1–10 ps,[157,166–168] it is possible to separate the causes (i.e., the carrier excitation), from the consequences (i.e., the material response). Due to reduced optical Kerr effect in the nanosecond regime, one may intuitively guess that the beam propagation is linear. However, thermal and other nonlinearities render the propagation highly nonlinear. In particular, during the interaction, the material properties dynamically change (e.g., carrier density, optical index, temperature, pressure, internal energy), leading to a complex interaction dynamics between the laser and the material. A full model would ideally account for the phase changes, the rise in temperature, the material movement, the dependence of almost every single material parameter on the temperature, the formation of pressure and shock waves, hydrodynamic phenomena, etc. While, in principle, this full model could be developed for well-known materials such as silicon, several groups have chosen a simplified approach for explaining the experimental results they obtained.

A first theoretical approach for modeling nanosecond-laser–silicon interaction was developed by Ohmura et al.[145] This model consists of evaluating the increase in temperature $\Delta T$ provoked by a laser pulse of 150-ns duration at 1.06-μm wavelength, by calculating (i) the internal heat generation, and (ii) the intensity of a focused beam thanks to Beer–Lambert law with a temperature-dependent linear absorption coefficient $\alpha(T)$.[169] Linear propagation was considered, which is reasonable regarding the subcritical power conditions ($P \approx 30$ W). The calculated evolution of the temperature as a function of the depth is displayed in **Figure 21** at different times. In these simulations, the temperature drastically increases near the focal region ($z =$ 60 μm) during the beginning of the pulse. The striking feature in Figure 21 is the development of an absorption front upstream the incoming laser during the pulse. This behavior is well-known in wide band-gap materials irradiated by nanosecond pulses due to the cooperation of different mechanisms including band-gap

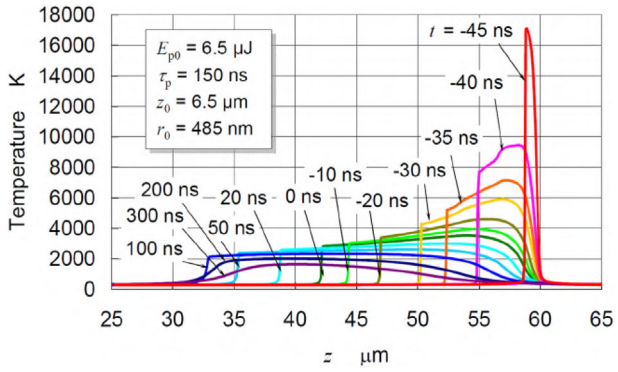


**Figure 21.** Evolution of the calculated temperature as a function of the distance $z$ along the optical axis at various times. The time 0 ns refers to the temporal maximum intensity. Laser wavelength: 1.06 μm; pulse duration: 150 ns. Reproduced with permission.[147] Copyright 2011, IntechOpen.

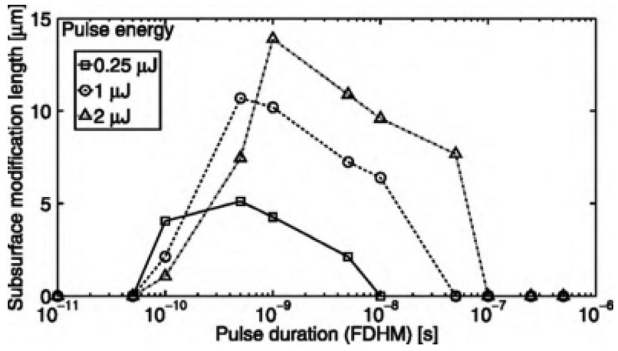


**Figure 22.** Subsurface modification length as a function of the pulse duration [full-duration at half-maximum (FDHM)] and the pulse energy. The beam with a quality factor $M^2 = 1.30$ is focused at a depth of 100 μm under the silicon surface with an objective lens of numerical aperture NA = 0.7. Laser wavelength: 1.3 μm. Reproduced with permission.[171] Copyright 2014, Springer Nature.

collapse, heat diffusion and free-carrier transport.[170] As shown in Figure 21, an analogous behavior is obtained in the linear absorption case, which enabled the authors to explain the elongated morphology in the prefocal region of the modifications.

A more sophisticated model was developed by Verburg et al. for evaluating the size of the modifications in the two-photon absorption regime (at 1.3-μm wavelength).[171] The approach of the authors relied on a two-temperature model for calculating the increase in temperature in silicon. The propagation is assumed to be shape-invariant. The damage criterion in this model corresponds to the melting temperature of silicon (1687 K[52,53]). Simulation results are displayed in **Figure 22** for various pulse durations and energies. For all pulse energies, there is a narrow duration window in which modifications can be produced. Additional simulations (not shown here) demonstrated that two-photon absorption and heat diffusion are the main contributions for explaining this window behavior. For too long pulses (≥ 100 ns), the intensity is not high enough for producing sufficient electron density—and, thus, for reaching the melting temperature of silicon. On the other hand, when the pulses are too short (≤ 50 ps), a plasma is formed in the prefocal region and provokes undesired absorption by the free carriers. However,

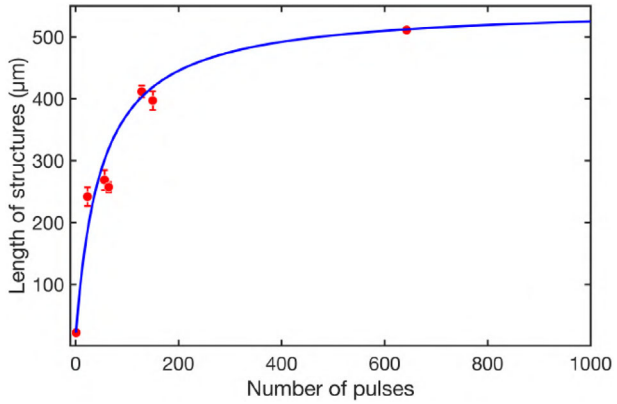


**Figure 23.** Length of laser-induced modifications experimentally measured (red circles), and the toy model prediction (solid line). The error bars correspond to standard deviations from averaging lengths of 20–30 subsurface modifications. Laser wavelength: 1.55 μm; pulse duration: 5 ns. Reproduced with permission.[19] Copyright 2017, Springer Nature.

one should note that, at these short durations, the critical power for self-focusing in silicon is exceeded, and the shape-invariant approximation of the model is not valid anymore due to the competition between the optical Kerr effect and plasma defocusing.

This competition between opposing mechanisms inducing opposite refractive index changes during the propagation of nanosecond pulses in the bulk of silicon represents another degree of complexity which was accounted for in the "toy model" developed by Tokel et al.[19] The goal of this model is to predict the size of the modifications after a sequence of consecutive pulses. The experimental irradiation conditions enabling the production of these modifications include the reflection at the exit silicon–air interface. The back-reflected light is then focused in the bulk of silicon. The model takes into account the laser propagation by means of the nonlinear paraxial equation with a varying refractive index change. The contributions of the index change are the optical Kerr effect, the temperature change inside the material, and plasma defocusing. The electron dynamics include ionization (by two-photon absorption) and Auger recombination. The heat source term can thus be calculated and injected in the heat equation (Fourier's law). By repeating the calculations on a pulse-to-pulse basis, the total length of the modifications $l_{total}$ after $N$ successive pulses can be calculated as[19]

$$l_{total} = \frac{l_1}{1 + \xi/(N-1)} \tag{4}$$

where $l_1$ is the focal position of the first pulse, $\xi = f_{FCI} f_{therm} / l_1 (f_{FCI} + f_{therm})$ is constant, $f_{FCI} < 0$ is the focal length associated with the refractive index change induced by the free carriers, and $f_{therm} > 0$ is the focal length associated with the thermally induced refractive index change. As shown in **Figure 23**, the model described by Equation (4) is accurate for predicting the length of the modifications measured experimentally.

Recently, Kiyota et al. proposed an advanced thermomechanical model for predicting the characteristic geometrical features of zones in different material states present in laser-induced modifications.[172] In this model, calculations of the beam propagation under the paraxial approximation are

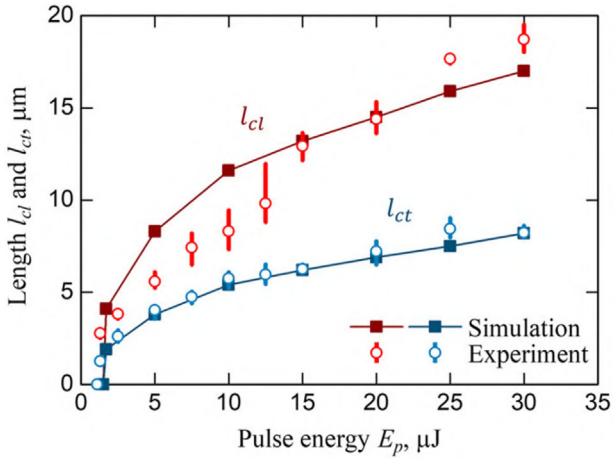


**Figure 24.** Comparison between the experiments and the simulated crack front dimensions as a function of the pulse energy. The laser beam is focused 82 µm below the silicon surface with a numerical aperture of NA = 0.75. The lengths $l_{cl}$ and $l_{ct}$ correspond to the radii of the ellipse-shaped crack front along and perpendicularly to the laser flux, respectively. Laser wavelength: 1.34 µm; pulse duration: 45 ns. Reproduced with permission.[172] Copyright 2020, American Institute of Physics.

performed by solving the nonlinear Schrödinger equation (NLSE) including the optical Kerr effect and plasma defocusing. The kinetic equation for plasma concentration includes linear and two-photon absorption as well as Auger recombination. Finally, heat diffusion and mechanical processes such as the generation of residual stress (through Hooke's law) and cracks (through Von Mises stress criterion) are taken into account. The proposed method allowed the authors to distinguish the different phases formed inside silicon after a single nanosecond irradiation, including voids, molten, recrystallized, and densified silicon. The simulation results were then compared to experimental data obtained for modifications produced at 1.34-µm wavelength, as illustrated in **Figure 24** for the dimensions of the crack front. The good agreement confirms that the proposed model is able to predict the morphology of nanosecond-laser induced modifications inside silicon. In their work, Kiyota et al. have also shown that their model could predict the position of densified silicon zones with respect to the geometrical focus of the laser beam.

#### *4.1.4. Positive Refractive Index Changes—Applications*

The possibility to control the refractive index of silicon with nanosecond laser pulses makes these pulses a fantastic tool for refractive index engineering. In that way, Chambonneau et al. demonstrated the possibility to inscribe longitudinal lines (i.e., along the optical axis) inside the material.[24] As shown by the phase images in **Figure 25**, the line morphology is strongly dependent on the writing speed. For high ($\geq$ 1.0 mm s$^{-1}$) and low speed ($\leq$ 5.0 µm s$^{-1}$), the lines consist of a mix between positive and negative index change, which can be attributed to the single-pulse configuration and accumulation effects, respectively. Interestingly, for 0.1-mm s$^{-1}$ writing speed, the lines exhibit only a positive index change, which is approximately $\Delta n = 5.3 \times 10^{-3}$ (assuming a cylindrical symmetry). These structures represent the first waveguide inscription deep inside monolithic crystalline

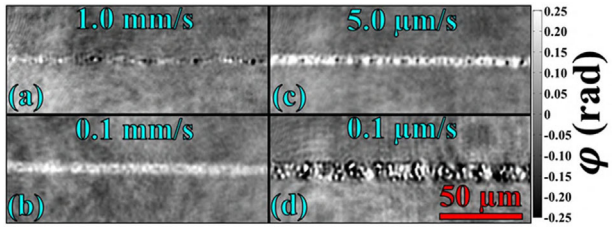


**Figure 25.** Phase images of lines inscribed inside silicon at the four indicated writing speeds, 2.0-µJ pulse energy, and 1-kHz repetition rate. Laser wavelength: 1.55 µm; pulse duration: 5 ns. Reproduced with permission.[24] Copyright 2016, The Optical Society.

silicon, as confirmed by the injection of light inside the lines and the detection of the scattered light. Later works of the same group have shown that, by applying the same method, it is also possible to inscribe Y-splitters longitudinally.[173]

One could wonder about the origin of the positive refractive index change associated with the written waveguides. Given the higher refractive index of amorphous silicon[174] $n_{a\text{-}Si} = 3.73$[175] compared to the one of crystalline silicon $n_{c\text{-}Si} = 3.48$ (at 1.55-µm wavelength[44]), one could expect a partial amorphization of the material for explaining the waveguiding properties. In a later study, Chambonneau et al. investigated the material changes at the nanometer scale.[28] To do so, the surface perpendicular to the waveguides was chemically etched with a diluted potassium hydroxide (KOH) solution. Due to the lower etching rate in the waveguide zone compared to non-irradiated silicon, the waveguides become visible and form a pyramid shape on the surface (**Figure 26**a). After etching, the modifications can be precisely located, and a thin lamella could then be prepared for the TEM observations displayed in Figure 26b,c, where the anatomy of the waveguide is clearly visible. This is possible either if the allotropic form of silicon has been modified, or if local strain is present inside the material. Given that the electron diffraction pattern in Figure 26d exhibits no change in the mono-crystalline structure, the waveguiding properties are more likely to originate from local strain fields. This was also confirmed with the Raman spectrum in Figure 26e, where only the features associated with mono-crystalline silicon according to ref. [176] (indicated with blue arrows) were exhibited. Indeed, features inherent to amorphous silicon such as a broad band around 480 cm$^{-1}$[177] are absent.

While longitudinally-written waveguides represent a proof of concept for positive refractive index engineering, the working distance of the employed focusing systems generally makes them inconvenient for long waveguide inscription. Transverse inscription is thus preferred for this purpose. However, Gaussian beams focused in a homogeneous medium through a plane surface, systematically show a Rayleigh length $z_R$ larger than the beam waist $w_0$ (i.e., the radius at $1/e^2$). Under the paraxial approximation, one can estimate the ratio between $z_R$ and $w_0$ as

$$\frac{z_R}{w_0} = \frac{n}{\mathrm{NA}} \tag{5}$$

where $n \geq 1$ is the refractive index of the medium, and NA $< 1$ is the numerical aperture of the focusing system. Therefore, while waveguides inscribed longitudinally with Gaussian pulses naturally exhibit a cylindrical symmetry, Equation (5) implies that

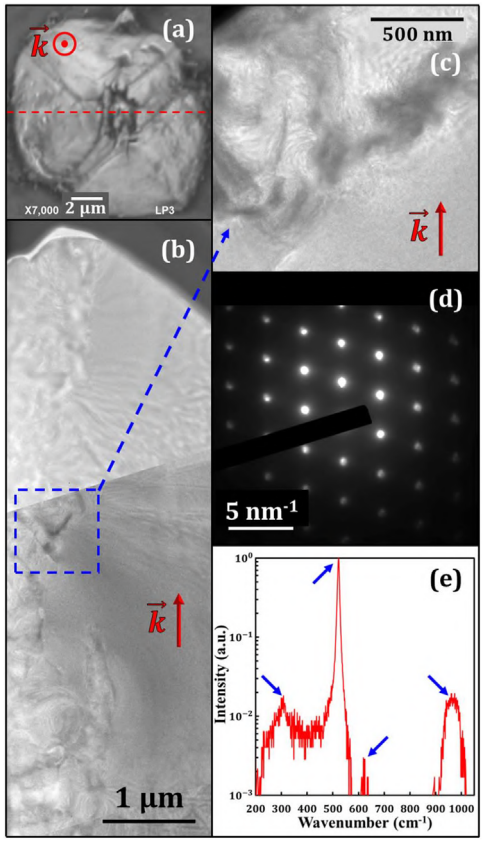


**Figure 26.** a) SEM image of a waveguide written at 0.1-mm $s^{-1}$ speed, and 0.9-µJ pulse energy after KOH etching. b) TEM image of the same site corresponding to the dotted red line in a). c) TEM magnification of the dotted blue square in b). The vector $\vec{k}$ shows the laser propagation direction. d) Electron diffraction pattern observed in c). e) Micro-Raman spectrum of the site observed in a), with mono-crystalline features of silicon according to ref. [176] indicated by the blue arrows. Laser wavelength: 1.55 µm; pulse duration: 5 ns. Reproduced with permission.[28] Copyright 2019, The Optical Society.

transverse writing intrinsically leads to waveguides with an elliptical cross section, which could be a hurdle for some applications. In order to write waveguides transversely, elliptical beam shaping is usually the simplest solution. In glasses, this can be experimentally guaranteed by the use of a cylindrical telescope[178] or a slit[179] before focusing. By breaking the symmetry of the Gaussian beam before focusing, the effective numerical aperture is different along two directions perpendicular to the optical axis. Therefore, by selecting the appropriate beam shape before the focus, the cross section of the beam becomes circular in one plane in the focal region. As stated by Equation (5), the higher the refractive index $n$, the more astigmatic the beam has to be. This challenge in silicon ($n \approx 3.5$) was recently taken by Wang et al., who first showed the possibility to transversely inscribe lines in the nanosecond regime with a circular cross section thanks to astigmatic beam shaping.[180] This achievement was the preliminary step for the inscription of centimeter-long straight and curved waveguides inside silicon as shown in **Figure 27**. Measurements of the numerical aperture of the single-mode waveguide NA = 0.038 yielded an estimated refractive index change

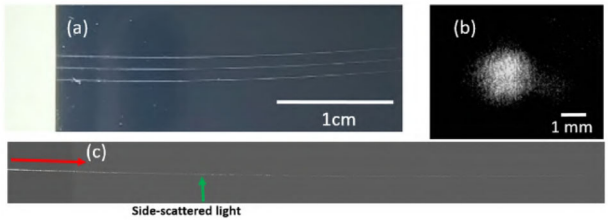


**Figure 27.** Laser-written curved waveguides in bulk silicon. a) Surface marks on the silicon sample indicating the location of the curved waveguides in the bulk. b) Far-field intensity profile of guided light at the waveguide output. c) Scattered light image. The red arrow indicates the light propagation direction. Laser wavelength: 1.55 µm; Pulse duration: 3.5 ns. Reproduced with permission.[181] Copyright 2020, American Institute of Physics.

$\Delta n = 2.0 \times 10^{-4}$.[181] Power measurements before and after the inscribed waveguide showed losses around 3.3 dB $cm^{-1}$. In the case of curved waveguides with various curvature radii in the 0.2–6-cm range, the authors measured additional bending losses ranging from $5 \times 10^{1}$ dB $cm^{-1}$ down to $2 \times 10^{-3}$ dB $cm^{-1}$.[182]

Another type of functionalization thanks to transverse writing consists of inscribing diffraction gratings inside silicon. This was demonstrated in ref. [27] where gratings with various periods $\Lambda$ were transversely written. Typical diffraction patterns recorded after the injection of continuous light through the gratings are displayed in **Figure 28**a. The experimentally measured efficiency of the grating is compared in Figure 28b to the predictions of a model relying on rigorous coupled-wave analysis,[183] where the refractive index change $\Delta n$ of the lines is a fitting parameter (the geometry of the lines composing the gratings having been characterized). The best agreement between theory and experiments was obtained for $\Delta n = 3.0 \times 10^{-3}$, which is very close to the value $\Delta n = 3.6 \times 10^{-3}$ measured with phase microscopy. The simulations do not reproduce the orders ±5 and ±6 due to the limited dynamic range of the employed camera. Besides the applications related to the writing of an additional function inside silicon, the agreement between experiments and theory provides another way to estimate the positive refractive index change of laser-inscribed modifications inside silicon, similar to what exists in glasses.[184] Noteworthy, the diffraction grating inscription demonstrated in ref. [27] in the two-photon absorption regime (at 1.55-µm wavelength) was recently transposed to the linear absorption regime (at 1.06-µm wavelength) in thin silicon wafers (300-µm thickness).[185]

#### *4.1.5. Negative Refractive Index Changes—Applications*

Besides the waveguides based on positive index changes as discussed in Section 4.1.4, another way is to take advantage of the negative index changes for the inscription of depressed-cladding waveguides. Despite their leaky nature when the refractive index of the core is identical to the one of the substrate,[186] these waveguides usually show excellent performance in terms of losses, and the core diameter is easier to adjust experimentally. A proof of concept of longitudinal inscription of depressed-cladding waveguides in crystalline silicon with nanosecond laser pulses was first demonstrated by Tokel et al.[19] and meticulous waveguide analyses were presented by Turnali et al.[26] As shown in **Figure 29**,

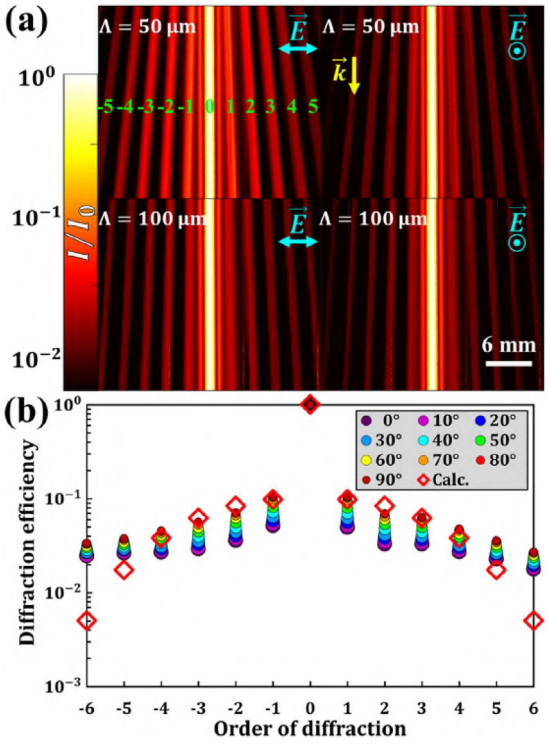


**Figure 28.** a) Diffraction patterns normalized to the 0th order obtained on gratings with indicated periods $\Lambda$ for an incident polarization indicated by the vector $\vec{E}$. The vector $\vec{k}$ shows the laser propagation direction. b) Diffraction efficiencies for a grating period $\Lambda = 50$ μm, at the indicated polarizations. 0° and 90° stand for a polarization parallel and perpendicular to the lines, respectively. The circles are measurements, and the empty red squares are calculations at 90° according to ref. [183]. Laser wavelength: 1.55 μm; pulse duration: 5 ns. Reproduced with permission.[27] Copyright 2018, The Optical Society.

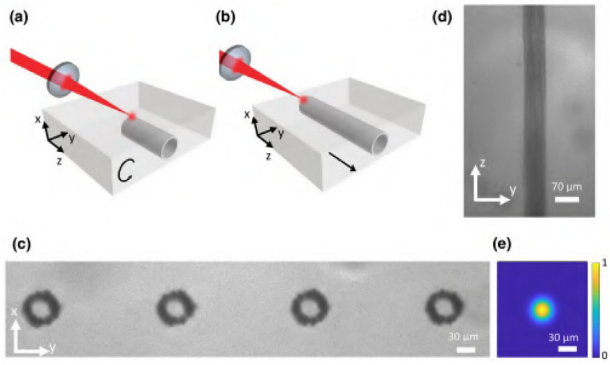


**Figure 29.** a) Longitudinal-writing technique used to form depressed-cladding waveguides deep inside crystalline silicon. Concentric circles are written at a specific depth by rotating the sample. b) Same procedure used at different depths along the optical axis. c) Infrared transmission microscopy image showing the circular cross-section from a waveguide array, positioned 500 μm from the top surface. d) Infrared image of the top view of a single waveguide where rod-like structures are used to form the cladding. e) Finite-difference time-domain (FDTD) simulation showing the mode field profile. Laser wavelength: 1.55 μm; pulse duration: 5 ns. Reproduced with permission.[26] Copyright 2019, The Optical Society.

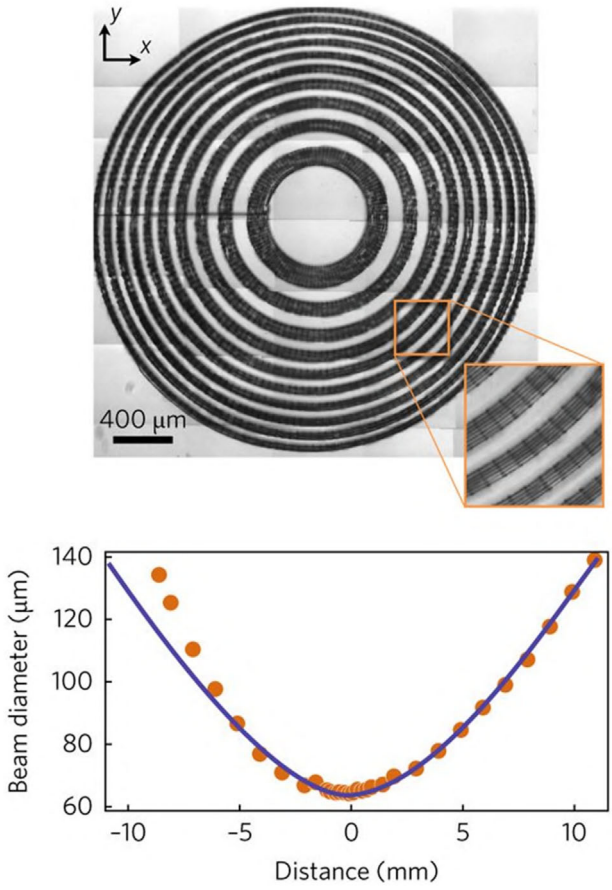


**Figure 30.** Top: composite infrared transmission microscope image of a subsurface Fresnel zone plate lens. Inset: close-up view. Bottom: theoretical and experimental beam profiles during focusing. Laser wavelength: 1.55 μm; pulse duration: 5 ns. Reproduced with permission.[19] Copyright 2017, Springer Nature.

the waveguides are composed of tubular modifications exhibiting a refractive index change $\Delta n = -3.0 \times 10^{-4}$ as measured with an interferometric method. By injecting light inside the 2.9-mm long structures, the authors confirm their waveguiding properties with a single-mode operation at 1.3-μm wavelength (core diameter: 30 μm). Measurements of the numerical aperture of the waveguides (NA = 0.034) revealed a refractive index change value $\Delta n = -1.6 \times 10^{-4}$, thus confirming the order of magnitude of the refractive index change. As expected, the waveguide losses $\alpha = 2.2$ dB cm$^{-1}$ obtained by analyses of the scattering light are remarkably low. Power measurements at the output of the waveguide showed even lower losses ($\alpha = 1.4$ dB cm$^{-1}$).

While we concentrated so far on the inscription of optical elements that guide[24,26,181] and disperse[27] light inside silicon, it is possible to write lenses as well. In that way, Tokel et al. demonstrated the inscription of Fresnel zone plates in crystalline silicon by writing concentric rings exhibiting a negative refractive index change (top image in **Figure 30**).[19] Measurements of the propagation after the Fresnel zone plate are in good agreement with theoretical predictions (bottom image in Figure 30). The light is focused down to a diameter close to 60 μm. The focal lens of the fabricated optical element is $f = 7.3$ cm at 1.55-μm wavelength.

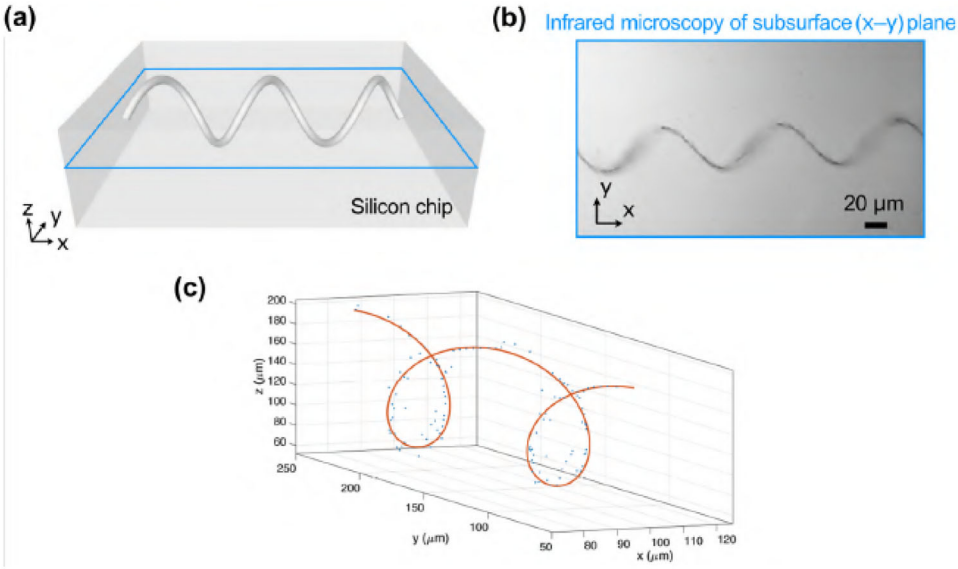


**Figure 31.** a) A schematic representing a 3D in-chip architecture. b) Planar cross-section of a laser-written helix recorded with infrared transmission microscopy. The out-of-focus parts of the image correspond to modifications remaining outside the depth-of-focus of the imaging objective. c) Complete experimental reconstruction of the 3D helix architecture. The blue dots are retrieved from 64 microscope images, whereas the red curve indicates the track of the laser focal positions writing at different depths. Laser wavelength: 1.55 µm; pulse duration: 5 ns. Adapted with permission.[19] Copyright 2017, Springer Nature.

The beam quality factor is $M^2 = 1.46$ with a diffraction efficiency of 15%.

A particularly interesting potential of laser direct writing is making use of the third dimension inside transparent materials. The third dimension has already been exploited in diverse materials, such as various polymers and glasses, with exciting applications in multiple fields.[168,187–192] Tokel et al. have demonstrated an analogous multi-dimensional fabrication capability in the bulk of silicon.[19] The authors used nanosecond pulses at 1.55-µm wavelength with optimized energy and focus, in order to fabricate various 3D shapes and in-chip architectures. **31a** shows a representative schematic of a buried 3D architecture. The laser-written structure can be revealed with infrared transmission microscopy. For instance, Figure 31b shows a cross-sectional subsurface plane, indicated with the blue rectangle in Figure 31a. The complete helix structure may be reconstructed from 64 microscope images (Figure 31c), following the path of the laser focus at virtually any depth inside the wafer, creating 3D architecture with high fidelity. The 1-µm resolution and point-by-point writing approach may limit the fabrication speed, however, the fabricated in-chip structures in principle may be extended to a rich set of applications, with significant potential in microfluidics, microelectromechanical systems (MEMS) as well as micro- and opto-fluidics.[168]

Negative refractive index changes may also be used for the fabrication of micro-devices. Analogously to the stealth dicing technique combining laser direct writing and the application of a mechanical force as described in Section 4.1.1, laser direct writing can be coupled with selective chemical etching to fabricate such micro-devices with an extraordinary degree of control as illustrated in **32**.[19] The technique relies on nanosecond irradiation in the bulk of silicon resulting in the production of voids and micro-cavities inside the material. During selective chemical etching, the laser-induced porosity facilitates the chemical solution to penetrate into the material. In other words, the laser irradiation enables to control the etching rate of the material. After chemical etching, the material is structured following a pattern related to the laser inscription. It is thus possible to fabricate complex structures in silicon by tailoring the refractive index change. Noteworthy, this negative-tone structuring induced by the negative refractive index change has its positive-tone equivalent for positive refractive index change, which decreases the etching rate of the chemical solution due to the presence of local strain fields.[28] However, one must highlight here the extremely

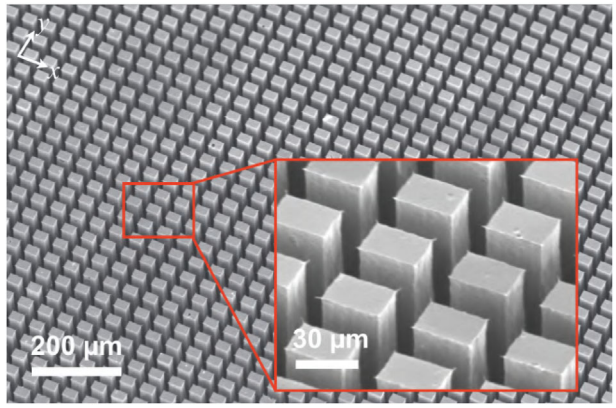


**Figure 32.** SEM image of an experimental realization of high-aspect-ratio structures covering a $mm^2$ wide area obtained by laser processing followed by chemical etching. The pillars individual structures have dimensions of approximately $20 \times 30 \times 500$ $\mu m^3$ with their longer sides along the laser beam propagation direction. Laser wavelength: 1.55 µm; pulse duration: 5 ns. Reproduced with permission.[19] Copyright 2017, Springer Nature.

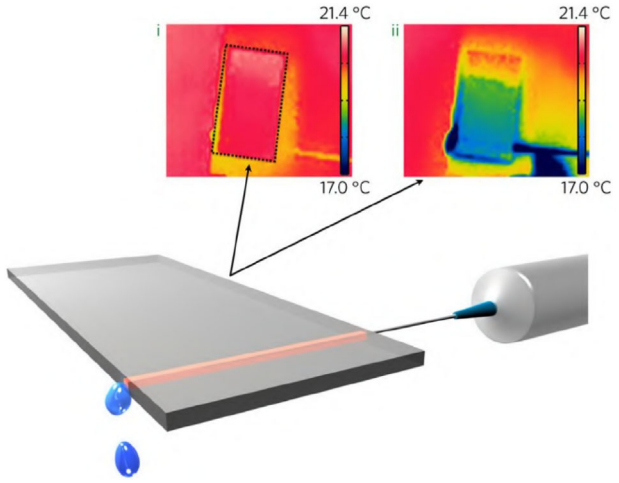


**Figure 33.** Illustration of an 8-mm long microfluidic channel carrying cooling water into a chip. Thermal camera images i) before and ii) after passing the water show that the surface temperature of the chip decreases by 4 °C within a few seconds. Laser wavelength: 1.55 µm; pulse duration: 5 ns. Reproduced with permission.[19] Copyright 2017, Springer Nature.

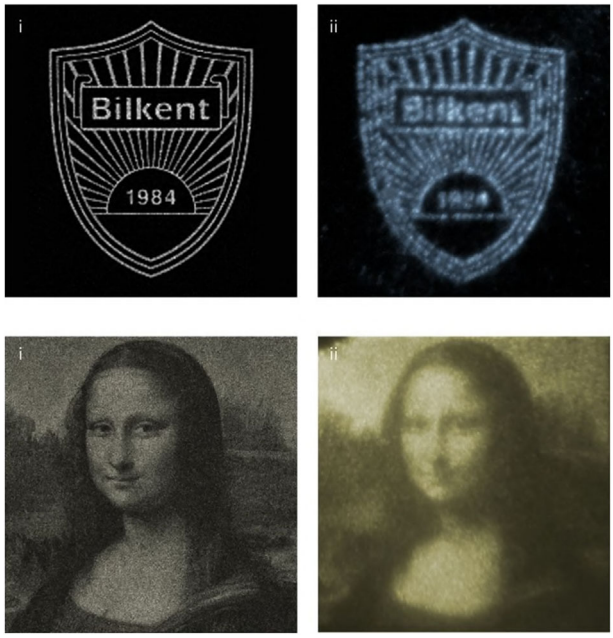


**Figure 34.** i) Simulation of (top) a binary image with high-frequency spatial components and (bottom) a grey-scale image of the Mona Lisa (by Leonardo da Vinci), from a hologram of 600 × 600 10-µm size pixels. ii) Experimental reconstruction of the holograms written in silicon. Laser wavelength: 1.55 µm; Pulse duration: 5 ns. Reproduced with permission.[19] Copyright 2017, Springer Nature.

high etching contrast demonstrated in negative-tone structuring by Tokel et al. for the fabrication of complex structures.

A direct application arising from the possibility to selectively remove material in silicon is microelectronics. Indeed, coupling laser inscription and selective chemical etching can be used to inscribe millimeter-long microfluidic channels in silicon. Such channels constitute an interesting alternative to standard technologies employed for cooling microelectronic devices (e.g., microprocessors), and thus, increasing the clock rates.[193] These laser-written channels enable direct cooling of the target device, as shown in **Figure 33** where a chip is cooled down by a few degrees in a few seconds[19] (see Video S4, Supporting Information in this reference). Therefore this result demonstrates that nanosecond laser direct writing can be applied for preventing microelectronic circuits from overheating.

A last application of negative refractive index changes induced by nanosecond laser pulses is data storage. While laser-writing is a well-established technique for eternal data storage in glasses,[194,195] it had no equivalent in silicon until recently. Tokel et al. demonstrated the possibility to store data by creating 2D Fourier computer-generated holograms for binary and grayscale images designed with an adaptive-additive iterative Fourier transform algorithm (see **Figure 34**).[19] These nanosecond-laserwritten holograms are composed of 600 × 600 pixels with a pixel size of 10 µm, and show to date a comparable quality in terms of image reconstruction to nanophotonic phase arrays[196] and metamaterial phase holograms.[197,198]

Data storage in silicon was also illustrated by the inscription of parallel lines of modified material that can act as a barcode. In that way, Tokel et al. have shown that it was even possible to inscribe several barcodes at various depths inside silicon.[19] The reading of these two barcodes was performed by using optical coherence tomography. Moreover, by annealing the sample in which the structures were inscribed in an oven at high temperatures (1100 °C during 2 h), the barcodes could be erased and rewritten again, highlighting the prospects for erasable and rewritable information storage holography.

### 4.2. Picosecond Inscription

We have shown in Section 3 that modifying silicon with femtosecond laser pulses is extremely challenging. In stark contrast, it is possible to tailor the material properties with nanosecond laser pulses, as shown in Section 4.1. The picosecond regime thus naturally appears as the pivotal time domain where silicon can be modified. In that way, Kämmer et al. have studied the pulse duration dependence of laser-induced damage in the picosecond regime at 1.55-µm wavelength.[199] As shown in **Figure 36**, for a constant pulse energy of 6.6 µJ, the damage probability (defined as the ratio between the number of damage sites and the total number of irradiated sites) increases with the pulse duration, logically bridging the behaviors found in the femtosecond and the nanosecond regime. Noteworthy, this increase in the damage probability with respect to the pulse duration for a constant pulse energy is opposite to the laser-induced damage behavior in dielectrics.[65–67,200] This indicates again that damage initiation in the bulk of silicon is closely correlated with the nonlinear propagation of the laser pulses. One can also note in Figure 36 that the damage probability is close (but not equal) to 100% for a pulse duration of 10 ps, highlighting that this regime is close to the one where repeatable modifications can be achieved in a deterministic way.

In order to reach this regime, Chambonneau et al. have chosen to employ picosecond pulses at 2-µm wavelength for modifying

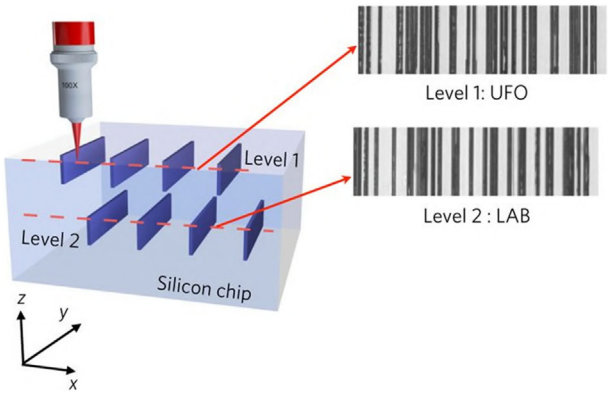


**Figure 35.** Illustration of multilevel information storage and measured images in silicon. The level 1 barcode spells "UFO" and the level 2 barcode spells "LAB". Laser wavelength: 1.55 µm; pulse duration: 5 ns. Reproduced with permission.[19] Copyright 2017, Springer Nature.

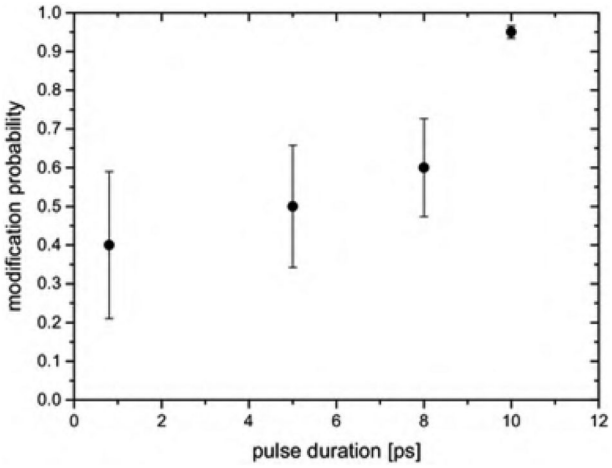


**Figure 36.** Evolution of the damage probability in bulk crystalline silicon as a function of the pulse duration. The irradiations are composed of 15,000 pulses with a pulse energy of 6.6 µJ. Laser wavelength: 1.55 µm. Reproduced with permission.[199] Copyright 2018, Springer Nature.

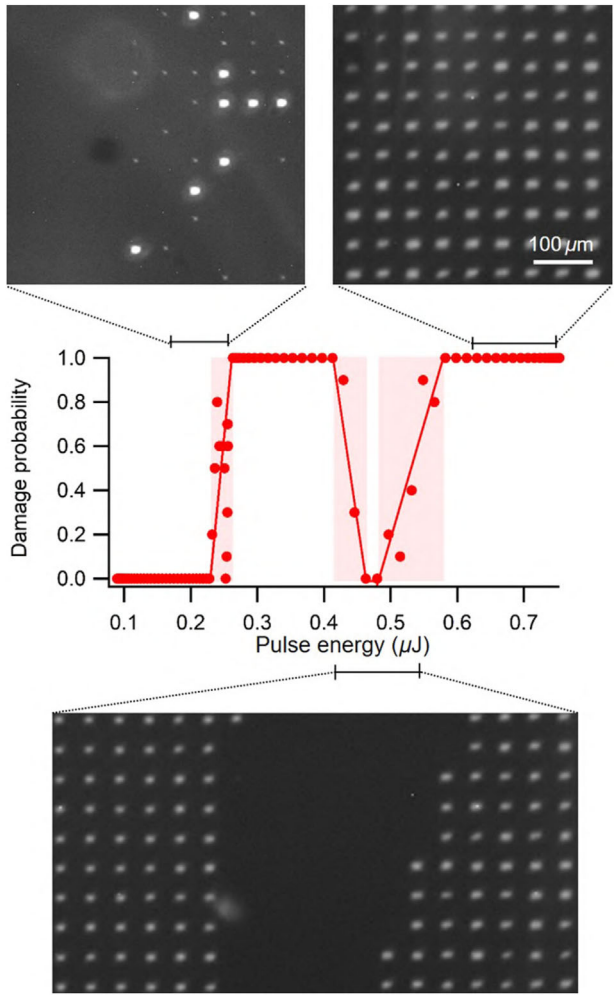


**Figure 37.** Evolution of the damage probability in the bulk of silicon (at a depth of 150 µm) as a function of the pulse energy. The laser beam is focused with an aspherical lens of numerical aperture NA = 0.85. Each probability value is retrieved from the irradiation of 10 fresh sites by 10,000 pulses at 100-kHz repetition rate. The inserted images correspond to dark field microscopy observations of the irradiated sites along the optical axis in the indicated pulse energy ranges. Laser wavelength: 1.97 µm; pulse duration: 2 ps. Reproduced with permission.[31] Copyright 2019, American Physical Society.

bulk silicon in a deterministic and repeatable way.[31] At this wavelength, the nonlinear refractive index of silicon $n_2$ shows a peak value.[47,48,98] According to nonlinear propagation simulations performed by Zavedeev et al. (see Section 3.2, Figure 12), this peak implies a local maximum value of the produced electron density, thus potentially leading to permanent modification.[102] As shown in **Figure 37**, damage probabilities of 100% can be reached with 2-ps pulses at 2-µm wavelength and sub-µJ pulse energies. The striking feature in this figure is the non-monotonic behavior of the damage probability curve. Starting from the highest pulse energies, one should note that the damage probability decreases to 0% at ≈ 450 nJ. The damage probability increases again to 100% and finally drops down to 0% again at 250 nJ, thus defining the damage threshold. By repeating the experiments in various regions of the sample, the authors concluded that this extremely uncommon damage behavior in the 0.4–0.6-µJ pulse energy range was not related to statistical effects.

In the same study (ref. [31]), nonlinear propagation simulations and energy flow analyses revealed that this experimental behavior originates from the competition between the optical Kerr effect and plasma defocusing. The corresponding simulations displayed in **Figure 38** have shown that, during this competition, the mechanism taking over strongly depends on the pulse energy. Hence, the number of energy flow lines near the focus as a function of the input pulse energy exhibits a minimum when plasma defocusing is the dominant mechanism.

Tolstik et al. and Richter et al. confirmed the specificity of reaching the permanent modification regime at 2-µm wavelength with picosecond pulses by comparing the results of nonlinear propagation simulations at wavelengths between 1.55 and 2.35 µm.[201,202] Similar to the nonlinear propagation models presented in Section 3, the calculations rely on the solution of the nonlinear Schrödinger equation (NLSE). For 1-µJ pulses, the domain of high free-carrier density at 1.95- and 2.15-µm

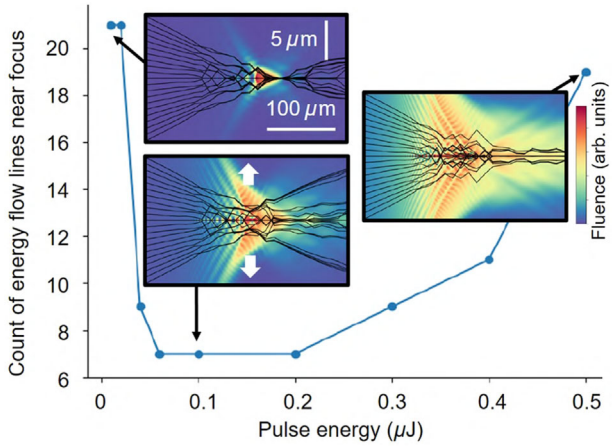


**Figure 38.** Energy flow analysis by nonlinear propagation simulations of focused picosecond pulses. The insets show the fluence distribution and energy flow lines obtained by retrieving the wave vectors from the wavefront of the pulse at each propagation distance for incoming energies of 0.01, 0.1, and 0.5 μJ. The graph gives the number of energy flow lines reaching a zone of 1 μm at the vicinity of the focus as a function of the input pulse energy. Laser wavelength: 1.97 μm; pulse duration: 2 ps. Reproduced with permission.[31] Copyright 2019, American Physical Society.

wavelength is larger than at 1.55- and 2.35-μm wavelength. This result is consistent with ref. [102], and explained by the aforementioned presence of a peak in the nonlinear refractive index of silicon around 2-μm wavelength. The beneficial aspect of near-2-μm wavelengths for modifying silicon was experimentally verified in ref. [202] by using 5-ps duration pulses at 2.09-μm wavelength emitted by a Ho:fiber-seeded Ho:YAG chirped-pulse amplifier.

### 4.3. Pulse Trains

We have introduced the capacity of nanosecond lasers to thermally induce modifications in the bulk of semiconductors (see Section 4.1), the relative harmlessness of femtosecond regime,[13,77] and an interesting potential in the intermediate picosecond regime despite some remaining competitions with the nonlinear response that may affect the writing controllability.[31,199] Nevertheless, there is still a large range of possible optimizations in the time domain to solve this problem and improve the reliability of ultrafast transformation regimes.

To illustrate this aspect, it is important to mention the works by Mori et al.[17] and Shimotsuma et al.[203] in which local modifications in the bulk of semiconductors have been achieved for the first time with femtosecond pulse trains. Employing a Cr:forsterite amplified femtosecond laser system operating at 1.24-μm wavelength with 110-fs pulse duration, the authors first confirmed that it is impossible to induce any structural changes inside silicon with repeated single-pulse irradiations[13,77] despite high-energy pulses (600 μJ) and a large numerical aperture (NA = 0.85) for focusing. However, by repeatedly illuminating silicon with double-pulse trains of ≈ 50-μJ energy, they successfully obtained embedded modifications taking the form of periodic nanostructures. **Figure 39** shows an electron image of the modifications captured after polishing the irradiated samples

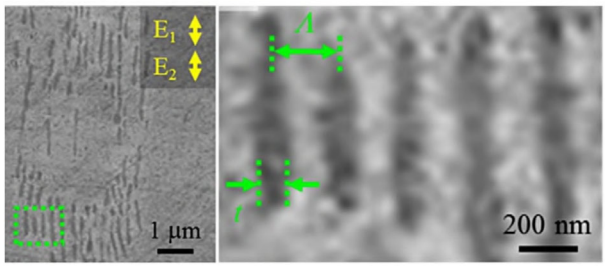


**Figure 39.** Self-organized nanostructures formed inside silicon by illumination with trains of two femtosecond pulses. The images are secondary electron images of polished samples down to the depth of the focus position after laser irradiations with 1,000 double-pulse sequences of 50-μJ total energy. The pulses are separated by ≈ 1 ps and are focused with a numerical aperture NA = 0.85. Laser wavelength: 1.24 μm; pulse duration: 120 fs. Reproduced with permission.[17] Copyright 2015, Wiley–VCH.

down to the level necessary to have the modifications exposed to the surface.

The motivation of applying double-pulses to deposit higher energy densities was directly inspired by a method applied in dielectrics to separate and control individually plasma ignition (first pulse) and energy deposition by free-carrier heating and avalanche ionization (second pulse).[205,206] Accordingly, the reported modifications were obtained for pulse separations from 1 ps to 1 ns, which is the timescale for which there is no significant decay of free-carrier density in silicon.[77,78] The authors found that an appropriate energy ratio between the two pulses is required so that the second pulse can interact with a plasma of adequate density to avoid that most of the energy gets reflected or defocused. However, double-pulses (of 120 fs each) with equally-divided pulse energy were typically employed that raises questions on the strongly different results obtained in comparison to other experiments performed with twice longer pulses (250 fs) in which material modification was impossible.[77]

Interestingly, Figure 39 shows that the modifications consist of strained-silicon regions induced with a period of $\lambda/2n = 180$ nm similar to those found in fused silica[207,208] and other dielectrics. However, a major difference is the orientation of the structures that are aligned parallel to the laser polarization while planar nanostructures in dielectrics are orthogonal to the laser polarization. Because the physics behind the formation of these nanostructures remains today an important matter of debate, it is interesting to find different situations in the bulk leading to the two orientations. So far, this was only reported on surfaces for different regimes of the so-called laser-induced periodic surface structure (LIPSS) found in a wide variety of materials.

By repeating the experiments in various semiconductors, Shimotsuma et al. found that the generation of nanogratings was only possible for silicon and gallium phosphide (GaP) which are indirect band-gap materials.[203] In the case of gallium arsenide (GaAs), gallium nitride (GaN), and zinc oxide (ZnO) which are direct band-gap materials, no nanogratings could be observed. The origin of the formation is far from being elucidated, but this dependency on the band gap led the authors to suggest an interpretation based on an electrostrictive force through the plasma–phonon interaction. On the technological side, material analyses show that the strained-silicon nanostrutures exhibit electrical and

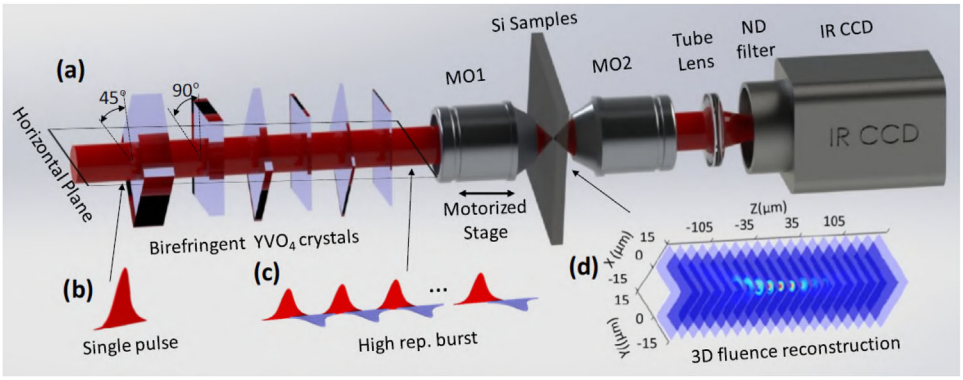


**Figure 40.** Experimental arrangement for generation of THz-repetition rate trains of pulses and diagnostic of the delivered fluence in silicon a) experimental setup, b,c) temporal pulse shapes and associated polarization orientations. d) 3D laser fluence reconstruction by an imaging technique resembling the *z*-scan. Reproduced with permission.[204] Copyright 2020, AAAS.

thermal conductivity that may offer possibilities for the fabrication of thermoelectric devices.[203]

Capitalizing on this first double-pulse report and inspired by recent advances in surface machining using GHz burst regimes, a recent study has revisited the potential of trains of two or more pulses[204] to meet the challenge of ultrafast laser writing inside silicon. In this work, bursts with repetition rates up to 5.6 THz and number of pulses up to 64 are generated by an engineered stack of birefringent crystals as shown in **Figure 40**. This allows splitting any incoming ultrashort pulse in a train of delayed replicas with inter-pulse separations controlled by the thicknesses of crystals. With the typical picosecond inter-pulse delay in the trains, an improvement of energy deposition is systematically observed in delivered and absorbed fluence diagnostics. This is due to pulse-to-pulse accumulation of carriers and heat before the energy diffusion processes occurring at typical nanosecond timescales come into play.[78] Interestingly, the study concludes on a number of pulses in the train that should not be exceeded (in the range 8 to 16 for 180-fs pulses focused with a numerical aperture of NA = 0.85) for appropriate excitation build-up and limited retro-reaction delocalizing the beam creating the excitation. However a major difference with ref. [203] is that none of the pulse sequences with individual pulse duration of ≈180 fs was successful in achieving permanent modifications inside silicon. The difference has been recently attributed to the sensitivity to the temporal contrast of the pulses that are not identical due to different laser technologies used in these two studies.[209]

The benefits of the burst mode have been however exploited for improved performance of 3D laser direct writing inside silicon with trains of picosecond pulses. This can be directly seen in **Figure 41** showing impacts inside silicon obtained for identical energies but shared in different sequences of 5 ps pulses (single-pulse, double-pulse, or four-pulse sequence). Single-pulse irradiations are systematically below threshold (Figure 41a) while all conditions with trains of 4 pulses at energies exceeding 1.1 μJ lead to highly repeatable modifications (Figure 41c). Interestingly, the sites irradiated with double-pulse trains exhibit smaller features than the 4-pulse trains and low probability for modification occurrence at the maximum tested energy (Figure 41c). This is likely due to light delocalization near the critical power for self-focusing.[31] This is interesting for technological considerations, because a simple insertion of crystals in the beam path which split the applied pulses, can represent a practical solution to make a step up in the deposited energy (that is not accessible by simply increasing the input pulse energy due to intensity clamping[18]) and then stabilize the picosecond laser writing performances for applications.

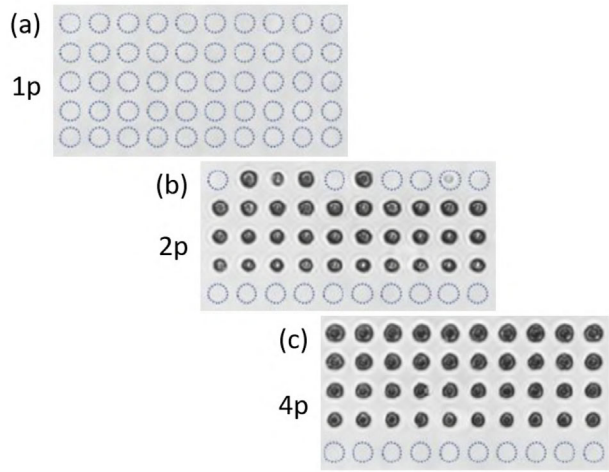


**Figure 41.** Modification attempts with 5-ps a) single-pulse, b) double-pulse, and c) four-pulse irradiations. From top to bottom, the irradiation are repeated ten times with identical conditions on each row for different energies: 2.1, 1.9, 1.5, 1.1, 0.6 μJ. The dotted circles represent irradiated sites without apparent modification. One observes that, by energy sharing between pulses, the situation changes from no modification to highly reproducible modifications. Laser wavelength: 1.55 μm. Adapted with permission.[204] Copyright 2020, AAAS.

### 4.4. Surface-Seeded Bulk Modifications

In the previous sections, laser–silicon interaction was investigated solely in the bulk. Nevertheless, one could wonder how the exit surface of silicon behaves under laser irradiation. In dielectrics, the exit surface exhibits a lower damage threshold than the entrance one. This mainly originates from the asymmetry of the surface plasma formed during the interaction.[210,211] In

the case of entrance surface irradiation, plasma shielding occurs, and prevents the material from modification for insufficient laser fluences. In stark contrast, for a plasma formed on the exit surface, there is no shielding effect and the hot plasma grows toward the material. In the present section, we first report some studies on damage formation on the exit surface of silicon showing a radically different behavior compared to dielectrics. Then, several works on the exit-surface-seeded inscription of waveguides in bulk silicon are presented.

#### 4.4.1. Backside Processing of Silicon

As detailed in Section 3, the propagation of laser pulses with a duration < 100 fs in silicon is highly nonlinear.[15,18] Consequently, the energy deposition is strongly delocalized, and no permanent modification can be produced in the bulk of the material through a plane interface. Interestingly, the repeatable experimental measurements of the nonlinear propagation in refs. [15, 18] were possible due to the fact that no damage could be produced on the exit surface of the material—the energy depletion in the bulk being too important. This holds even when the maximum fluence is located at the exit surface of the double-side polished sample.

Using 100-fs duration pulses at 1.3-μm wavelength, Lei et al. showed that repeatable modifications could be produced on the gold-coated exit-surface of a silicon wafer.[212] The same nonlinear propagation imaging procedure as in refs. [15, 18] was applied for uncoated silicon, revealing again the absence of permanent modifications on the exit surface of the sample. However, as shown in **Figure 42**, repeatable damage is produced for a gold-coated exit surface. This can be explained by the fact that the free electrons of the metallic film are able to absorb the laser flux linearly by inverse bremsstrahlung, which is particularly efficient for infrared wavelengths. Concerning the damage tests on gold-coated entrance surface of silicon (Figure 42a), the damage pattern looks symmetric with respect to the center line, with a minimum size for a geometrical focus located on the surface. In stark contrast, damage tests on the gold-coated exit surface of silicon (Figure 42b) exhibit an asymmetry. In particular, the crater size is larger when the prefocal region is located on the surface. This is clear evidence of the delocalization of the light in silicon, and confirmed at the different tested energies. The through-silicon ablation technique for selective removal of gold films was also observed recently by Astrauskas et al. at 2.09-μm wavelength.[213] By employing a single chirped volume Bragg grating for stretching and compressing the pulses, the authors performed backside ablation of gold on a silicon substrate at various pulse durations ranging from 400 fs to 6 ns. Their conclusion was that 3.2-ps pulses lead to the optimal ablation results since this pulse duration reduces the nonlinearities observed with sub-picosecond pulses on the one hand, and thermal effects inherent to > 100-ps pulses on the other hand.

Besides the applications in selective material removal, the enhanced absorption on the exit surface of silicon when interfaced with a metal can be advantageously used for additive manufacturing. This was recently illustrated by Chambonneau et al. who demonstrated semiconductor–metal laser welding with 9.8-ps pulses at 1.55-μm wavelength.[214,215] As described in Section 3, laser filaments are formed during the propagation in silicon, and

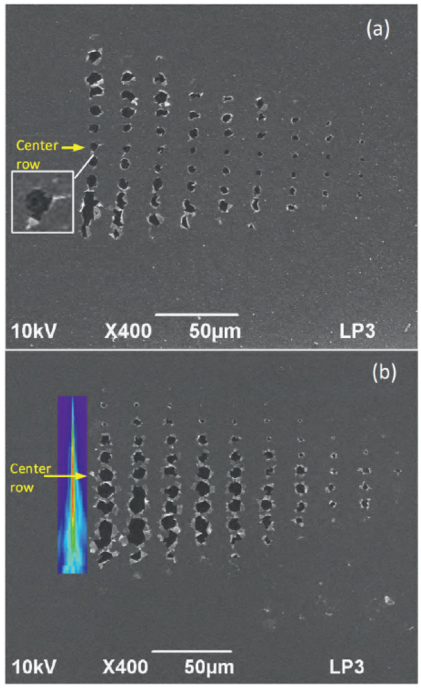


**Figure 42.** Scanning electron microscopy images showing ablation of a gold thin film on silicon wafer from a) the entrance surface and b) the exit surface. The pulse energy ranges from ≈ 150 to ≈ 15 nJ (from left to right). The center line corresponds to the maximum intensity, and the other lines correspond to relative displacements of 5 μm on the focusing objective lens. Laser wavelength: 1.3 μm; pulse duration: 100 fs. Reproduced with permission.[212] Copyright 2016, Elsevier.

the nonlinear focal shift leads to a dramatic depletion of the energy deposition at the exit surface of the material at levels insufficient for laser welding applications. In order to remedy this problem, the authors first determined the nonlinear focal shift $\Delta z$ in silicon only, thanks to nonlinear propagation imaging. The evolution of $\Delta z$ as a function of the input pulse energy $E_{in}$ is well described by a modified Marburger formula[214–216] accounting for the nonlinear absorption losses. Then, by employing the arrangement in **Figure 43**a, silicon–copper laser welding was endeavored with and without precompensation of the nonlinear focal shift $\Delta z$. This precompensation consists of correcting the position of the focusing objective lens by the predetermined $\Delta z$ value. The welding quality in terms of shear joining strength was evaluated *ex-situ* by separating the two samples. As shown in Figure 43b, mediocre shear joining strengths (< 30 kPa) which are incompatible with applications have been measured for a geometrical focus simply positioned at the interface (i.e., no $\Delta z$ precompensation). In stark contrast, precompensating the nonlinear focal shift $\Delta z$ leads to significant shear joining strength values. By employing higher input pulse energy $E_{in}$ values than in Figure 43b (up to 1 μJ), remarkable shear joining strengths were measured in this study (up to 2.2 MPa). This shows the considerable advantage to account for nonlinear propagation effects for semiconductor–metal ultrafast laser welding as illustrated in Figure 43c.

The difficulties to modify the exit surface of silicon with the aforementioned ≤ 100-fs duration pulses also exist with sub-picosecond pulses. This was demonstrated by Ito et al.,[217] and,

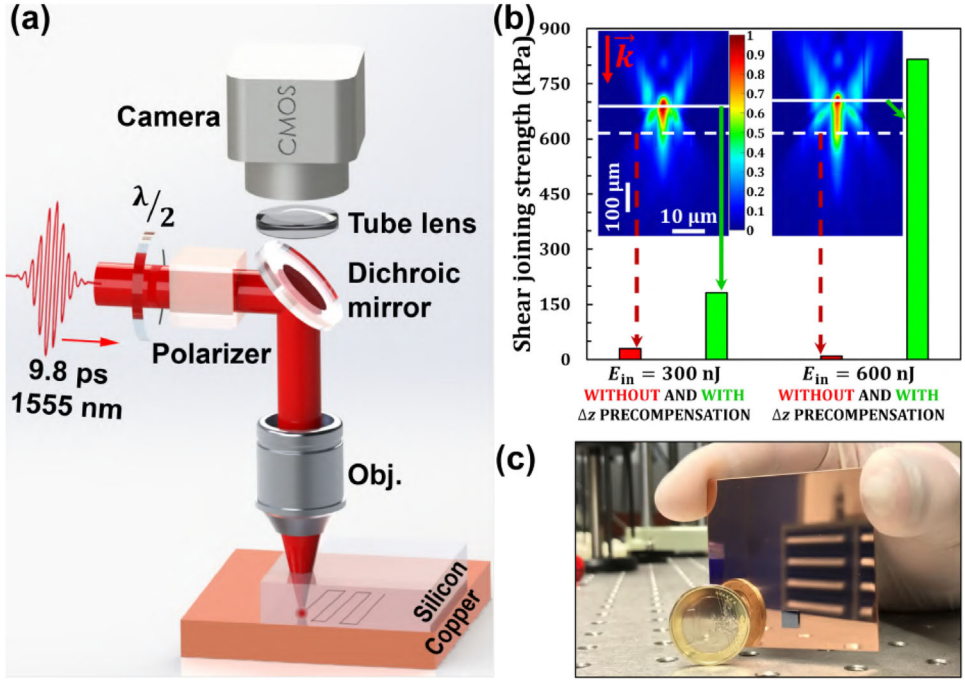


**Figure 43.** a) Schematic of the arrangement employed for semiconductor–metal ultrafast laser welding. b) Laser-induced shear joining strength between silicon and copper for an input pulse energy $E_{in}$ = 300 and 600 nJ without (in red) and with (in green) precompensation of the nonlinear focal shift Δz. The insets are the corresponding fluence distributions obtained with nonlinear propagation imaging. The vector $\vec{k}$ shows the direction of the laser propagation. The solid and dashed white lines indicate the position of the interface between the two samples in each configuration. c) Photograph of an ultrafast-laser-welded 5 × 5-mm$^2$ size crystalline silicon sample on copper. Laser wavelength: 1.55 µm; pulse duration: 9.8 ps. Reproduced with permission.[214] Copyright 2021, Wiley–VCH.

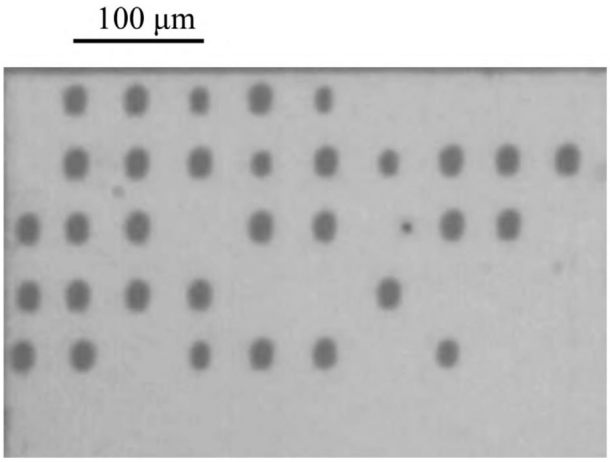


**Figure 44.** Optical micrograph of the exit surface of silicon after 100,000 pulses on the same site. The laser conditions are kept the same for all sites. Laser wavelength: 1.55 µm; pulse duration: 900 fs. Reproduced with permission.[218] Copyright 2020, Laser Institute of America.

more recently, by Luong et al.[218] In these studies, 900-fs pulses have been employed for studying backside ablation of silicon. As shown in **Figure 44**, it is possible to produce modifications on the exit surface of the material. Nevertheless, the appearance of such damage sites is stochastic, which likely originates from the presence of precursor defects locally enhancing the laser electric field and/or the absorption of the laser flux by the material.[219] Additionally, one can note the non-repeatable character of the damage morphology. All these results indicate the difficulty to inscribe continuous lines on the exit surface of silicon with sub-picosecond laser pulses.

As discussed in Section 4.1, nanosecond pulses are a powerful alternative for modifying silicon. Moreover, at 2-µm wavelength, silicon exhibits a nonlinear refractive index peak (see Section 3.2, Figure 12),[47,48,98] which is favorable for producing relatively high electron density[102] and potential modifications.[31,202] By combining these two advantages, Gehlich et al.,[220] and Mingareev et al.[221] have employed nanosecond laser pulses at 2-µm wavelength for writing continuous lines at the exit surface of silicon. As shown in **Figure 45**, 7- and 100-ns duration pulses are both suitable for this achievement. Nevertheless, the line morphology is different in each case. The line inscribed with 7-ns duration pulses shows a fractured morphology, while the one inscribed with 100-ns duration pulses exhibits a periodic resolidified pattern (1 µm period) likely arising from overlapping single-pulse modifications. In this long pulse duration regime, a larger contribution of thermal phenomena to the modification process was pointed out by the authors. They also measured the damage threshold of the entrance and the exit surface with 7-ns duration pulses. The striking result is that this threshold is way higher for the exit surface ($\lesssim$ 17.2 J cm$^{-2}$) compared to the entrance surface ($\lesssim$ 2.86 J cm$^{-2}$). Given the Fresnel reflection coefficient of an air–silicon interface ($\approx$ 30%), this significant difference cannot only be explained by an energy decrease due to

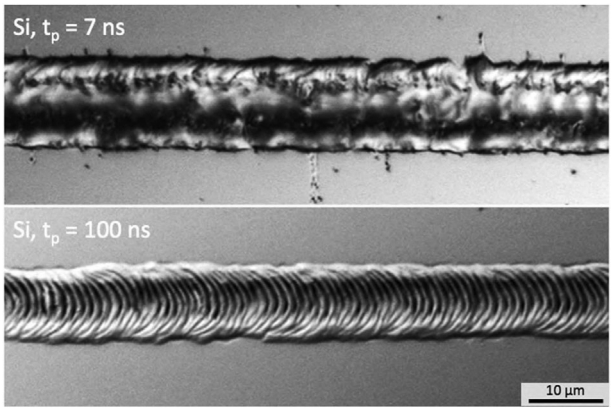


**Figure 45.** Optical micrographs of modifications obtained on the exit surface of silicon for 294-µJ pulse energy and the indicated pulse durations. Laser wavelength: 1.99 µm. Reproduced with permission.[221] Copyright 2016, Springer Nature.

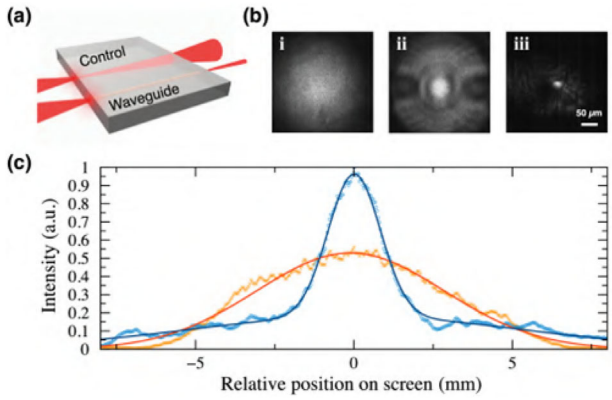


**Figure 46.** a) Schematic illustration of direct coupling of continuous light at 1.5-µm wavelength into the waveguide in bulk silicon and the corresponding control experiment. b) (i) far-field image of the light after passing through silicon without waveguide. (ii) far-field image of the light exiting from the end facet of the waveguide. (iii) near-field image of the light exiting from the end facet of a waveguide. c) Intensity profiles along the vertical axes of the far-field images shown in parts (i), (ii), and the corresponding numerical fits. The blue (solid) curve is a double Gaussian fit to the intensity profile data (blue circles) obtained from the waveguide exit. The red curve is a Gaussian fit to the data (orange crosses) from the control measurement. Laser wavelength: 1.5 µm; pulse duration: 350 fs. Reproduced with permission.[20] Copyright 2017, The Optical Society.

reflection. Therefore, this result highlights the importance of the nonlinear propagation phenomena even with nanosecond pulses at 2-µm wavelength. Noteworthy, as previously discussed, this behavior is totally opposite to the one observed in glasses, where the entrance surface usually exhibits a higher laser-induced damage threshold than the exit surface.[210,211,222]

#### *4.4.2. Exit-Surface-Seeded Waveguide Inscription*

Once the exit surface of silicon is damaged (see Section 4.4.1), the absorption is enhanced in the vicinity of the modifications. Therefore, for a constant position of the focus, the laser-induced modification may grow on a pulse-to-pulse basis. This damage growth phenomenon has been intensively studied in glasses as it represents an important limitation for the operation of inertial confinement fusion laser facilities.[223,224] While the exact physical mechanisms explaining this phenomenon are still to date under debate due to the complex modeling of this multi-pulse phenomenon, one can cite the creation of local defects inducing states located in the band gap, and electric field enhancement due to the change in the surface topography.

By constantly moving the focus upstream the laser, some research groups have turned this undesirable effect into an advantage for the inscription of waveguides in bulk silicon. These exit-surface-seeded waveguides rely on the fact that the modification induced by one pulse acts as a precursor for the following one. A first demonstration of such waveguides was provided by Pavlov et al. where 350-fs duration laser pulses emitted at 1.5-µm wavelength and 250-kHz repetition rate were employed.[20] In these experiments, the focus of an aspherical lens (numerical aperture NA = 0.5) was constantly moved from the exit surface to the entrance surface at a constant speed in the range of 0.03–0.1 mm $s^{-1}$. As illustrated in **Figure 46**, the injection of continuous light in the 20-µm diameter and 5.5-mm long structures revealed their waveguiding properties. The input and output ports of the waveguides are then revealed by polishing the surfaces. Quantitative shadowgraphy and calculations of the numerical aperture of the waveguide (NA = 0.05) were applied for estimating a refractive index change $\Delta n = 3.5 \times 10^{-4}$ and $6.0 \times 10^{-4}$, respectively, assuming a step-index profile. The written structures constitute the first functional optical elements created deep inside silicon without altering the wafer surface using femtosecond laser pulses.

By using a comparable technique, Matthäus et al. achieved 800-µm long waveguides in silicon.[25] In this study, a rough polishing process was applied on the exit surface of the sample for generating the necessary seeds for the subsequent waveguide inscription. The employed 800-fs duration laser pulses at 1.55-µm wavelength were focused with an objective lens of numerical aperture NA = 0.4. A parameter study revealed the existence of an optimal pulse energy of 110 nJ for the improved waveguiding properties. For this pulse energy, the waveguides exhibit a refractive index change $\Delta n = 2.5 \times 10^{-3}$ as confirmed by the comparison between simulations relying on the inverse Helmholtz equation and near-field images. The demonstration of guided light was all the more supported by the inscription of the Y-splitter depicted in **Figure 47**, similar to ref. [173]. The injection of a Gaussian-shaped beam of continuous light at 1.55-µm wavelength (Figure 47a) gives rise to two distinct spots at the output of the structure (Figure 47b) with propagation losses on the order of 4.5 dB $mm^{-1}$, as illustrated by the scattered light image in Figure 47c.

In refs. [20] and [25], the possibility to modify silicon was attributed to potential cumulative effects at relatively high repetition rates (250 kHz in ref. [20] and 30–400 kHz in ref. [25]). Below, we examine this assumption with simple theoretical considerations for evaluating the potential existence of cumulative effects. First, one could expect heat accumulation effects similar to those existing at repetition rates ≥ 100 kHz in glasses.[38] However, one should keep in mind the high thermal diffusivity of silicon ($D = 8.8 \times 10^{-5}$ $m^2$ $s^{-1}$,[50] as reported in Section 2, Table 1) which is two orders of magnitude larger than the one of

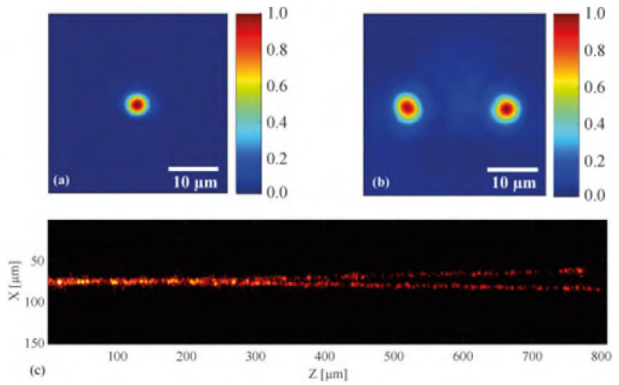


**Figure 47.** a) Normalized near-field distribution before the injection of continuous light at the entrance of a Y-splitter. b) Normalized near-field distribution at the output of the Y-splitter. c) Image of the light scattered along the Y-splitter (logarithmic scale). Laser wavelength: 1.55 μm; pulse duration: 800 fs. Reproduced with permission.[25] Copyright 2018, The Optical Society.

glasses. The distance $L$ where the heat has diffused away from the source reads

$$L = \sqrt{\frac{2D}{\Omega}} = \sqrt{2D\tau} \tag{6}$$

where $\Omega$ is the repetition rate of the laser source, and $\tau = 1/\Omega$ is the duration between two consecutive pulses. Considering the maximum repetition rates in refs. [20] and [25], the distance $L$ is 26.5 and 21 μm, respectively. These values are about one order of magnitude higher than the beam radius (on the order of 1 μm), given the high numerical apertures employed in these studies (NA = 0.5 in ref. [20] and NA = 0.4 in ref. [25]). Therefore, one can conclude that, in these works, the modifications are unlikely to originate from heat accumulation effects. This conclusion was also drawn experimentally in ref. [25] where the authors observed no significant difference in the results by changing the repetition rate in the 30–400 kHz range. In fact, Equation (6) implies that the condition $L \leq 1$ μm is satisfied only for $\Omega \geq 176$ MHz, in accordance with the results of Wang et al.[204] presented in Section 4.3.

One could also consider free-carrier accumulation effects to occur in refs. [20] and [25]. Recent time-resolved observations in bulk silicon under femtosecond laser irradiation compared to an electron diffusion model have shown an ambipolar diffusion coefficient of 2.5 $cm^2\ s^{-1}$.[78] Moreover, the lifetime of the laser-produced plasma is in the 1–10 ns range.[77,78] Once again, these values imply that repetition rates ≥ 10 MHz have to be employed for generating free-carrier accumulation effects in bulk silicon. Therefore, one can reasonably attribute the waveguide inscription in refs. [20] and [25] to exit-surface seeding. While, in ref. [20], it was also possible to write the structures away from the exit-surface, the repeatability was somewhat higher when the structures were initiated closer to the surface. This tends to indicate an absence of fundamental limitations for achieving in-bulk modification in these experiments, but imposes conditions for exceeding the damage threshold without the assistance of a seeding imperfection during the writing process. As discussed in Section 4.3, such a situation could eventually be attributed to the some imperfections in the temporal profile of the laser pulses.[209]

Following the same exit-surface-seeded waveguide inscription procedure as the one detailed in ref. [25], Alberucci et al. have recently carried out in-depth analyses of the waveguide profiles, that is, its refractive index distribution in the $xy$ plane perpendicular to the optical axis $z$.[225] This work relies on a comparison between experiments consisting of transversely-shifted injection of continuous light in the waveguides in the $xy$ plane, and calculations of the overlap integral together with the beam propagation in each situation. In this case, the waveguides showed losses of

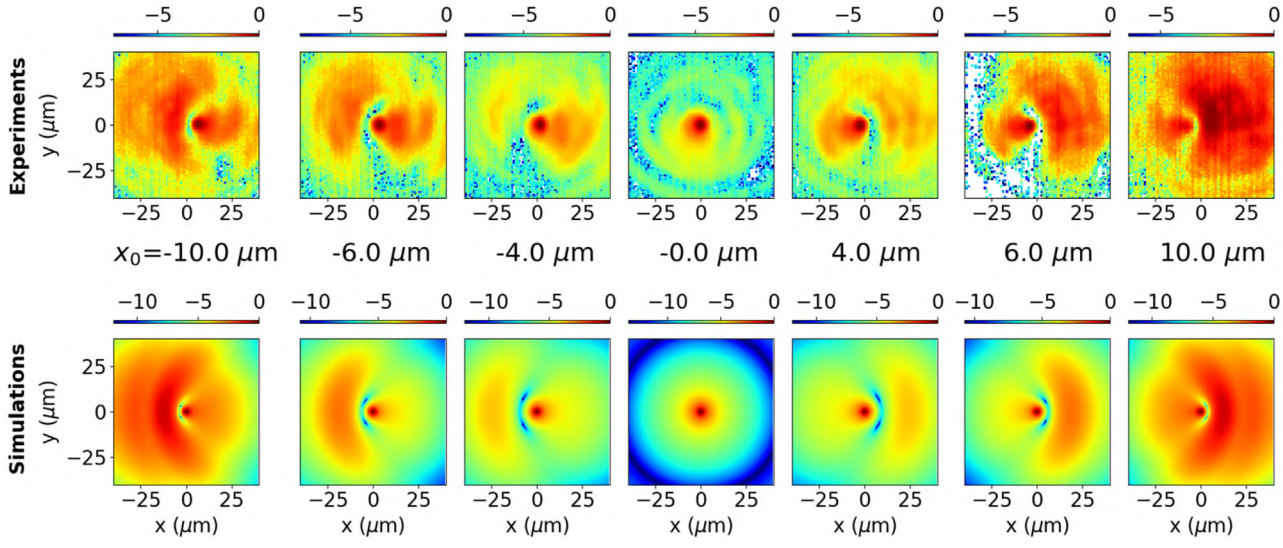


**Figure 48.** (Top) Experimental measurements of the normalized intensity distribution at the output of a waveguide, for the indicated lateral shifts $x_0$. (Bottom) Corresponding simulations with a beam propagation method, assuming a waveguide profile of the waveguide according to Equation (7) with $\Delta = 4 \times 10^{-3}$. The results are in logarithmic scale and the white points correspond to negative data. Laser wavelength: 1.55 μm; pulse duration: 860 fs. Reproduced with permission.[225] Copyright 2020, American Physical Society.

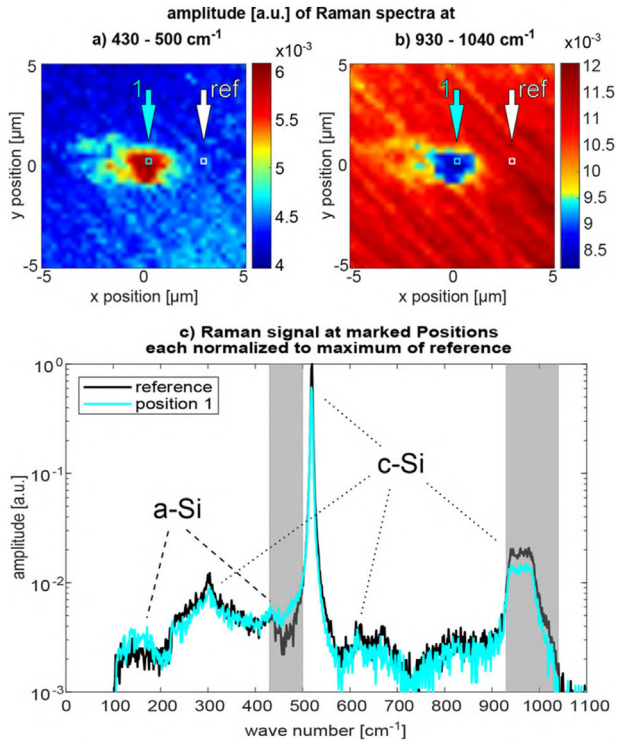


**Figure 49.** Raman spectroscopy signal in the vicinity of a waveguide in silicon in the spectral range of a) 430–500 $cm^{-1}$ and b) 930–1,040 $cm^{-1}$. The arrows in a) and b) mark the position of the full Raman spectra in c). Laser wavelength: 1.55 µm; pulse duration: 800 fs. Reproduced with permission.[23] Copyright 2019, Wiley–VCH.

8.7 dB $cm^{-1}$. In the simulations, the waveguides are assumed to be W-shaped, that is, proportional to the Laplacian of a Gaussian:

$$\Delta n = \Delta\left(1 - \frac{2r^2}{w_{\text{guide}}^2}\right)\exp\left(-\frac{2r^2}{w_{\text{guide}}^2}\right) \quad (7)$$

where $\Delta n$ is the refractive index change, $\Delta$ is the maximum refractive index change, $r$ is the radial distance with respect to the center of the waveguide, and $w_{\text{guide}}$ is the radius corresponding to the transverse extension of the waveguide (measured under infrared transmission microscopy). As shown in **Figure 48**, a very good qualitative agreement is found between the experimental measurements and the theoretical calculations. Moreover, additional calculations assuming a bell-shaped (e.g., Gaussian-shaped) waveguide failed to reproduce the experimental data in Figure 48. Therefore, the waveguides fabricated by exit-surface seeded inscription are W-shaped with a maximum refractive index change of about $\Delta = 4 \times 10^{-3}$. The profile given by Equation (7) is analogous to the one of nanosecond-laser written waveguides observed with phase microscopy, consistent with the law of conservation of mass: if the material is densified somewhere, it has to be rarefied elsewhere.

Finally, from the material science point of view, Kämmer et al. focused their attention on the origin of waveguiding by the inscribed structures based on Raman spectroscopy analyses.[23] As illustrated in **Figure 49**, the waveguide region is unambiguously exhibited with this technique in the spectral ranges of 430–500 $cm^{-1}$ (Figure 49a) and 930–1040 $cm^{-1}$ (Figure 49b) associated with amorphous and crystalline features, respectively.[176,177] The amorphous features increase in the first range while the crystalline features decrease in the second one. This was interpreted by a disturbed crystal structure of the material, potentially induced by defects and dislocations. In this scenario, the refractive index increase of the waveguides could thus be related to local strain fields provoked by the laser-silicon interaction.

## 5. Summary and Outlook

To summarize, while femtosecond laser direct writing is a proven technique in dielectrics, transposing it to silicon is a considerable challenge. This radically different behavior can be attributed to the extremely high nonlinear coefficients of silicon, implying filament formation together with prefocal absorption. As a consequence the energy deposition in the bulk of silicon is strongly depleted, giving rise to underdense plasma formation. While different techniques for producing permanent modifications in silicon with femtosecond laser pulses have been proposed, these are too restrictive for applications. Various solutions have been found to date for circumventing these limitations and functionalize silicon. The first one is to employ longer pulses (in the nanosecond and picosecond regime)—and, thus, operate in different interaction regimes, including the complex self-organization based fabrication. These regimes opened a broad range of applications including wafer dicing, surface texturing, microfluidics, data storage as well as the inscription of functional optical elements (waveguides, holograms, Fresnel-zone-plate lens, gratings).[19,24-28,31,144-147,181,182] The second range of solutions relies on seeded control strategies. Depending on configurations, the seed for modifications can be prepared by locally creating a transient state (i.e., plasma) with an engineered prepulse[209] or train of pulses[204] so that the out-of-equilibrium conditions can be exploited to enhance the absorption of a synchronized processing pulse. Another way to functionalize silicon is to rely on non-transient precursor defects for the bulk inscription process. Such conditions can be found or created by preprocessing at a surface. Using this approach, longitudinal inscription of waveguides has been demonstrated by inducing a seed on the exit surface.[20,23,25,225] This offers a unique possibility for simple writing of optical functional devices in silicon. Based on recent efforts concentrating on silicon and parallel advances in ultrafast laser technologies, its seems natural to expect at short term the deployment of laser 3D writing to even narrower band-gap materials and other important semiconductors such as zinc selenide,[226] zinc sulfide,[227] and gallium phosphide.[228] The rapid development of innovative mid-infrared laser sources should also stimulate researchers to evaluate the potential benefits of selecting wavelengths in high-order (i.e., > 3) multi-photon absorption regimes. In the experimental point of view, picosecond pulses are an excellent compromise for modifying bulk silicon. However, theoretical efforts are still required for the development of a multiscale model accounting for both the nonlinear propagation effects in silicon as well as the response of the material. Ultimately, as a long-term application, the combination of multiple low-loss laser-written functions could allow envisioning the contactless inscription of all-integrated quantum circuits inside silicon.

## Acknowledgements

The authors gratefully acknowledge Ghaith Makey for his help in the production of the graphical abstract. This research has been supported by the Bundesministerium für Bildung und Forschung (BMBF) through the NUCLEUS project (grant No. 03IHS107A), the European Research Council (ERC) through the EXSEED (grant No. 724480), the NLL (grant No. 617521), and the SUPERSONIC (grant No. 966846) projects, the TÜBİTAK – The Scientific and Technological Research Council of Turkey with project No. 20AG024, 20AG001 and 219M274, as well as the TUBA-GEBIP award, and the National Priorities Research Program (grant No. NPRP11S-1128-170042) from the Qatar National Research Fund (member of The Qatar Foundation).

Open access funding enabled and organized by Projekt DEAL.

## Conflict of Interest

The authors declare no conflict of interest.

## Keywords

infrared, processing, nonlinear propagation, silicon, laser–matter interaction, laser direct writing

Received: March 12, 2021
Revised: June 30, 2021
Published online:

[1] F. Arute, K. Arya, R. Babbush, D. Bacon, J. C. Bardin, R. Barends, R. Biswas, S. Boixo, F. G. S. L. Brandao, D. A. Buell, B. Burkett, Y. Chen, Z. Chen, B. Chiaro, R. Collins, W. Courtney, A. Dunsworth, E. Farhi, B. Foxen, A. Fowler, C. Gidney, M. Giustina, R. Graff, K. Guerin, S. Habegger, M. P. Harrigan, M. J. Hartmann, A. Ho, M. Hoffmann, T. Huang, et al., *Nature* **2019**, *574*, 505.
[2] M. Lipson, *J. Lightwave Technol.* **2005**, *23*, 4222.
[3] M. A. Foster, A. C. Turner, J. E. Sharping, B. S. Schmidt, M. Lipson, A. L. Gaeta, *Nature* **2006**, *441*, 960.
[4] M. A. Foster, R. Salem, D. F. Geraghty, A. C. Turner-Foster, M. Lipson, A. L. Gaeta, *Nature* **2008**, *456*, 81.
[5] K. M. Davis, K. Miura, N. Sugimoto, K. Hirao, *Opt. Lett.* **1996**, *21*, 1729.
[6] K. Miura, H. Inouye, J. Qiu, T. Mitsuyu, K. Hirao, *Nucl. Instrum. Methods Phys. Res., Sect. B* **1998**, *141*, 726.
[7] K. Miura, J. Qiu, H. Inouye, T. Mitsuyu, K. Hirao, *Appl. Phys. Lett.* **1997**, *71*, 3329.
[8] R. Soref, *Nat. Photonics* **2010**, *4*, 495.
[9] M. Hochberg, T. Baehr-Jones, *Nat. Photonics* **2010**, *4*, 492.
[10] S. Koehl, A. Liu, M. Paniccia, *Opt. Photonics News* **2011**, *22*, 24.
[11] A. H. Nejadmalayeri, P. R. Herman, J. Burghoff, M. Will, S. Nolte, A. Tünnermann, *Opt. Lett.* **2005**, *30*, 964.
[12] T. H. Crawford, J. Yamanaka, G. A. Botton, H. K. Haugen, *J. Appl. Phys.* **2008**, *103*, 053104.
[13] A. Mouskeftaras, A. V. Rode, R. Clady, M. Sentis, O. Utéza, D. Grojo, *Appl. Phys. Lett.* **2014**, *105*, 191103.
[14] E. V. Zavedeev, V. V. Kononenko, V. M. Gololobov, V. I. Konov, *Laser Phys. Lett.* **2014**, *11*, 036002.
[15] V. Y. Fedorov, M. Chanal, D. Grojo, S. Tzortzakis, *Phys. Rev. Lett.* **2016**, *117*, 043902.
[16] P. C. Verburg, G. R. B. E. Römer, A. J. Huis in 't Veld, *Opt. Express* **2014**, *22*, 21958.
[17] M. Mori, Y. Shimotsuma, T. Sei, M. Sakakura, K. Miura, H. Udono, *Phys. Status Solidi A* **2015**, *212*, 715.
[18] M. Chanal, V. Y. Fedorov, M. Chambonneau, R. Clady, S. Tzortzakis, D. Grojo, *Nat. Commun.* **2017**, *8*, 773.
[19] O. Tokel, A. Turnalı, G. Makey, P. Elahi, T. Çolakoğlu, E. Ergeçen, Ö. Yavuz, R. Hübner, M. Zolfaghari Borra, I. Pavlov, A. Bek, R. Turan, D. K. Kesim, S. Tozburun, S. Ilday, F. Ö. Ilday, *Nat. Photonics* **2017**, *11*, 639.
[20] I. Pavlov, O. Tokel, S. Pavlova, V. Kadan, G. Makey, A. Turnali, Ö. Yavuz, F. Ö. Ilday, *Opt. Lett.* **2017**, *42*, 3028.
[21] P. C. Verburg, L. A. Smillie, G. R. B. E. Römer, B. Haberl, J. E. Bradby, J. S. Williams, A. J. Huis in 't Veld, *Appl. Phys. A* **2015**, *120*, 683.
[22] H. Iwata, D. Kawaguchi, H. Saka, *Microscopy* **2017**, *66*, 328.
[23] H. Kämmer, G. Matthäus, K. A. Lammers, C. Vetter, M. Chambonneau, S. Nolte, *Laser Photonics Rev.* **2019**, *13*, 1800268.
[24] M. Chambonneau, Q. Li, M. Chanal, N. Sanner, D. Grojo, *Opt. Lett.* **2016**, *41*, 4875.
[25] G. Matthäus, H. Kämmer, K. A. Lammers, C. Vetter, W. Watanabe, S. Nolte, *Opt. Express* **2018**, *26*, 24089.
[26] A. Turnali, M. Han, O. Tokel, *J. Opt. Soc. Am. B* **2019**, *36*, 966.
[27] M. Chambonneau, D. Richter, S. Nolte, D. Grojo, *Opt. Lett.* **2018**, *43*, 6069.
[28] M. Chambonneau, X. Wang, X. Yu, Q. Li, D. Chaudanson, S. Lei, D. Grojo, *Opt. Lett.* **2019**, *44*, 1619.
[29] F. Stutzki, C. Gaida, M. Gebhardt, F. Jansen, A. Wienke, U. Zeitner, F. Fuchs, C. Jauregui, D. Wandt, D. Kracht, J. Limpert, A. Tünnermann, *Opt. Lett.* **2014**, *39*, 4671.
[30] D. Gaponov, L. Lavoute, S. Février, A. Hideur, N. Ducros, Proc. SPIE, 9728, 972834.
[31] M. Chambonneau, L. Lavoute, D. Gaponov, V. Fedorov, A. Hideur, S. Février, S. Tzortzakis, O. Utéza, D. Grojo, *Phys. Rev. Appl.* **2019**, *12*, 024009.
[32] Q. Li, M. Chambonneau, M. Blothe, H. Gross, S. Nolte, *Appl. Opt.* **2021**, *60*, 3954.
[33] G. L. Tan, M. F. Lemon, D. J. Jones, R. H. French, *Phys. Rev. B: Condens. Matter Mater. Phys.* **2005**, *72*, 205117.
[34] J. C. Diels, W. Rudolph, *Ultrashort Laser Pulse Phenomena*, Academic Press, San Diego, CA **2006**, Ch. 7.
[35] A. R. Forouhi, I. Bloomer, *Phys. Rev. B* **1986**, *34*, 7018.
[36] C. D. Salzberg, J. J. Villa, *J. Opt. Soc. Am. A* **1957**, *47*, 244.
[37] J. Zhang, Q. Lin, G. Piredda, R. W. Boyd, G. P. Agrawal, P. M. Fauchet, *Appl. Phys. Lett.* **2007**, *91*, 071113.
[38] S. M. Eaton, H. Zhang, P. R. Herman, F. Yoshino, L. Shah, J. Bovatsek, A. Y. Arai, *Opt. Express* **2005**, *13*, 4708.
[39] G. G. Macfarlane, T. P. McLean, J. E. Quarrington, V. Roberts, *Phys. Rev.* **1958**, *111*, 1245.
[40] V. Alex, S. Finkbeiner, J. Weber, *J. Appl. Phys.* **1996**, *79*, 6943.
[41] W. Bludau, A. Onton, W. Heinke, *J. Appl. Phys.* **1974**, *45*, 1846.
[42] M. V. Fischetti, D. J. DiMaria, S. D. Brorson, T. N. Theis, J. R. Kirtley, *Phys. Rev. B* **1985**, *31*, 8124.
[43] E. Vella, F. Messina, M. Cannas, R. Boscaino, *Phys. Rev. B* **2011**, *83*, 174201.
[44] H. H. Li, *J. Phys. Chem. Ref. Data* **1980**, *9*, 561.
[45] I. H. Malitson, *J. Opt. Soc. Am. A* **1965**, *55*, 1205.
[46] M. Dinu, F. Quochi, H. Garcia, *Appl. Phys. Lett.* **2003**, *82*, 2954.
[47] A. D. Bristow, N. Rotenberg, H. M. van Driel, *Appl. Phys. Lett.* **2007**, *90*, 191104.
[48] Q. Lin, J. Zhang, G. Piredda, R. W. Boyd, P. M. Fauchet, G. P. Agrawal, *Appl. Phys. Lett.* **2007**, *91*, 10.
[49] A. Couairon, L. Sudrie, M. Franco, B. Prade, A. Mysyrowicz, *Phys. Rev. B* **2005**, *71*, 125435.
[50] H. R. Shanks, P. D. Maycock, P. H. Sidles, G. C. Danielson, *Phys. Rev.* **1963**, *130*, 1743.
[51] J. Bonse, T. Seuthe, M. Grehn, M. Eberstein, A. Rosenfeld, A. Mermillod-Blondin, *Appl. Phys. A* **2018**, *124*, 60.

[52] W. K. Rhim, S. K. Chung, A. J. Rulison, R. E. Spjut, *Int. J. Thermophys.* **1997**, *18*, 459.
[53] K. Yamaguchi, K. Itagaki, *J. Therm. Anal. Calorim.* **2002**, *69*, 1059.
[54] H. L. Schick, *Chem. Rev.* **1960**, *60*, 331.
[55] L. V. Keldysh, *Sov. Phys. J. Exp. Theor. Phys.* **1965**, *21*, 1136.
[56] D. Grojo, S. Leyder, P. Delaporte, W. Marine, M. Sentis, O. Utéza, *Phys. Rev. B* **2013**, *88*, 195135.
[57] S. Leyder, D. Grojo, P. Delaporte, W. Marine, M. Sentis, O. Utéza, *Appl. Surf. Sci.* **2013**, *278*, 13.
[58] V. V. Kononenko, E. V. Zavedeev, V. M. Gololobov, *Appl. Phys. A* **2016**, *122*, 293.
[59] A. Couairon, A. Mysyrowicz, *Phys. Rep.* **2007**, *441*, 47.
[60] E. I. Mareev, K. V. Lvov, B. V. Rumiantsev, E. A. Migal, I. D. Novikov, S. Y. Stremoukhov, F. V. Potemkin, *Laser Phys. Lett.* **2020**, *17*, 015402.
[61] E. I. Mareev, B. V. Rumiantsev, E. A. Migal, A. S. Bychkov, A. A. Karabutov, E. B. Cherepetskaya, V. A. Makarov, F. V. Potemkin, *Meas. Sci. Technol.* **2020**, *31*, 085204.
[62] A. Das, A. Wang, O. Uteza, D. Grojo, *Opt. Express* **2020**, *28*, 26623.
[63] B. Chimier, O. Utéza, N. Sanner, M. Sentis, T. Itina, P. Lassonde, F. Légaré, F. Vidal, J. C. Kieffer, *Phys. Rev. B* **2011**, *84*, 094104.
[64] D. J. Griffiths, *Introduction to Electrodynamics*, Fourth Edition, Pearson Education Inc., London **2013**, Ch. 8.
[65] B. C. Stuart, M. D. Feit, A. M. Rubenchik, B. W. Shore, M. D. Perry, *Phys. Rev. Lett.* **1995**, *74*, 2248.
[66] B. C. Stuart, M. D. Feit, S. Herman, A. M. Rubenchik, B. W. Shore, M. D. Perry, *Phys. Rev. B* **1996**, *53*, 1749.
[67] M. Mero, J. Liu, W. Rudolph, D. Ristau, K. Starke, *Phys. Rev. B* **2005**, *71*, 115109.
[68] X. Mao, S. S. Mao, R. E. Russo, *Appl. Phys. Lett.* **2003**, *82*, 697.
[69] Q. Sun, H. Jiang, Y. Liu, Z. Wu, H. Yang, Q. Gong, *Opt. Lett.* **2005**, *30*, 320.
[70] W. Gawelda, D. Puerto, J. Siegel, A. Ferrer, A. Ruiz de la Cruz, H. Fernandez, J. Solis, *Appl. Phys. Lett.* **2008**, *93*, 2008.
[71] P. Martin, S. Guizard, P. Daguzan, G. Petite, P. D'Oliveira, P. Meynadier, M. Perdrix, *Phys. Rev. B* **1997**, *55*, 5799.
[72] P. Audebert, P. Daguzan, A. Dos Santos, J. C. Gauthier, J. P. Geindre, S. Guizard, G. Hamoniaux, K. Krastev, P. Martin, G. Petite, A. Antonetti, *Phys. Rev. Lett.* **1994**, *73*, 1990.
[73] D. G. Papazoglou, S. Tzortzakis, *Appl. Phys. Lett.* **2008**, *93*, 2.
[74] D. Grojo, M. Gertsvolf, S. Lei, T. Barillot, D. M. Rayner, P. B. Corkum, *Phys. Rev. B* **2010**, *81*, 212301.
[75] K. Bergner, D. Flamm, M. Jenne, M. Kumkar, A. Tünnermann, S. Nolte, *Opt. Express* **2018**, *26*, 2873.
[76] M. Jenne, F. Zimmermann, D. Flamm, D. Großmann, J. Kleiner, M. Kumkar, S. Nolte, *J. Laser Micro/Nanoeng.* **2018**, *13*, 273.
[77] V. V. Kononenko, V. V. Konov, E. M. Dianov, *Opt. Lett.* **2012**, *37*, 3369.
[78] A. Mouskeftaras, M. Chanal, M. Chambonneau, R. Clady, O. Utéza, D. Grojo, *Appl. Phys. Lett.* **2016**, *108*, 041107.
[79] N. W. Ashcroft, N. D. Mermin, *Solid State Physics*, Harcourt College Publishers, New York **1976**, Ch. 1.
[80] S. Juodkazis, K. Nishimura, S. Tanaka, H. Misawa, E. G. Gamaly, B. Luther-Davies, L. Hallo, P. Nicolai, V. T. Tikhonchuk, *Phys. Rev. Lett.* **2006**, *96*, 166101.
[81] E. G. Gamaly, B. Luther-Davies, L. Hallo, P. Nicolai, V. T. Tikhonchuk, *Phys. Rev. B* **2006**, *73*, 214101.
[82] V. V. Kononenko, E. V. Zavedeev, M. I. Latushko, V. P. Pashinin, V. I. Konov, E. M. Dianov, *Quantum Electron.* **2012**, *42*, 925.
[83] F. Quéré, S. Guizard, P. Martin, G. Petite, O. Gobert, P. Meynadier, M. Perdrix, *Appl. Phys. B: Lasers Opt.* **1999**, *68*, 459.
[84] F. Quéré, S. Guizard, P. Martin, *Europhys. Lett.* **2001**, *56*, 138.
[85] S. Mao, F. Quéré, S. Guizard, X. Mao, R. Russo, G. Petite, P. Martin, *Appl. Phys. A* **2004**, *79*, 1695.
[86] D. Abdollahpour, D. G. Papazoglou, S. Tzortzakis, *Phys. Rev. A* **2011**, *84*, 053809.
[87] T. Balciunas, A. Melninkaitis, G. Tamosauskas, V. Sirutkaitis, *Opt. Lett.* **2008**, *33*, 58.
[88] D. Faccio, E. Rubino, A. Lotti, A. Couairon, A. Dubietis, G. Tamošauskas, D. G. Papazoglou, S. Tzortzakis, *Phys. Rev. A* **2012**, *85*, 033829.
[89] M. K. Bhuyan, F. Courvoisier, P. A. Lacourt, M. Jacquot, R. Salut, L. Furfaro, J. M. Dudley, *Appl. Phys. Lett.* **2010**, *97*, 4.
[90] S. Mitra, M. Chanal, R. Clady, A. Mouskeftaras, D. Grojo, *Appl. Opt.* **2015**, *54*, 7358.
[91] F. He, J. Yu, Y. Tan, W. Chu, C. Zhou, Y. Cheng, K. Sugioka, *Sci. Rep.* **2017**, *7*, 40785.
[92] D. Grojo, A. Mouskeftaras, P. Delaporte, S. Lei, *J. Appl. Phys.* **2015**, *117*, 153105.
[93] M. K. Bhuyan, P. K. Velpula, J. P. Colombier, T. Olivier, N. Faure, R. Stoian, *Appl. Phys. Lett.* **2014**, *104*, 021107.
[94] J. Amako, D. Sawaki, E. Fujii, *J. Opt. Soc. Am. B* **2003**, *20*, 2562.
[95] M. Duocastella, C. Arnold, *Laser Photonics Rev.* **2012**, *6*, 607.
[96] J. Bonse, S. Baudach, J. Krüger, W. Kautek, M. Lenzner, *Appl. Phys. A* **2002**, *74*, 19.
[97] D. Austin, K. Kafka, C. I. Blaga, L. F. Dimauro, E. Chowdhury, Proc. SPIE (**2014**) 9237, 92370V.
[98] T. Wang, N. Venkatram, J. Gosciniak, Y. Cui, G. Qian, W. Ji, D. T. H. Tan, *Opt. Express* **2013**, *21*, 32192.
[99] D. G. Papazoglou, N. K. Efremidis, D. N. Christodoulides, S. Tzortzakis, *Opt. Lett.* **2011**, *36*, 1842.
[100] P. Panagiotopoulos, A. Couairon, M. Kolesik, D. G. Papazoglou, J. V. Moloney, S. Tzortzakis **2016**, *93*, 033808.
[101] I. B. Bogatyrev, D. Grojo, P. Delaporte, S. Leyder, M. Sentis, W. Marine, T. E. Itina, *J. Appl. Phys.* **2011**, *110*, 103106.
[102] E. V. Zavedeev, V. V. Kononenko, V. I. Konov, *Laser Phys.* **2016**, *26*, 016101.
[103] S. Pearl, N. Rotenberg, H. M. van Driel, *Appl. Phys. Lett.* **2008**, *93*, 131102.
[104] F. Gholami, S. Zlatanovic, A. Simic, L. Liu, D. Borlaug, N. Alic, M. P. Nezhad, Y. Fainman, S. Radic, *Appl. Phys. Lett.* **2011**, *99*, 081102.
[105] X. Gai, Y. Yu, B. Kuyken, P. Ma, S. J. Madden, J. Van Campenhout, P. Verheyen, G. Roelkens, R. Baets, B. Luther-Davies, *Laser Photonics Rev.* **2013**, *7*, 1054.
[106] L. Rapp, B. Haberl, C. Pickard, J. Bradby, E. Gamaly, J. Williams, A. Rode, *Nat. Commun.* **2015**, *6*, 7555.
[107] L. A. Smillie, M. Niihori, L. Rapp, B. Haberl, J. S. Williams, J. E. Bradby, C. J. Pickard, A. V. Rode, *Phys. Rev. Mater.* **2020**, *4*, 093803.
[108] V. V. P. Sreenivas, M. Bülters, R. B. Bergmann, *J. Eur. Opt. Soc.: Rapid Publ.* **2012**, *7*, 12035.
[109] K. A. Serrels, E. Ramsay, R. J. Warburton, D. T. Reid, *Nat. Photonics* **2008**, *2*, 311.
[110] K. Agarwal, R. Chen, L. S. Koh, C. J. Sheppard, X. Chen, *Phys. Rev. X* **2015**, *5*, 021014.
[111] D. H. Habing, *IEEE Trans. Nucl. Sci.* **1965**, *12*, 91.
[112] S. C. Moss, S. D. LaLumondiere, J. R. Scarpulla, K. P. MacWilliams, W. R. Crain, R. Koga, *IEEE Trans. Nucl. Sci.* **1995**, *42*, 1948.
[113] J. S. Melinger, D. McMorrow, A. B. Campbell, S. Buchner, L. H. Tran, A. R. Knudson, W. R. Curtice, *J. Appl. Phys.* **1998**, *84*, 690.
[114] D. McMorrow, J. Melinger, S. Buchner, T. Scott, R. Brown, N. Haddad, *IEEE Trans. Nucl. Sci.* **2000**, *47*, 559.
[115] S. Skorobogatov, Local heating attacks on flash memory devices, in 2009 IEEE International Workshop on Hardware-Oriented Security and Trust, HOST 2009, IEEE, Piscataway, NJ **2009**, pp. 1–6.
[116] R. Llido, P. Masson, A. Regnier, V. Goubier, G. Haller, V. Pouget, D. Lewis, *Microelectron. Reliab.* **2012**, *52*, 1816.

[117] A. Sarafianos, R. Llido, J. M. Dutertre, O. Gagliano, V. Serradeil, M. Lisart, V. Goubier, A. Tria, *Microelectron. Reliab.* **2012**, *52*, 2035.
[118] A. Sarafianos, C. Roscian, J. Dutertre, M. Lisart, A. Tria, *Microelectron. Reliab.* **2013**, *53*, 1300.
[119] D. McMorrow, W. T. Lotshaw, J. S. Melinger, S. Buchner, R. L. Pease, *IEEE Trans. Nucl. Sci.* **2002**, *49 I*, 3002.
[120] D. McMorrow, W. Lotshaw, J. Melinger, S. Buchner, R. Pease, *IEEE Trans. Nucl. Sci.* **2002**, *49*, 3002.
[121] J. A. Pellish, R. A. Reed, D. McMorrow, J. S. Melinger, P. Jenkins, A. K. Sutton, R. M. Diestelhorst, S. D. Phillips, J. D. Cressler, V. Pouget, N. D. Pate, J. A. Kozub, M. H. Mendenhall, R. A. Weller, R. D. Schrimpf, P. W. Marshall, A. D. Tipton, G. Niu, *IEEE Trans. Nucl. Sci.* **2008**, *55*, 2936.
[122] F. El-Mamouni, E. X. Zhang, N. D. Pate, N. Hooten, R. D. Schrimpf, R. A. Reed, K. F. Galloway, D. McMorrow, J. Warner, E. Simoen, C. Claeys, A. Griffoni, D. Linten, G. Vizkelethy, *IEEE Trans. Nucl. Sci.* **2011**, *58*, 2563.
[123] A. Khachatrian, N. J. Roche, D. McMorrow, J. H. Warner, S. P. Buchner, J. S. Melinger, *IEEE Trans. Nucl. Sci.* **2014**, *61*, 3416.
[124] J. M. Hales, A. Khachatrian, N. J. Roche, J. Warner, S. P. Buchner, D. McMorrow, *IEEE Trans. Nucl. Sci.* **2015**, *62*, 1550.
[125] V. Della Marca, M. Chambonneau, S. Souiki-Figuigui, J. Postel-Pellerin, P. Canet, P. Chiquet, E. Kussener, F. Yengui, R. Wacquez, D. Grojo, J. M. Portal, M. Lisart, in 2016 IEEE International Reliability Physics Symposium (IRPS), IEEE, Piscataway, NJ **2016**, pp. 7B–4–1–7B–4–7.
[126] M. Chambonneau, S. Souiki-Figuigui, P. Chiquet, V. Della Marca, J. Postel-Pellerin, P. Canet, J. M. Portal, D. Grojo, *Appl. Phys. Lett.* **2017**, *110*, 6.
[127] J. M. Hales, N. J. Roche, A. Khachatrian, D. Mcmorrow, S. Buchner, J. Warner, M. Turowski, K. Lilja, N. C. Hooten, E. X. Zhang, R. A. Reed, R. D. Schrimpf, *IEEE Trans. Nucl. Sci.* **2017**, *64*, 1133.
[128] J. M. Hales, S. H. Chi, T. Allen, S. Benis, N. Munera, J. W. Perry, D. McMorrow, D. J. Hagan, E. W. Van Stryland, in Conference on Lasers and Electro-Optics, OSA Publishing, Washington, D.C. (**2018**), p. JTu2A.59.
[129] J. M. Hales, A. Khachatrian, S. Buchner, N. J. Roche, J. Warner, Z. E. Fleetwood, A. Ildefonso, J. D. Cressler, V. Ferlet-Cavrois, D. Mcmorrow, *IEEE Trans. Nucl. Sci.* **2018**, *65*, 1724.
[130] A. Ildefonso, Z. E. Fleetwood, G. N. Tzintzarov, J. M. Hales, D. Nergui, M. Frounchi, A. Khachatrian, S. P. Buchner, D. Mcmorrow, J. H. Warner, J. Harms, A. Erickson, K. Voss, V. Ferlet-Cavrois, J. D. Cressler, *IEEE Trans. Nucl. Sci.* **2019**, *66*, 359.
[131] P. Chiquet, M. Chambonneau, V. Della Marca, J. Postel-Pellerin, P. Canet, S. Souiki-Figuigui, G. Idda, J. M. Portal, D. Grojo, *Sci. Rep.* **2019**, *9*, 7392.
[132] J. M. Hales, A. Khachatrian, J. Warner, S. Buchner, A. Ildefonso, G. N. Tzintzarov, D. Nergui, D. M. Monahan, S. D. LaLumondiere, J. D. Cressler, D. McMorrow, *Opt. Express* **2019**, *27*, 37652.
[133] J. M. Hales, J. D. Cressler, D. McMorrow, A. Khachatrian, S. Buchner, J. Warner, A. Ildefonso, G. N. Tzintzarov, D. Nergui, D. M. Monahan, S. D. LaLumondiere, *IEEE Trans. Nucl. Sci.* **2020**, *67*, 81.
[134] L. D. Ryder, K. L. Ryder, A. L. Sternberg, J. A. Kozub, H. Gong, E. X. Zhang, D. Linten, J. Mitard, R. A. Weller, R. D. Schrimpf, S. M. Weiss, R. A. Reed, *IEEE Trans. Nucl. Sci.* **2020**, *67*, 38.
[135] D. Faccio, M. Clerici, A. Averchi, O. Jedrkiewicz, S. Tzortzakis, D. Papazoglou, F. Bragheri, L. Tartara, A. Trita, S. Henin, I. Cristiani, A. Couairon, P. Di Trapani, *Opt. Express* **2008**, *16*, 8213.
[136] H. Pinhas, O. Wagner, Y. Danan, M. Danino, Z. Zalevsky, M. Sinvani, *Opt. Express* **2018**, *26*, 25370.
[137] S. W. Hell, J. Wichmann, *Opt. Lett.* **1994**, *19*, 780.
[138] V. Kadan, S. Pavlova, I. Pavlov, H. Rezaei, Ö. Ilday, I. Blonskyi, *Appl. Phys. A: Mater. Sci. Process.* **2018**, *124*, 560.
[139] D. von der Linde, H. Schulz, T. Engers, H. Schuler, *IEEE J. Quantum Electron.* **1992**, *28*, 2388.
[140] N. H. Burnett, H. A. Baldis, M. C. Richardson, G. D. Enright, *Appl. Phys. Lett.* **1977**, *31*, 172.
[141] P. B. Corkum, F. Krausz, *Nat. Phys.* **2007**, *3*, 381.
[142] M. A. Green, M. J. Keevers, *Prog. Photovoltaics Res. Appl.* **1995**, *3*, 189.
[143] A. Marcinkevičiūtė, V. Jukna, R. Šuminas, N. Garejev, G. Tamošauskas, A. Dubietis, *Opt. Lett.* **2019**, *44*, 1343.
[144] M. Kumagai, N. Uchiyama, E. Ohmura, R. Sugiura, K. Atsumi, K. Fukumitsu, in 2006 IEEE International Symposium on Semiconductor Manufacturing, IEEE, Piscataway, NJ **2006**, pp. 215–218.
[145] E. Ohmura, F. Fukuyo, K. Fukumitsu, H. Morita, *Int. J. Comput. Mater. Sci. Surf. Eng.* **2007**, *1*, 677.
[146] O. Haupt, F. Siegel, A. Schoonderbeek, L. Richter, R. Kling, A. Ostendorf, *J. Laser Micro/Nanoeng.* **2008**, *3*, 135.
[147] E. Ohmura, Temperature Rise of Silicon Due to Absorption of Permeable Pulse Laser, in Heat Transfer - Engineering Applications (Ed. V. Vikhrenko), InTech, Rijeka (**2011**), pp. 29–46.
[148] F. Fukuyo, K. Fukumitsu, N. Uchiyama, T. Wakuda, US8097829B2 (**2006**).
[149] N. Liu, J. Vincent, K. Moumanis, J. J. Dubowski, *J. Laser Micro/Nanoeng.* **2016**, *11*, 232.
[150] P. Verburg, Ph.D. Thesis, University of Twente, Netherlands **2015**.
[151] X. Yu, X. Wang, M. Chanal, C. A. Trallero-Herrero, D. Grojo, S. Lei, *Appl. Phys. A: Mater. Sci. Process.* **2016**, *122*, 1001.
[152] W. Spitzer, H. Y. Fan, *Phys. Rev.* **1957**, *108*, 268.
[153] K. Shimamura, J. Okuma, S. Ohmura, F. Shimojo, *J. Phys. Conf. Ser.* **2012**, *402*, 012044.
[154] H. Iwata, D. Kawaguchi, H. Saka, *Microscopy* **2018**, *67*, 30.
[155] H. Saka, H. Iwata, D. Kawaguchi, *Microscopy* **2018**, *67*, 112.
[156] D. Kawaguchi, H. Iwata, H. Saka, *Philos. Mag.* **2019**, *99*, 1849.
[157] S. K. Sundaram, E. Mazur, *Nat. Mater.* **2002**, *1*, 217.
[158] Q. Li, M. Chambonneau, M. Chanal, D. Grojo, *Appl. Opt.* **2016**, *55*, 9577.
[159] H. Bénard, *J. Phys. Theor. Appl.* **1900**, *9*, 513.
[160] M. Cross, H. Greenside, *Pattern Formation and Dynamics in Nonequilibrium Systems*, Cambridge University Press, Cambridge **2009**.
[161] M. Birnbaum, *J. Appl. Phys.* **1965**, *36*, 3688.
[162] B. Öktem, I. Pavlov, S. Ilday, H. Kalaycıoğlu, A. Rybak, S. Yavaş, M. Erdoğan, F. Ö. Ilday, *Nat. Photonics* **2013**, *7*, 897.
[163] C. Kerse, H. Kalaycloğ Lu, P. Elahi, B. Çetin, D. K. Kesim, Ö. Akçaalan, S. Yavaş, M. D. Aşlk, B. Öktem, H. Hoogland, R. Holzwarth, F. Ö. Ilday, *Nature* **2016**, *537*, 84.
[164] S. Ilday, G. Makey, G. B. Akguc, Ö. Yavuz, O. Tokel, I. Pavlov, O. Gülseren, F. Ö. Ilday, *Nat. Commun.* **2017**, *8*, 14942.
[165] G. Makey, S. Galioglu, R. Ghaffari, E. D. Engin, G. Yıldırım, Ö. Yavuz, O. Bektaş, Ü. S. Nizam, Ö. Akbulut, Ö. Şahin, K. Güngör, D. Dede, H. V. Demir, F. Ö. Ilday, S. Ilday, *Nat. Phys.* **2020**, *16*, 795.
[166] A. Rousse, C. Rischel, S. Fourmaux, I. Uschmann, S. Sebban, G. Grillon, P. Balcou, E. Förster, J. Geindre, P. Audebert, J. Gauthier, D. Hulin, *Nature* **2001**, *410*, 65.
[167] K. Sokolowski-Tinten, C. Blome, J. Blums, A. Cavalleri, C. Dietrich, A. Tarasevitch, I. Uschmann, E. Förster, M. Kammler, M. Horn von Hoegen, D. von der Linde, *Nature* **2003**, *422*, 287.
[168] R. R. Gattass, E. Mazur, *Nat. Photonics* **2008**, *2*, 219.
[169] H. A. Weakliem, D. Redfield, *J. Appl. Phys.* **1979**, *50*, 1491.
[170] C. W. Carr, J. D. Bude, P. DeMange, *Phys. Rev. B* **2010**, *82*, 184304.
[171] P. C. Verburg, G. R. B. E. Römer, A. J. Huis in 't Veld, *Appl. Phys. A* **2014**, *114*, 1135.
[172] H. Kiyota, K. Hara, M. Jankowski, M. M. Fejer, *J. Appl. Phys.* **2020**, *127*, 085106.
[173] D. Grojo, M. Chambonneau, US10509168 (**2019**).

[174] According to ref. [35], the refractive index value of amorphous silicon is extremely dependent on the molecular structure and composition as well as the preparation method.
[175] M. J. A. de Dood, A. Polman, T. Zijlstra, E. W. J. M. van der Drift, *J. Appl. Phys.* **2002**, *92*, 649.
[176] P. A. Temple, C. E. Hathaway, *Phys. Rev. B* **1973**, *7*, 3685.
[177] J. Bonse, K. W. Brzezinka, A. J. Meixner, *Appl. Surf. Sci.* **2004**, *221*, 215.
[178] R. Osellame, S. Taccheo, M. Marangoni, R. Ramponi, P. Laporta, D. Polli, S. De Silvestri, G. Cerullo, *J. Opt. Soc. Am. B* **2003**, *20*, 1559.
[179] M. Ams, G. D. Marshall, D. J. Spence, M. J. Withford, *Opt. Express* **2005**, *13*, 5676.
[180] X. Wang, X. Yu, H. Shi, X. Tian, M. Chambonneau, D. Grojo, B. DePaola, M. Berg, S. Lei, *J. Laser Appl.* **2019**, *31*, 022601.
[181] X. Wang, X. Yu, M. Berg, B. DePaola, H. Shi, P. Chen, L. Xue, X. Chang, S. Lei, *J. Laser Appl.* **2020**, *32*, 022002.
[182] X. Wang, X. Yu, M. J. Berg, P. Chen, B. Lacroix, S. Fathpour, S. Lei, *Opt. Express* **2021**, *29*, 14201.
[183] M. G. Moharam, T. K. Gaylord, *J. Opt. Soc. Am. A* **1983**, *73*, 1105.
[184] L. Sudrie, M. Franco, B. Prade, A. Mysyrowicz, *Opt. Commun.* **1999**, *171*, 279.
[185] K. Sugimoto, S. Matsuo, Y. Naoi, *Sci. Rep.* **2020**, *10*, 21451.
[186] J. Hu, C. R. Menyuk, *Adv. Opt. Photonics* **2009**, *1*, 58.
[187] Y. Bellouard, A. Champion, M. Gevincevicius, C. Corbari, M. Beresna, P. Kazansky, O. Chappuis, M. Kral, R. Clavel, J. M. Breguet, F. Barrot, Y. Mabillard, S. Bottinelli, M. Hopper, C. Hoenninger, E. Mottay, J. Lopez, in Conference on Lasers and Electro-Optics 2012, OSA, Washington, D.C., **2012**, p. ATu3L.3.
[188] M. Beresna, M. Gecevičius, P. G. Kazansky, T. Taylor, A. V. Kavokin, *Appl. Phys. Lett.* **2012**, *101*, 053120.
[189] T. Gissibl, S. Thiele, A. Herkommer, H. Giessen, *Nat. Photonics* **2016**, *10*, 554.
[190] F. Kotz, K. Arnold, W. Bauer, D. Schild, N. Keller, K. Sachsenheimer, T. M. Nargang, C. Richter, D. Helmer, B. E. Rapp, *Nature* **2017**, *544*, 337.
[191] R. Bekenstein, Y. Kabessa, Y. Sharabi, O. Tal, N. Engheta, G. Eisenstein, A. J. Agranat, M. Segev, *Nat. Photonics* **2017**, *11*, 664.
[192] C. R. Ocier, C. A. Richards, D. A. Bacon-Brown, Q. Ding, R. Kumar, T. J. Garcia, J. van de Groep, J. H. Song, A. J. Cyphersmith, A. Rhode, A. N. Perry, A. J. Littlefield, J. Zhu, D. Xie, H. Gao, J. F. Messinger, M. L. Brongersma, K. C. Toussaint, L. L. Goddard, P. V. Braun, *Light Sci. Appl.* **2020**, *9*, 196.
[193] B. Dang, M. S. Bakir, D. C. Sekar, C. R. King Jr, J. D. Meindl, *IEEE Trans. Adv. Packag.* **2010**, *33*, 79.
[194] J. Zhang, A. Čerkauskaitė, R. Drevinskas, A. Patel, M. Beresna, P. G. Kazansky, Proc. SPIE (**2016**), 9736, 97360U.
[195] G. Shakhgildyan, A. Lipatiev, S. Lotarev, S. Fedotov, V. Sigaev, *Front. Chem.* **2020**, *8*, 384.
[196] J. Sun, E. Timurdogan, A. Yaacobi, E. S. Hosseini, M. R. Watts, *Nature* **2013**, *493*, 195.
[197] S. Larouche, Y. J. Tsai, T. Tyler, N. M. Jokerst, D. R. Smith, *Nat. Mater.* **2012**, *11*, 450.
[198] G. Zheng, H. Mühlenbernd, M. Kenney, G. Li, T. Zentgraf, S. Zhang, *Nat. Nanotechnol.* **2015**, *10*, 308.
[199] H. Kämmer, G. Matthäus, S. Nolte, M. Chanal, O. Utéza, D. Grojo, *Appl. Phys. A* **2018**, *124*, 302.
[200] M. Lenzner, J. Krüger, S. Sartania, Z. Cheng, C. Spielmann, G. Mourou, W. Kautek, F. Krausz, *Phys. Rev. Lett.* **1998**, *80*, 4076.
[201] N. Tolstik, R. Richter, M. Skogen, I. Astrauskas, E. Sorokin, I. T. Sorokina, Ultra-short pulsed fiber-based lasers around 2.1 um and their applications, Proc. SPIE (**2020**), 11357, 1135713.
[202] R. A. Richter, N. Tolstik, S. Rigaud, P. D. Valle, A. Erbe, P. Ebbinghaus, I. Astrauskas, V. Kalashnikov, E. Sorokin, I. T. Sorokina, *J. Opt. Soc. Am. B* **2020**, *37*, 2543.
[203] Y. Shimotsuma, T. Sei, M. Mori, M. Sakakura, K. Miura, *Appl. Phys. A: Mater. Sci. Process.* **2016**, *122*, 159.
[204] A. Wang, A. Das, D. Grojo, *Research* **2020**, *2020*, 8149764.
[205] K. Sugioka, M. Iida, H. Takai, K. Micorikawa, *Opt. Lett.* **2011**, *36*, 2734.
[206] J. Peng, D. Grojo, D. M. Rayner, P. B. Corkum, *Appl. Phys. Lett.* **2013**, *102*, 161105.
[207] Y. Shimotsuma, P. G. Kazansky, J. Qiu, K. Hirao, *Phys. Rev. Lett.* **2003**, *91*, 247405.
[208] V. Bhardwaj, E. Simova, P. Rajeev, C. Hnatovsky, R. Taylor, D. Rayner, P. Corkum, *Phys. Rev. Lett.* **2006**, *96*, 057404.
[209] A. Wang, A. Das, D. Grojo, *Phys. Rev. Res.* **2020**, *2*, 033023.
[210] N. L. Boling, M. D. Crisp, G. Dubé, *Appl. Opt.* **1973**, *12*, 650.
[211] S. Papernov, A. W. Schmid, *J. Appl. Phys.* **2008**, *104*, 063101.
[212] S. Lei, D. Grojo, J. Ma, X. Yu, H. Wu, *Proc. Manuf.* **2016**, *5*, 594.
[213] I. Astrauskas, B. Považay, A. Baltuška, A. Pugžlys, *Opt. Laser Technol.* **2021**, *133*, 106535.
[214] M. Chambonneau, Q. Li, V. Y. Fedorov, M. Blothe, K. Schaarschmidt, M. Lorenz, S. Tzortzakis, S. Nolte, *Laser Photonics Rev.* **2021**, *15*, 2000433.
[215] M. Chambonneau, Q. Li, V. Y. Fedorov, M. Blothe, S. Tzortzakis, S. Nolte, Proc. SPIE (**2021**), 11676, 1167610.
[216] J. Marburger, *Prog. Quantum Electron.* **1975**, *4*, 35.
[217] Y. Ito, H. Sakashita, R. Suzuki, M. Uewada, K. P. Luong, R. Tanabe, *J. Laser Micro/Nanoeng.* **2014**, *9*, 98.
[218] K. P. Luong, R. Tanabe-Yamagishi, N. Yamada, Y. Ito, *J. Laser Appl.* **2020**, *32*, 012017.
[219] N. Bloembergen, *Appl. Opt.* **1973**, *12*, 661.
[220] N. Gehlich, T. Bonhoff, L. Sisken, M. Ramme, C. Gaida, M. Gebhardt, I. Mingareev, L. Shah, M. C. Richardson, Proc. SPIE (**2014**), 8968, 89680W.
[221] I. Mingareev, N. Gehlich, T. Bonhoff, A. Abdulfattah, A. M. Sincore, P. Kadwani, L. Shah, M. Richardson, *Int. J. Adv. Manuf. Technol.* **2016**, *84*, 2567.
[222] B. Ma, K. Wang, J. Han, Z. Zhang, X. Cheng, *Laser Phys.* **2020**, *30*, 036003.
[223] S. G. Demos, R. N. Raman, R. a. Negres, *Opt. Express* **2013**, *21*, 4875.
[224] M. Chambonneau, L. Lamaignère, *Sci. Rep.* **2018**, *8*, 891.
[225] A. Alberucci, N. Alasgarzade, M. Chambonneau, M. Blothe, H. Kämmer, G. Matthäus, C. P. Jisha, S. Nolte, *Phys. Rev. Appl.* **2020**, *14*, 024078.
[226] J. R. Macdonald, S. J. Beecher, P. A. Berry, K. L. Schepler, A. K. Kar, *Appl. Phys. Lett.* **2013**, *102*, 161110.
[227] J. R. Macdonald, S. J. Beecher, A. Lancaster, P. A. Berry, K. L. Schepler, S. B. Mirov, A. K. Kar, *Opt. Express* **2014**, *22*, 7052.
[228] D. J. Wilson, K. Schneider, S. Hönl, M. Anderson, Y. Baumgartner, L. Czornomaz, T. J. Kippenberg, P. Seidler, *Nat. Photonics* **2020**, *14*, 57.

**Maxime Chambonneau** received his Ph.D. degree at Aix-Marseille University (France) in 2014, under the supervision of Laurent Lamaignère, Guillaume Duchateau, and Jean-Yves Natoli. He worked as a post-doctoral researcher at LP3 laboratory in Marseille (France) from 2015 to 2018, under the supervision of David Grojo. From 2018, he is a post-doctoral researcher at the Institute of Applied Physics in Jena (Germany), under the supervision of Stefan Nolte.

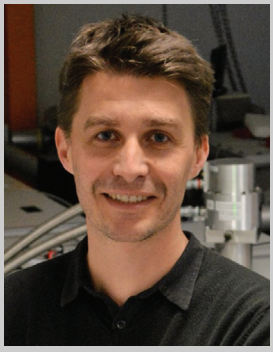

**David Grojo** received his Ph.D. degree at Aix-Marseille University in 2006, France. After 3 years working in the Attosecond Science program of Canada, he is researcher at the French National Center for Scientific Research (CNRS), France. His researches are conducted at LP3 laboratory, Marseille, France. Among other things, he studies nonlinear processes with non-conventional radiations. This opens new and exciting opportunities to tailor materials with nanometer resolutions and a new range of 3D laser direct writing applications.

**Onur Tokel** received his Ph.D. degree at Cornell University, USA in 2011, followed by postdoctoral studies at Harvard University, USA and Bilkent University, Turkey. He is currently leading the Photonic Devices Laboratory at the Department of Physics and also at the National Nanotechnology Research Center, Turkey. His research is focused on investigating laser-material interactions, developing novel laser micro-/nano-fabrication approaches and 3D laser-writing methods.

**Fatih Ömer Ilday** is a professor of physics, electrical engineering, and materials science and nanotechnology at Bilkent University in Ankara, Turkey, where he founded the Ultrafast Optics and Lasers Laboratory (UFOLAB). He received his Ph.D. degree at Cornell University, USA, in 2004, followed by a post-doctoral fellow and later research scientist positions at Massachusetts Institute of Technology, USA, before joining the faculty at Bilkent University. His research is focused on mode-locking of lasers, complex laser-material interactions, and nonlinear dynamics and statistical physics of self-organization.

**Stelios Tzortzakis** received his Ph.D. from the École Polytechnique (France, 2001) in Nonlinear Optics. He is a professor of physics at Texas A&M University at Qatar and the Materials Science and Technology Department of the University of Crete, Greece. He is heading the Ultrashort Nonlinear Interactions and Sources (UNIS) research group at the Institute of Electronic Structure and Laser (IESL) at FORTH, Greece, where he also served as Deputy Director for many years. He is an expert in nonlinear laser propagation phenomena in transparent media and introduced the filamentation.org scientific resource.

**Stefan Nolte** is professor of laser physics at the Friedrich-Schiller-University in Jena, Germany, where he is heading the Ultrafast Optics group at the Institute of Applied Physics. He is also the Deputy Director of the Fraunhofer IOF, Jena. He studied physics at the University of Hannover, Germany, from where he received his diploma in 1995 and his Ph.D. in 1999. He has been actively engaged in research on femtosecond laser micromachining and materials modification since the field's inception in the mid-1990s.